Microdosimetric studies of Auger electrons from DNA-incorporated ^{123}I using the micronucleus assay and the Geant4 Monte Carlo simulation toolkit

by Hein Fourie

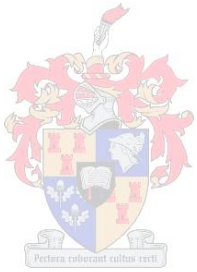

Thesis presented in partial fulfilment of the requirements for the degree of Master of Science at Stellenbosch University

Supervisor: Prof. Richard T Newman

Co-supervisor: Prof. Jacobus P Slabbert

December 2014

Declaration

By submitting this thesis electronically, I declare that the entirety of the work contained therein is my own original work, that I am the sole author thereof (save to the extent explicitly otherwise stated), that reproduction and publication thereof by Stellenbosch University will not infringe any third party rights and that I have not previously in its entirety or in part submitted it for obtaining any qualification.

Abstract

This study's focus is on the determination and quantization of radiation damage on a cellular level due to the decay of the Auger electron-emitting ^{123}I and the replication of this energy deposition using Geant4 Monte Carlo simulations. The relatively short half-life of ^{123}I (13.2 hours) makes it ideal for studies of Auger electrons which induce biological damage similar to that of high linear energy transfer radiations, when permitted to deposit their energy in close proximity to DNA. Due to small cellular dimensions, direct dose measurements are impossible but estimates may be made from Monte Carlo simulations. In this investigation the thymidine analogue 5-[^{123}I]-iodo-2-deoxyuridine (^{123}IUdR) was used to incorporate the ^{123}I into the cellular DNA of T-lymphocytes from two human donors. Radiation induced micronuclei were numerated in binucleated cells using fluorescence microscopy. The energy deposition per decay of ^{123}I was calculated within a spherical geometry, having the same size and density as a human lymphocyte, using the open source Geant4 toolkit. The absorbed energy per disintegration was used to convert the incorporated ^{123}I activity (Bq) into absorbed dose (Gy) values, in order to compare the biological damage caused by the radioactive iodine to ^{60}Co γ-radiation. A linear relationship between micronuclei frequency and ^{123}I activity could be established. The linear dose-response noted for Auger electrons in the study is indicative of the high-LET nature of these particles. Using the linear-quadratic dose-response curve for micronuclei frequencies following exposure to graded doses of ^{60}Co γ-rays, the relative biological effectiveness (RBE) of the DNA incorporated ^{123}I estimated in this work was found to range from 19 ± 10 to 32 ± 7 for lymphocyte donor 1 and 15 ± 6 to 42 ± 11 for donor 2. The dose limiting RBE (RBE_M) for lymphocyte donor 1 and 2 are respectively 34 ± 8 and 50 ± 15 and follows the expected shift in terms of the inherent radiosensitivity of the donors. We also considered the inclusion of the S-phase fraction of the lymphocytes in the dosimetry calculations. The resultant RBEs of the dose points of lymphocyte donor 1 ranges from 4 ± 2 to 7 ± 2, and those of donor 2 ranges from 3 ± 1 to 9 ± 2. The RBE_M for lymphocyte donor 1 and 2 are respectively 7 ± 2 and 11 ± 3. The inclusion of the S-phase fraction reduces the calculated RBEs significantly and these observed RBE values relate well to those obtained in studies with fibroblasts and ^{125}IUdR.

Opsomming

Hierdie studie fokus op die bepaling en kwantisering van stralingskade op 'n sellulêre vlak as gevolg van die verval van ^{123}I wat Auger elektrone afgee, asook die simulering van hierdie energie afsetting met behulp van die Geant4 Monte Carlo program. Die relatiewe kort half-leeftyd van ^{123}I (13.2 uur) maak dit ideaal vir studies van Auger elektrone wat biologiese skade soortgelyk aan dié van 'n hoë lineêre-energie-oordrag uitstraling veroorsaak, indien die energie van die elektrone naby sellulêre DNA geabsorbeer word. As gevolg van die klein sellulêre dimensies is direkte dosis metings egter onmoontlik, maar skattings kan gemaak word met behulp van Monte Carlo simulasies. Die timidien analoog 5-[^{123}I]-jodo-2-deoxyuridien (^{123}IUdR) was in hierdie ondersoek gebruik om die ^{123}I in die DNA van menslike T-limfosiete in te bou. Mikrokerne in dubbel-kernige selle wat vorm as gevolg van die Auger elektrone was getel met behulp van fluoressensie mikroskopie. Die energie afsetting per ^{123}I verval was bereken binne ‘n sferiese geometrie, met dieselfde grootte en digtheid as 'n menslike limfosiet, met behulp van die Geant4 sagteware. Die geabsorbeerde energie per verval was gebruik om die geïnkorporeerde ^{123}I aktiwiteit (Bq) om te skakel na ‘n waarde van geabsorbeerde dosis (Gy), ten einde die biologiese skade wat veroorsaak word deur die radioaktiewe jodium-123 met kobalt-60 gamma straling te vergelyk. ‘n Lineêre verwantskap tussen die mikrokerne frekwensies en die ^{123}I aktiwiteit is vasgestel. Hierdie verwantskap vir Auger elektrone is 'n aanduiding van die hoë lineêre-energie-oordrag van hierdie deeltjies. Die lineêr-kwadratiese dosis-effek krommes vir mikrokerne frekwensies na blootstelling aan ^{60}Co γ-strale was gebruik om die relatiewe biologiese doeltreffendheid (RBE) van die DNA geïnkorporeerde ^{123}I te beraam. RBE waardes wissel van 19 ± 10 tot 32 ± 7 vir limfosiete van skenker 1 en 15 ± 6 tot 42 ± 11 vir skenker 2. Die dosis beperkte RBE (RBE_M) vir limfosiet skenker 1 en 2 is onderskeidelik 34 ± 8 en 50 ± 15 en volg die verwagte skuif in terme van die inherente radiogevoeligheid van die skenkers. Die fraksie van limfosiete wat in S-fase was tydens die blootstelling aan ^{125}IUdR was ingesluit in verdere dosimetrie berekeninge. Die gevolglike RBEs van die dosispunte van limfosiete van skenker 1 wissel van 4 ± 2 tot 7 ± 2 en dié van skenker 2 wissel van 3 ± 1 tot 9 ± 2. Die RBE_M vir limfosiet skenker 1 en 2 is onderskeidelik 7 ± 2 en 11 ± 3. Die insluiting van die S-fase fraksie verminder die berekende RBEs aansienlik en die RBE waardes waargeneem hou goed verband met die wat in studies met fibroblaste en ^{125}IUdR verkry is.

Acknowledgements

I wish to thank my supervisors, Prof. Richard T Newman and Prof. Jacobus P Slabbert, for their academic and administrative support and knowledge in the fields of radiation physics and radiobiology.

Similarly, I wish to thank Mr. Philip Beukes for his continuous supervision and instruction in and outside of the laboratory, as well as his guidance in the field of radiation protection.

I also wish to thank Dr. Neil Rossouw for the synthesis and labeling of the 5-[^{123}I]-iodo-2-deoxyuridine.

A final thank you to Prof. J P Slabbert and Mr. P Beukes of iThemba LABS, for allowing me to undertake the research experiments with biological samples and radioactive substances under their supervision and REC ethical clearance (reference number: S12/04/091) obtained from Stellenbosch University.

Parts of this work have been presented at the 2013 SAIP conference (entitled "*Cytogenetic analysis of ^{60}Co γ-radiation-induced chromosome damage and simulations using the Geant4 Monte Carlo toolkit*"), the 2014 SAIP conference (entitled "*Auger electron studies using Monte Carlo simulations of ^{123}I incorporated into human lymphocytes*") and the 2014 SAAPMB conference (entitled "*Estimating the Relative Biological Effectiveness (RBE) of Auger electrons in human lymphocytes using micronuclei inductions by 5-[^{123}I]-iodo-2-deoxyuridine and Monte Carlo simulations*").

Gratitude is expressed towards the Faculty of Science and the Department of Physics of Stellenbosch University for their continued financial assistance during the course of this postgraduate degree.

The financial assistance of the National Research Foundation (NRF) towards this research is hereby acknowledged. Opinions expressed and conclusions arrived at, are those of the author and are not necessarily to be attributed to the NRF.

Table of Contents

List of Figures

List of Tables

Chapter 1: Introduction

1.1. Microdosimetry & Problem statement

Nuclear medicine and molecular imaging use unsealed radionuclides for diagnostic and therapeutic purposes. In targeted radiotherapy, the aim is to address tumor cells using suitable radiopharmaceuticals and achieve a high dose deposition inside the target structures. “Macrodosimetry” generally entails estimating the dose effect in organs (or dimensions of at least some millimeters) and is outlined in detail by the Medical Internal Dose (MIRD) Committee, the U.S. Society of Nuclear Medicine and the International Commission of Radiological Protection (ICRP) [1]. Microdosimetry on the other hand entails estimating the dose absorbed in microscopic objects, such as cells.

As an alternative to characteristic photon emissions, radionuclides decaying by electron capture or internal conversion may undergo a process known as the Auger effect. In the Auger effect, an electron from an outer shell fills the lower electron vacancy, but the energy released in the process is transferred to another orbital electron. This electron is then emitted from the atom instead of a characteristic X-ray [2]. The emitted electron is called an Auger electron, with ranges in tissue typically at the micro- or nanometer level [3]. Their unique property of depositing significant amounts of energy in minute volumes around the decay site opens up the possibility of using them as microscopic probes to study fundamental questions regarding the interaction of radiation with cells.

^{123}I is used mainly in nuclear medicine because of its ideal γ-ray energy (159 keV) and relatively short half-life (13.2 h). The decay of ^{123}I is, however, also associated with the production of Auger electrons. These low energy particles (< 500 eV) have a very short range in tissue (< 25 nm) and as a result induce biological damage similar to that of high linear energy transfer radiations such as 5 MeV α-particles, provided that the isotope is allowed to decay within the cell nucleus [4].

Dose deposition in cells can originate from extracellular media, intracellular uptake in a single cell and from surrounding cells. Knowledge of the absorbed dose is required for evaluation of the observed biological effects and to predict or compare the effectiveness of different radiation modalities. However, direct dose measurements in cells are impossible due to the small cellular dimensions [5].

According to the stochastic character of all of the decay processes, a large number of pathways exist by means of which a radioactive particle can decay and the excited atom can de-excite, i.e. each initial inner shell vacancy may cause a different number of Auger electrons to be emitted resulting in a more or less broad distribution of differently charged

ions. Because these electron transitions and particle interactions are random processes, the Monte Carlo technique is an appropriate tool for the simulation of Auger emissions and electron spectra, as well as a feasible method to obtain accurate absorbed dose values under consideration of all irradiation aspects like geometry and activity distributions [5], [6], [7]. Bingham *et al*. found that the dose delivered to the cell nucleus is underestimated by a factor of 7.4 for ^{123}I in cells with nuclear radius of 4 μm and cell radius of 12 μm when compared to conventional organ dosimetry, indicating the need of developing dosimetric calculations for electron emissions at a cellular level [8]. Bingham *et al.*'s observation, along with the noticeable lack of current research and associated literature concerning standardized dosimetric calculations at a cellular level, indicate the need for microdosimetry studies as well as investigating and methods to compare these dose estimations.

Geant4 is an open source Monte Carlo (MC) toolkit, based on object orientated programming rules using the C++ language, which provides functions for simulating the passage of particles through matter [9]. The code is freely downloadable from the Geant4 web site. Detailed descriptions of the toolkit design and the physical fundamentals may be found in the "Geant4 User's Guide for Application Developers" and the "Physics Reference Manual" [10], [11]. Besides the fact that it is entirely open-source and freely available to all users, the main advantage of this toolkit is its openness to modification and extensions.

Originally Geant4 was used to model high-energy physics interactions, but it now also includes low-energy physics processes necessary for medical applications. A user can create stand-alone programs or programs based upon other object-orientated applications. Regardless of the foundation of the program, the toolkit offers support from the initial problem statement to the rendering of results and graphics for publishing. Geant4 has at hand a plethora of physics models which describe the interactions of particles with matter across a wide range of energies. Data and expertise from across the world have been used and therefore Geant4 acts as a repository which incorporates a large part of all that is known about particle interactions [12]. All aspects of a simulation process have been built into the toolkit: the geometry of the experiment, the materials and fundamental particles under investigation, the tracking of particles through matter and electromagnetic fields, the physics processes describing particle interactions, the response of detector components, the production of event data, the stockpiling of events and tracks, the visualization of the environment and particle trajectories, and the storing and analysis of simulation data at different levels of detail and refinement.

1.2. Objectives & Aims

The level of biological effects of certain radiations is not always directly proportional to the dose they impart. Since the delivered dose on a cellular level is not directly measurable using

current instrumentation, scientists and physicians have developed correlations between the biological response and the exposed dose through experiment and amongst others, the theory of atomic physics. An alternative method of predicting the delivered dose in a cell is by using Monte Carlo simulations. These simulations however, have to describe the biological composition and geometries of the material as accurately as possible, as well as the interactions of different particles with the material and can therefore result in complex codes and extremely long computation times.

In our study, the aim was to determine (through experiments and using Monte Carlo simulations) the relative biological effectiveness[1] (RBE) of ^{60}Co irradiations and ^{123}I decays on isolated and stimulated human T-lymphocytes.

The first phase of experiments was the exposure of 3 different types of cells to γ-radiation using a ^{60}Co-teletherapy unit. The proposed cell lines were: human T-lymphocytes, rat brain endothelial cells (bEND5, a cell with high radiosensitivity) and Chinese hamster ovarian cells (CHO-K1, a cell with low radiosensitivity). The cells were exposed to graded doses of ^{60}Co γ-radiation, after which they were cultured and the micronuclei formations in binucleated cells were used to analyze the effects of γ-radiation on the cell types.

The second phase of experiments was the exposure of a known number of isolated and stimulated human lymphocytes to certain activities of ^{123}I for a discrete amount of time. The thymidine analogue 5-[^{123}I]-iodo-2-deoxyuridine (^{123}IUdR) was prepared and used to incorporate ^{123}I into the DNA of human T-lymphocytes. This was done such that the radionuclide could be transported across the cell and nuclear membrane to permit the deposition of Auger and Coster-Kronig electrons in close proximity to cellular DNA. After exposure, the samples were cultured to express residual radiation damage. The cellular damage was quantified by numerating the micronuclei (MNi) frequency in binucleated (BN) cells. The experiments were done at iThemba LABS under the supervision and guidance of Prof. J P Slabbert and Mr. P Beukes.

The experimental work followed the same approach as that of Slabbert *et al*. [13]. In the study they focused on the targeting and accumulation of ^{123}I in human lymphocytes and CHO-K1 cells. They found that the combined effect of intracellular and extracellular disintegrations of ^{123}I is about 3.7 times more potent on lymphocytes, compared to when the disintegration of the radionuclide is restricted to only the extracellular medium, among other results. It was concluded that this enhancement is due to the short range Auger electrons emitted by the isotope.

[1] No formal definition of RBE is defined since it depends on the experimental system being studied. Generally, RBE values indicate the relative effectiveness of two radiation qualities to produce the same biological response.

Next, we wished to recreate the above experiments through Monte Carlo simulations and thereby determine as accurately as possible the absorbed energy and dose due to the irradiations, specifically the energy and dose deposited by Auger electrons produced during the decay of ^{123}I.

We made use of the Monte Carlo based simulation code Geant4. The code was used to simulate the scenarios mentioned above.

We attempted to simulate the above ^{60}Co exposures as well. This simulation was an investigation into the irradiation of a macroscopic volume by a radioactive source. The geometry was set up to replicate the experimental setup with regards to the source location and type, collimation, build-up and backscatter, the Petri dish and cellular media. The individual cells were not used as detectors, only the effective volume in the Petri dish. The energy and the dose deposited by the ^{60}Co source (γ-rays, primary and secondary electrons) were then quantified by the Geant4 simulation.

Our main endeavor was to simulate the energy deposition from the decay of ^{123}I within a cell using Geant4. Basically, a geometry representing a biological cell (with the same volume, density, etc. as the proposed lymphocytes) was created as a detector to measure the dose, energy and particles traversing it due to a radionuclide prone to emit Auger electrons, i.e. ^{123}I. A similar simulation was performed by Bousis *et al.* (2012), using their in-house Monte Carlo code [14]. More advanced simulations involve the calculation of DNA strand breaks due to direct and indirect effects of Auger electrons as was demonstrated by Raisali *et al.* (2013) [15], [16], [17]. This was however not attempted in this investigation.

Furthermore, an empirical formula relating the activity (and consequently the absorbed dose) to the biological response was determined. The curves were compared to other dose-response curves from literature, thereby indicating if the simulations are a viable option for predicting accurate dose depositions. We could then calculate the RBE values from our dose-response curves and compare them to values available in literature.

Finally, we aimed to determine the accuracy and feasibility of Geant4 as a simulation toolkit for microdosimetry purposes. To this end we considered the practicality, effort and time spent using Geant4, and also by comparing the calculated RBE values and dose-response curves to those in literature.

Geant4 is an advanced, extensive and comprehensive simulation toolkit. Its advantage over similar packages with regards to availability, artistic and geometric freedom, physics models and materials libraries and openness to modification are proven. It is a very powerful simulation toolkit and can be used in a large number of areas of expertise as is shown by the examples supplied alongside the toolkit.

Chapter 2: Background

In the following sections we discuss some background information with regards to the field of radiobiology and the Geant4 Monte Carlo toolkit, and also give an extensive literature review on studies concerning the Auger electron effect.

2.1. Radiobiology

Radiobiology is a combination of two disciplines: radiation physics and biology. It is a branch of science concerned with the action of ionizing radiation on biological tissues and living organisms [18].

2.1.1. The cell cycle

The cycle of the eukaryotic[2] cell is in its simplest form grouped into an interphase, during which the cell grows and its DNA is replicated, and an M-phase where the DNA separates and the cell divides [19]. Interphase can be further partitioned into three subsections known as the S-phase (S for synthesis, where DNA is replicated), and the so-called gap phases G_1 and G_2 that define the beginning and end of interphase. Based on the appearance of the cell's chromosomes, the events of M-phase are grouped into mitosis (five stages: prophase, prometaphase, metaphase, anaphase, and telophase) and cytokinesis (the final stage where the cell divides) [19].

It is during the S-phase when radiolabeled thymidine analogues, such as iododeoxyuridine (IUdR) and bromodeoxyuridine (BrdU), can be used to incorporate radioactive elements into the DNA strand.

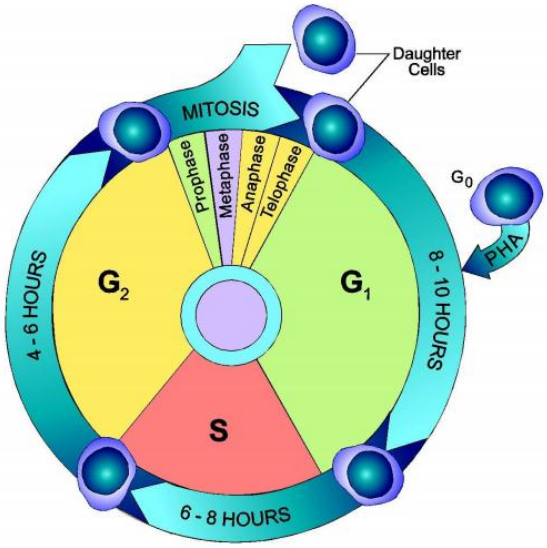

Figure 2.1. The cell cycle [20].

[2] Cells which contain a distinct membrane-bound nucleus.

DNA radiation damage can cause delays in 3 main cell progressions. The first delay is in the cell cycle checkpoint which involves the repair of damage and cell proliferation enhancement. The delay in repair, in the G_1 phase, could lead to the second cell progression delay which is the slowing down of DNA synthesis. Since synthesis in S-phase is delayed, cells cannot complete the M-phase on time and this leads, thirdly, to the delay of cell division [21]. Radiation-induced mitotic delay results primarily from damage to the cell nucleus rather than from damage to cytoplasmic structures or the membrane [22].

Human peripheral lymphocytes are a cell population which is predominantly in a DNA pre-synthetic stage of the cell cycle (i.e. the G_0 phase). Peripheral human lymphocytes can be stimulated to undergo *in vitro* mitoses using phytohaemagglutinin (PHA). Two main types of lymphocytes can be distinguished, i.e. T and B cells. On the basis of their surface markers, T and B cells comprise a mixture of cells with differing life spans and differing roles in the immunological processes. It is the T cells, mostly of the $CD4^+$ and $CD8^+$ subtypes, which are stimulated *in vitro* by PHA and are used for biological dosimetry [20].

2.1.2. Radioactive emissions and their properties

Radiations of primary concern originate in atomic or nuclear processes. They are categorized into four general types: fast electrons, heavy charged particles, electromagnetic radiation, and neutrons. *Fast electrons* include β-particles (positive or negative) emitted in nuclear decay, as well as energetic electrons produced by any other process. *Heavy charged particles* denote a category that encompasses all energetic ions with mass of one atomic mass unit or greater, such as α-particles (He-nuclei), protons or fission products. The *electromagnetic radiation* of interest includes X-rays emitted in the rearrangement of electrons in the shells of atoms, and γ-rays which originate from transitions within the nucleus itself. *Neutrons* generated in various nuclear processes are often further divided into *slow neutron* and *fast neutron* subcategories [23].

The *activity* of a radioisotope source is defined as its rate of decay, and is given by the fundamental law of radioactive decay

$$\frac{dN}{dt} = -\lambda N$$

where *N* is the number of radioactive nuclei and λ is defined as the decay constant. The historical unit of activity has been the *curie* (Ci), defined as exactly 3.7×10^{10} disintegrations / second, but has been replaced by its SI equivalent, the *Becquerel* (1 Bq = 1 disintegration/sec).

A radioactive parent X with atomic number Z and atomic mass number A decays into a daughter Y through the following possible modes of decay: α, β^-, β^+, electron capture (EC). Nuclear relaxation emissions include γ emission and internal conversion (IC) [18].

In α decay:

$$^{A}_{Z}X \rightarrow {}^{A-2}_{Z-2}Y + {}^{4}_{2}He(\alpha)$$

A ^{4}He nucleus, referred to as an α particle, is emitted during the decay.

In β^- decay:

$$^{A}_{Z}X \rightarrow {}_{Z+1}{}^{A}Y + \beta^- + \bar{\nu}_e$$

A neutron transforms into a proton, and an electron (β^-) and antineutrino ($\bar{\nu}_e$) sharing the available energy, are ejected from the nucleus.

In β^+ decay:

$$^{A}_{Z}X \rightarrow {}_{Z-1}{}^{A}Y + \beta^+ + \nu_e$$

A proton transforms into a neutron, and a positron (β^+) and neutrino (ν_e) sharing the available energy, are ejected from the nucleus. The positron, usually within a few millimetres of the site of its origin, then combines with an electron in an annihilation interaction and their masses are converted into energy in the form of two back-to-back 0.511 MeV annihilation photons.

In electron capture (EC):

$$^{A}_{Z}X + e^-_K \rightarrow {}_{Z-1}{}^{A}Y + \nu_e$$

The nucleus captures one of its own K shell orbital electrons, a proton transforms into a neutron, and a neutrino is ejected.

In γ emission:

$$^{A}_{Z}X^* \rightarrow {}^{A}_{Z}X + \gamma$$

An excited nucleus $^{A}_{Z}X^*$ attains its ground state $^{A}_{Z}X$ through emission of one or several photons (γ). The energies of the emitted γ-rays are unique to each element; hence the emission spectra can be used to determine the type of element.

In internal conversion (IC):

$$^{A}_{Z}X^* \rightarrow {}^{A}_{Z}X + e^-_K$$

Rather than being emitted as a γ photon, the nuclear excitation energy may be transferred to a K shell orbital electron that is ejected with a kinetic energy equal to the excitation energy minus the orbital electron binding energy. The resulting K shell vacancy is filled with a higher level orbital electron and the transition energy is emitted in the form of characteristic X-ray photons or Auger electrons.

In the Auger effect, an electron from an outer shell fills a lower vacancy, but the energy released in the process is transferred to another orbital electron. This electron is then emitted from the atom instead of a characteristic X-ray [2]. The kinetic energy of an Auger electron is

equal to the difference between the binding energy of the shell containing the original vacancy and the sum of the binding energies of the two shells having vacancies after the emission. Two orbital vacancies exist after the Auger effect occurs. These are filled by electrons from the other outer shells, resulting in the emission of additional characteristic X-rays or Auger electrons. A Coster-Kronig (CK) transition is an Auger transition in which the atomic shell vacancy is filled by an electron from a higher subshell of the same shell. In the following paragraphs and sections, the term “Auger electrons” will be used to refer to the CK electrons as well as Auger electrons.

The decay of ^{123}I is associated with the production of Auger electrons [24]:

$$^{123}_{53}\mathrm{I} \xrightarrow{EC} {}^{123}_{52}\mathrm{Te}^{*} + \nu_e$$

^{123}I ($T_{1/2}$ = 13.2234(37) h) decays to ^{123}Te ($T_{1/2}$ = 12 × 10^{12} y) by electron capture (EC, 100%).

The EC process may lead to different nuclear excited ^{123}Te states depending on the branching ratios. Most frequently (97.18%) the decay goes to the 158.99 keV level through the emission of a 1.070 MeV mono-energetic neutrino (the ^{132}Te atom mat have some kinetic energy as well).

The excited Te-nucleus then decays by the emission of a 158.99 keV γ-ray with emission probability of 83.25%; or by IC electron emission (127.17 keV) with emission probability of 13.72%, leading to Auger electron cascades and/or X-ray emissions.

The EC process leaves the ^{123}Te atom with a vacancy in one of its electron orbitals, most probably the K-shell. This vacancy may result in the emission of X-rays and/or Auger electrons. The characteristic X-ray emissions of ^{123}I are 27.2 keV (emission probability of 24.7%) and 27.5 keV (emission probability of 46.0%).

Since only ~14% of the ^{123}I decays result in IC electron emissions, only this percentage of decays give rise to two possible Auger cascades. The decay level scheme of ^{123}I can be seen in Appendix A, long with a summary of the energies of the particles emitted in Table 5.1.

For use in radiobiology and radiation protection and radiotherapy the physical quantity that is most useful for defining the quality of an ionizing radiation beam is the linear energy transfer (LET). Also referred to as stopping power, the LET focuses attention on the linear rate of energy absorption by the absorbing medium as the charged particle traverses the medium and the typical unit for the LET is keV/μm [18]. Basically it represents the density of ionisations in the particle tracks. Typical LET values for commonly used radiations are given in Table 2.1.

Table 2.1. Typical LET values for commonly used particles [18].

Particle type	*LET*
250 kVp X-rays	2 keV/μm
^{60}Co γ-rays	0.3 keV/μm
3 MeV X-rays	0.3 keV/μm
14 MeV neutrons	12 keV/μm
Heavy charged particles	100 – 200 keV/μm
1 keV electrons	12.3 keV/μm
10 keV electrons	2.3 keV/μm
1 MeV electrons	0.25 keV/μm

X-rays and γ-rays are considered low-LET (sparsely ionizing) radiations, while energetic neutrons, protons and heavy charged particles are high-LET (densely ionizing) radiations. The discrimination value between low- and high-LET is ~10 keV/μm [18]. It is clear that the LET increases with decreasing electron energy, necessitating the investigation into the ionising properties of low energy electrons.

2.1.3. Radiosensitivity

Radiosensitivity is the relative vulnerability of cells to the harmful effect of ionizing radiation. In general, cell populations which divide quickly have a high percentage of cells in the S-phase which are most radio-resistant. Cells in M and G_2 phases are most radiosensitive [18], [25], [26], [27].

Large variations in radiosensitivity for cells in culture exist when exposed to low-LET radiations, and a general reduction in the variation of radiosensitivity of different cell lines is found with increasing ionization density (high-LET) [28].

The biological effects of radiation exposures result mainly from damage to the DNA, which is the most critical target within the cell; however, there are also other sites in the cell (e.g. mitochondria) that, when damaged, may lead to cell death [18].

2.1.4. Micronucleus assay

A standard method used to determine the combined effects of ionizing radiation-induced damage and repair is cytogenetic analysis (or analysis of chromosomes). Chromosomal aberrations resulting from non- or mis-repaired radiation-induced double strand breaks can be detected using such methods.

The cytokinesis-blocked cytome assay is one such cytogenetic analysis method [29]. The "cytome" concept implies that every cell in the system studied is scored cytologically:

- for its viability status (necrosis[3], apoptosis[4]),
- its mitotic status (mononucleated, binucleated (BN), multinucleated[5]), and
- its chromosomal damage or instability status (presence of micronuclei (MNi), nucleoplastic bridges (NPBs), nuclear buds (NBUDs)).

This assay is a comprehensive system for evaluating DNA damage, mitotic status and cytotoxicity. DNA damage events are scored and include MNi, a biomarker of chromosome breakage and/or whole chromosome loss; NPBs, a biomarker of DNA misrepair and/or telomere end-fusions; or NBUDs, a biomarker of elimination of amplified DNA and/or DNA repair complexes.

To analyze the effects of radiation exposure of cells in a particular phase of the cell cycle, cells can be synchronized (with or without chemicals) or handled in a particular way to enhance the proportion of cells in the phase of interest. Non-stimulated lymphocytes are in the G_0 phase of the cell cycle at the time of irradiation. However, when exponentially growing cell lines are used, a heterogeneous population of cells residing in different phases (usually G_2 or S) of the cell cycle is irradiated.

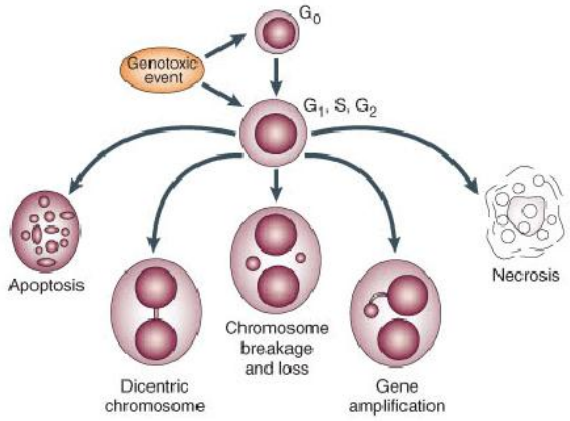

Figure 2.2. The various possible fates of cultured cytokinesis-blocked cells following radiation exposure. Using these biomarkers in the assay, it is possible to numerate chromosome breakage (MNi), chromosome loss (MNi), dicentric chromosomes (NPBs), gene amplification (NBUDs), necrosis and apoptosis [29].

After *in vitro* irradiation, cells are blocked from performing cytokinesis by the addition of cytochalasin-B (cyt-B). Cyt-B is an inhibitor of actin polymerization required for the formation of the microfilament ring that constricts the cytoplasm between the daughter nuclei during cytokinesis [30]. Since nuclei can still divide, after one division, cells will consequently appear as BN cells.

Although the micronucleus assay is generally applied using lymphocytes, micronuclei can be detected in all types of eukaryotic cells; as long as they are capable of division.

[3] Unexpected and accidental cell death.
[4] Programmed cell death.
[5] A cell with more than one main nucleus.

MNi, result from the radiation damage and are small extranuclear bodies detected around the main nuclei. MNi are formed from acentric chromosome fragments (chromosome breaks lacking centromeres) and/or whole chromosomes that lag behind in anaphase and are left outside the daughter nuclei in telophase [31]. At telophase, a nuclear envelope forms around the chromosomal fragments or lagging chromosomes, which then uncoil and gradually assume the morphology of an interphase nucleus with the characteristic that they are smaller than the main nuclei.

The micronucleus assay allows for a more rapid assessment of radiation damage in cells compared to the scoring of chromosomal aberrations in metaphase, and radiation induced micronuclei stem from acentric chromosome fragments which are directly associated with dicentric formations. Therefore MNi provide a convenient and reliable index of both chromosome breakage and loss; and as the number of radiation-induced MNi is strongly correlated with radiation dose and quality, the MN assay is an appropriate test for biological microdosimetry [32].

The resulting DNA damage due to the radiation can be quantified by numerating the number of MNi per BN cell. To analyse the obtained results, the number of MNi per BN cell can be normalized to 500 BN or 1000 BN cells. This value is then plotted against the exposed dose and a dose-response curve is fitted to the data points. The curve usually has the linear-quadratic form:

$$y = c + \alpha \cdot D + \beta \cdot D^2 \tag{2.1}$$

In the above equation, *y* represents the number of micronuclei (per 500 or 1000 BN cells) induced by a dose *D*. Depending on the cell line and radiation quality, the quadratic coefficient *β* may be very prominent or not at all. For high LET radiation, the α-term becomes large and eventually the β-term becomes biologically less relevant and also statistically 'masked' and the dose response is approximated by a linear equation. The intrinsic MNi of the cell culture *c* can be subtracted (obtained from the control sample which was not exposed to any radiation) from each data point before the line fitting is done, resulting in the following equation:

$$y = \alpha \cdot D + \beta \cdot D^2 \tag{2.2}$$

MetaSystems developed and commercialized an automated MN scoring module for the Metafer 4 platform which allows the automated finding of BN cells and the subsequent scoring of MNi in these cells [33]. In short, the system identifies BN cells as two similar nuclei, close to each other, but completely separated. Classifiers determine what the system regards to be a BN cell by defining how similar the nuclei are in shape and size, and by defining a maximal distance between the two nuclei. To exclude trinucleated cells, the classifier defines a circular region of interest around the two daughter nuclei wherein no other

nuclei (of a certain size) may be found. When a BN cell is identified, the system will apply a second set of classifiers to define what a micronucleus is. These classifiers will define a circular area around the daughter nuclei in which the system searches for MNi. The size and the shape of the MN are also defined in the classifier [34]. The diameters of MNi in human lymphocytes vary between 1/16th and 1/3rd of the mean diameter of the main nuclei [29]. We can further validate the system by visually checking the BN cell gallery shown after each scan, resulting in a semi-automated MN scoring procedure.

Attention should be given to ensure that MNi are scored only in BN cells and not in other multinucleated cells because multinucleated cells with more than two main nuclei tend to have greatly elevated MNi frequencies relative to BN cells, which would result in inaccurate genome damage estimates [29]. This issue is particularly prominent in dense cell preparations, because it may be difficult to distinguish between two individual cells or cell types. For this reason, it is important to optimize the Cytokinesis-block micronucleus cytome assay protocol to maximize the frequency of BN cells and at the same time minimize the frequency of multinucleated cells.

Varga *et al*. reports that DAPI (4',6-diamidino-2-phenylindole, Vector Laboratories, Brussels, Belgium) is more suitable for automated micronucleus scoring, as it has the highest specificity to DNA and has a high fluorescence yield which result in a clear fluorescent picture of the 2 daughter nuclei and the micronuclei in the cytoplasmic background [33]. Furthermore, by using DAPI mixed in vectashield (anti-fade), the staining procedure is simplified to dropping vectashield + DAPI on the slide, followed by a cover slip.

Along with the number of micronuclei per binucleated cell, the binucleation index can also be determined. This is the fraction of all of the cells which were scored but had two main nuclei.

2.1.5. Relative Biological Effectiveness (RBE)

As the LET of radiation increases, the ability of the radiation to produce biological damage also increases. In radiobiology the RBE is expressed by the ratio of the absorbed doses of two different radiation qualities which produce the same specified effect:

$$RBE = \frac{Dose\ from\ reference\ radiation\ to\ produce\ a\ given\ biological\ effect}{Dose\ from\ test\ radiation\ to\ produce\ the\ same\ biological\ effect}$$

The dose can be determined by solving for *D* in equation (2.2). This value is dependent on the spatial distribution of the energy imparted, the density of ionisations per path length of ionising particles and the reference radiation [35]. No convention exists defining the standard reference radiation, although γ-rays from ^{60}Co or ^{137}Cs and 250 kVp X-rays have generally been used. The ICRP-ICRU RBE Committee defined a single and maximum representative RBE value as the RBE at minimal doses. Known as the dose limiting RBE (RBE_M, M for

maximum), it is expressed by the ratio of the initial slopes (the α-coefficients) of the dose-effect curves for the studied radiation and the reference radiation:

$$RBE_M = \frac{\alpha_{test}}{\alpha_{ref}}$$

The ICRP has assigned radiation weighting factors w_R to specified radiation types to be used in the calculation of equivalent dose (mostly used in radiation protection). Although no mathematical relationship between w_R and RBE exists (due to the varying definition of RBE), the w_R represents the relative biological effectiveness of the radiation. Per definition, an equivalent dose of radiation is estimated to have the same biological effect as an equal amount of absorbed dose of gamma rays (which has w_R = 1). Auger electrons emitted from nuclei bound to DNA are an exception from the ICRP Publication 60 recommendation for dosimetry of low energy electrons [36]:

"Auger electrons emitted from nuclei bound to DNA present a special problem because it is not realistic to average the absorbed dose over the whole mass of DNA as would be required by the present definition of equivalent dose. The effects of Auger electrons have to be assessed by the techniques of microdosimetry."

The LET values for Auger and low-energy electrons are higher than those for high-energy beta emitters or photons and therefore generally result in higher RBEs [37].

2.2. Monte Carlo simulations: Geant4

Geant4 is an open source Monte Carlo toolkit based on object orientated programming rules using the C++ language, created and developed for high energy particle simulations at CERN. It is a free software package composed of tools which can be used to accurately simulate the passage of radiation (particles) through matter [9], [12].

The code is freely downloadable from the Geant4 web site as well as detailed descriptions of the toolkit design and the physical fundamentals may be found in the "Geant4 User's Guide for Application Developers" and the "Physics Reference Manual" [10], [11].

This toolkit was successfully used by McNamara *et al*. (2012) to investigate the low energy secondary electron track structures produced by X-ray and proton beams in liquid water [38]. The low energy models of Geant4 were specifically used to evaluate the ionization cluster size distribution as well as the radial dose deposition of the two beams using the ionization cluster size distribution as well as the radial dose deposition of the beam. Monte Carlo simulations have shown that electrons with energies less than 1 keV can produce approximately 50% of all ionisations and can be correlated with the high biological effectiveness of such radiation on the nanometer scale.

2.2.1. Detector construction, Primary event generator, and Physics list

The `main()` method is implemented by two toolkit classes, the run manager (which controls the flow of the program and manages the event loops within a run and is also responsible for managing initialization procedures, including methods in the user initialization classes) and the user interface manager (needed for the user to issue commands to the program and to display information at the run, event and tracking levels of simulation); and three mandatory user classes: the detector construction, the primary event generator, and the physics list. Two of them are user initialization classes (derived from the base classes `G4VUserDetectorConstruction` and `G4VUserPhysicsList`) and the other is a user action class (`G4VUserPrimaryGeneratorAction`). In the `main()`, the random number generator (an engine which implements the basic algorithm for pseudo-random numbers generation) to be used in the Monte Carlo simulations is defined as well.

The `DetectorConstruction` class requires the user to define the geometries. A detector-geometry in Geant4 is made of a number of volumes. Each volume is created by describing its shape and its physical attributes, and then placing it inside a containing volume (the largest volume is called the “World” volume). To describe a volume's shape, the concept of a “solid volume” is used. A solid volume is a geometrical object that has a geometric shape and specific values for each of that shape's dimensions (e.g. a cube with sides of 10 cm). To describe a volume's material properties, a “logical volume” is used. It includes the geometrical properties of the solid volume and adds physical characteristics such as composition and density (e.g. a cube made out of water). Geant4 makes use of the definitions of materials supplied by the USA National Institute of Standards and Technology (NIST) materials database, or a user can define their own material e.g. using chemical compositions. To position the volume in the simulation, the user creates a “physical volume”, which places a copy of the logical volume inside a containing volume (e.g. a cube whose center is placed at the origin of the world volume) [39].

The `PhysicsList` requires the user to define all particles and physics processes (which describe how the particles must interact with other particles) to be used in the simulation. The “range” cut-off parameter should also be defined in this class. Geant4 provides seven major categories of processes: electromagnetic, hadronic, transportation, decay, optical, photolepton-hadron, and parameterization. For a given simulation, a number of physical processes are assigned to each particle type. To each of these processes, several models and cross section data sets are assigned; e.g. for the hadronic processes, the user must choose the models which are most appropriate to the energy range and level of detail required in their simulation. A Geant4 user may wish to write their own Physics List class, but to aid in and simplify the simulation Geant4 provides reference Physics Lists – combinations of models and processes predefined inside the Geant4 toolkit. An example of one of these

reference physics lists is QBBC; created for space applications, radiation biology, and radiation protection. It includes combinations of Binary cascade (BIC), BIC-ion, Bertini cascade, Chiral Invariant Phase Space, Quark Gluon String, Fritiof and Pre-compound models which describe hadronic interactions [40]. In general the interactions to be considered depend on the type of particle and its energy as well as those of the target particle or the material's properties. For example, the electromagnetic interactions include the Compton effect; Photoelectric effect; pair production; Rayleigh scattering and photonuclear interactions. Of these the first three are the important inelastic interactions resulting in the transfer of energy to atomic electrons and the last two are elastic interactions resulting in deflection of the incoming photons through a small angle and no energy loss. Pair production and photonuclear interactions are only important above MeV photon energies [41].

Geant4 tracks particles down to zero energy, but simulation performance is steered using "production cuts". These thresholds determine the minimal energy transfer to a secondary particle, so that the secondary particle is considered in the simulation [5]. The production cuts for secondaries can be specified as "range cuts", which are converted at the initialization of the program into energy thresholds for secondary gamma, electron, positron and proton productions [10]. The energy cut is still set to 990 eV even if a range cut equivalent to an energy lower than 990 eV is specified. In order to decrease this value (down to a minimum of 250 eV, to see low energy emission lines of the fluorescence spectrum for example), the user must set this threshold manually. This lower production cut will however increase the computational time. Physics processes (e.g. elastic scattering) however do have a threshold below which the incident particle is killed (stopped and the kinetic energy is locally deposited).

Lastly, the `PrimaryGeneratorAction` requires the user to define how a primary event should be generated. This involves setting the type of particle (e.g. an electron, or a neutral ^{123}I-atom), its starting position, momentum, and energy. More complicated primary events, such as randomly selecting photons from a spectrum of predefined energies and shooting them in certain directions, can be defined as well but requires more computational involvement from the user.

2.2.2. Run action, Event action, Tracking action, and Stepping action

In Geant4, `Run` is the largest unit of simulation. A "run" consists of a sequence of events, each started by the primary event generator. An "event" consists of particles each having a track assigned to them. Each "track" consists of number of steps. A "step" is the smallest unit of simulation in Geant4.

Within a run the detector geometry, the set-up of sensitive detectors (scoring volumes), and the physics processes used in the simulation should be kept unchanged. A run starts with the `BeamOn()` method of the run manager and ends when the last step of the last track of the last event is simulated. An event is started by the primary event generator. The entire event includes all the secondary particles and their interactions which may result from the primary event.

A track is assigned to each particle produced in an event. The track can be segmented into a number of steps; the size of which can be limited by the physics list and is dependent on the particle type and its energy. The track ends when the particle leaves the world volume, is killed in a process or has zero energy left.

A step holds the transient information of a particle's step. This includes the two endpoints of the step, `PreStepPoint` and `PostStepPoint`, which contain the points' coordinates and the volumes containing the points. It also consists of the change in track properties between the two points. These properties, such as energy and momentum, are updated as the various relevant processes are invoked. Some physics processes are sampled not at the beginning or the end of the step, but along the step (such as atomic de-excitation).

A user can define or utilize predefined functions and procedures to access and calculate the values they require at the beginning or at the end of the run, an event, a track, or a step.

2.2.3. Low energy processes

The Geant4 electromagnetic physics processes are able to describe photon interactions with matter. Photon processes are purely discrete, simulating explicitly all interactions on a step-by-step approach. These processes encompass the photoelectric effect, Compton scattering, pair production and Rayleigh scattering [42].

Historically, the Geant4 electromagnetic processes have been categorized and implemented into the "standard" and "low energy" sub-packages. The "standard" sub-package was initially designed for the large scale production of simulations related to high energy physics experiments (such as those at the Large Hadron Collider at CERN) but has been expanded to other application domains, such as medicine and space, covering the 1 keV – 10 PeV energy ranges. The "low energy" sub-package includes alternative electromagnetic physics models reaching the ~100 eV low energy limit and can simulate atomic shell effects, such as fluorescence emission and Auger electron production (atomic de-excitation). The "standard" models are based on analytical expression, whereas the "low energy" models are based on the publically available Livermore evaluated data libraries (EADL, EEDL, and EPDL97) or on a re-engineering of the 2001 version of the Penelope Monte Carlo code [42]. The "low

energy" physics processes are conveniently predefined in two Geant4 reference physics lists: G4EmLivermorePhysics and G4EmPenelopePhysics.

For charged particles, elastic scattering can be approximated by the multiple scattering model of Urban especially adapted for the "standard" Geant4 processes (''G4hMultipleScattering'' class) [11]. The model is based on the Lewis multiple scattering model (1950) taking into account angular deflection and spatial displacement of the particle, without the usual small angle approximation, giving relatively good results for small and large angles according to Lewis (1950). Basically the cumulative effect of all of the actual small angle deflections is a net deflection from the original particle direction (see Figure 2.3). Since the "standard" processes (including multiple scattering) are recommended for energies above 1 keV in Geant4, this energy restriction is also recommended for the Geant4-DNA charged particle processes above 1 keV. Francis *et al*. noted that it is hard to find reliable scattering data for ions below 1 keV in liquid water [43].

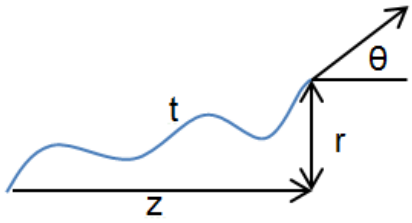

Figure 2.3. Multiple Scattering approximation of a charged particle's track *t*.

Currently the Geant4-DNA project, initiated by the European Space Agency, is under improvement. The project's goal is to combine simulations of different radiation effects in the human body using the Geant4 toolkit and should provide predictions of biological effects at the cellular level for complex geometrical setups of shielding materials and biological targets [40]. This project includes the development of specific electromagnetic physics models down to the sub-eV scale to simulate physical interactions with the DNA bases, the inclusion of water radiolysis for the production of oxidative radical species, and the development of realistic biological geometries, in order to simulate direct and indirect ionizing radiation effects at the DNA scale [42]. To date, it includes discrete electromagnetic physics models applicable to electrons (0.025 eV – 1 MeV), protons (1 keV – 100 MeV), alpha particles (10 keV – 40 MeV), H, C, N, O, and Fe (1 keV – 100 MeV) and their charged states [43]. In the Geant4 9.4.6 version, these models are specific to the liquid water medium, where water is treated as a molecule, and from version 10 it includes silicon as well [44], [45]. Photon interactions are based on the Geant4 Livermore models and they are included by default in the Geant4_DNA physics constructor. In the current version of Geant4-DNA, electrons can be transported between 8 eV and 1 MeV. Three types of physical processes are considered: ionization, excitation and elastic collisions [17]. If the Geant4-DNA processes are combined with other Geant4 electromagnetic processes (e.g. the photon processes) which use cuts for

secondary production, the default production cuts are set (990 eV), unless changed by the user. The Geant4-DNA processes are all discrete processes; as such they simulate explicitly all interactions and do not use any production cuts, hence the default 990 eV cut will have no effect on the Geant4-DNA Physics results [44].

Electrons with energies below 8.22 eV, which corresponds to the energy of the last excitation state for water molecule, do not have enough energy to undergo further ionisation or excitation processes. The only remaining processes are vibrational excitations (minimum of 2 eV) and elastic scattering (kill at 9 eV) and electron attachment that can occur between 8 and 13 eV as described by Melton (1972) [43]. The vibrational excitations and elastic scattering low energy limits can be extended down to 0.025 eV, but these are not set by default and have not been experimentally validated [44].

Two different data sets are available for electron elastic scattering. The first one uses the Rutherford model with screening effects taken into account for electrons above 200 eV described by Emfietzoglou *et al*. (2000), while the formula proposed by Brenner and Zaider (1983) was used for electrons below 200 eV. The second set uses the models published by Aouchiche *et al*. (2008) and Champion *et al*. (2009) for electrons (10 eV - 10 keV) and positrons in liquid and gaseous water [43]. The implementation in Geant4 however, is limited to energies greater than ~8 eV [15].

For ionisation and excitation inelastic cross-sections, the Plane-Wave First Born Approximation (FBA) is used considering the dielectric formalism and for K-shell, the model proposed in ICRU report 55 (1996) is applied. For very low electron energies (< 1 keV, when the incident electron speed approaches the speed of electrons orbiting the target molecule) the FBA is not successful. For such electron ionisations, the FBA is corrected using classic Coulomb-field correction and the exchange correction terms of Dingfelder *et al*. (1998) as proposed in ICRU report 37 [46]. The ionization energies are taken from Dingfelder *et al*. (1998) and excitation energies from Emfietzoglou (2002, 2003) [15], [47], [48].

2.2.4. Radioactive Decay and Relaxation

The `G4RadioactiveDecay` and associated classes are used to simulate the decay, either in-flight or at rest, of radioactive nuclei by α, β^+, and β^- emission and electron capture. It is a non-default process which must be registered with a process manager in the physics list. The simulation model depends on data taken from the Evaluated Nuclear Structure Data Files (ENSDF) which provides information on nuclear half-lives, nuclear level structure for the parent or daughter nuclide, decay branching ratios, and the energy of the decay process. If the daughter of a nuclear decay is an excited isomer, its prompt nuclear de-excitation is treated using the `G4PhotoEvaporation` class (similar to atomic relaxation) [11].

Atomic relaxation (de-excitation) processes can be induced by any ionization process that leaves the interested atom in an excited state (i.e. with a vacancy in its electronic shells). Currently the processes inducing atomic relaxation in Geant4 are the photoelectric effect, ionization, Compton scattering, internal conversion and electron capture processes. Geant4 uses the Livermore Evaluation Atomic Data Library (EADL) which contains data to describe the relaxation of atoms back to neutrality after they are ionized. Data in the EADL includes the radiative and non-radiative transition probabilities for each sub-shell of each element, for Z=1 to 100. Once the atom has been ionised by a process that has caused an electron to be ejected from an atom, leaving a vacancy in a given subshell, the EADL data are then used to calculate the complete radiative (X-rays) and non-radiative (Auger electrons) spectrum of particles emitted as the atom relaxes back to neutrality. Non-radiative de-excitation can occur for example via the Auger effect (the initial and secondary vacancies are in different shells) or Coster-Kronig effect (transitions within the same shell). Auger effects are only considered for $5 < Z < 100$ and always based on the EADL data tables, but only for those transitions which have a probability to occur of more than 0.1% of the total non-radiative transition probability. EADL probability data used are normalized to one for Fluorescence + Auger. Fluorescence is activated by default in the low energy physics lists, but the Auger effect and Particle Induced X-ray Emission (PIXE) should be activated by the user [11].

2.3. Literature review – The Auger and Coster-Kronig electrons

Two key features of Auger emitters have attracted the attention of the biomedical community: the short range of most Auger electrons and their resultant high cytotoxicity. Auger electron therapy is a promising form of molecular radiotherapy and has recently made the transition from the laboratory to the clinic. A term has been coined, targeted radioimmunotherapy (tRIT), to emphasize the unique characteristics of the short range but highly cytotoxic Auger electrons. Yasui (2012) gives an in depth review on recent Auger emitter research with an emphasis on findings on targeting, accumulation and mechanisms of action of Auger emitters in tumor cells [49].

A study by Bousis *et al*. (2012) was done using an in-house Monte Carlo code to investigate single-cell dosimetry of ^{123}I, ^{125}I and ^{131}I for tRIT of B-cell lymphoma. They found that ^{125}I gave the highest absorbed dose and ^{123}I the highest absorbed dose rate. Although, under the more realistic scenario of biological excretion from cells and from a dosimetric point of view, ^{123}I might be preferable to the other two radioiodines in the treatment of microscopic diseases in B-cell lymphoma patients [14].

2.3.1. Emission spectra

Sastry presented a review article for the AAPM of the physical and radiobiological data of the Auger emitter ^{125}I which was available in 1992 [50]. It was noted that the complete Auger and Coster-Kronig electron spectrum has not been measured for ^{125}I or any other Auger emitter. Reliable experimental data for ^{125}I for the K and L spectra are available, but the rest of the spectrum has to be calculated using theoretical transition rates and energies, approximations, and phenomenology - revealed by experimental and theoretical atomic research. In the review, spectra by the following groups were compared – Charlton & Booz (1981), and Howell (1992) using MC codes and theoretical transition rates and available binding energies; Pomplun (1987) using Dirac-Fock codes developed by Desclaux (1975); and phenomenological spectra by Sastry & Rao (1984). The spectrum of Pomplun differed substantially from the others because of multi-vacancy configurations and isolation assumptions that were made. It was shown from the reviewed spectra that the influences of the N- and O-shell are significant in electron spectra of Auger emitters.

Studies which did not address the N- and O-shell Auger electrons

The 1983 document by the International Commission on Radiological Protection (ICRP) provides nuclear transformation data and associated decay scheme drawings [51]. The energies and yields of the various electron energy states are those tabulated by Servier (1972) and the X-ray energies are of Bearden and Burr (1967). The document is based on the evaluated nuclear structure data files (ENSDF). The ENSDF data are part of the computer database of the National Nuclear Data Center at Brookhaven National Laboratory, from which the radioactive decay data are published in the periodical 'Nuclear Data Sheets' (Academic Press, New York). The ENSDF were subject to review in terms of consistency with the latest nuclear parameters, by comparing the computed energies of emitted radiations with total decay energies. The fundamental decay properties in the ENSDF, such as total decay energy (Q-values), branching fractions, excitation energies of isomers, physical half-life, and spin and parity of the initial and final states, were used in order to calculate the energies E (MeV) and yields Y ($Bq^{-1} \cdot s^{-1}$) of alpha particles, beta particles, gamma rays including annihilation photons, internal conversion electrons, X-rays, and Auger and Coster - Kronig (CK) electrons. The electron-binding energies are taken from the evaluated atomic data library (EADL) of Perkins *et al*. (1991).

Studies which did address the N- and O-shell Auger electrons

Charlton and Booz (1981) introduced a Monte Carlo method for calculating the electron spectrum following the decay of ^{125}I. The vacancy distributions after electron capture and

internal conversion are those of Behrens and Jänecke (1969), and the electron binding energies of Bearden and Burr (1967) were used. The work of McGuire (1972 & 1975) on the evaluation of the electron transition probabilities for the L-, M-, and N shells were incorporated. Charge neutralization was considered by filling O-shell vacancies during the cascade process. It was shown that different numbers of electrons are emitted depending on whether the atom is isolated or in the condensed phase. The average number of electrons emitted per ^{125}I decay for the condensed phase is 21.2 and 13.2 for an isolated atom (no charge neutralization) [52].

Humm *et al*. (1989) used the Monte Carlo code developed by Charlton and Booz (1981) to obtain the number and energies of electrons released by individual ^{125}I decays. These spectra were used alongside Berger's point kernels (1973, [53]) to calculate the mean energy per decay deposited in a cell nucleus, assuming a random distribution. They reported that the mean energy deposited in an 8.0 μm diameter nucleus per ^{123}I decay was approximately 4.879 keV [54].

Howell presented a report in 1992 for the AAPM to provide extremely detailed Auger electron spectra for commonly used radionuclides as opposed to the conventional spectra provided by the MIRD Committee and the ICRP [4]. The assumptions and techniques used by Sastry and Rao (1984), Humm (1983), Howell *et al*. (1985) and the MC code of Charlton and Booz (1981) were used in the report to calculate the spectra. All decay schemes and nuclear data are from Nuclear Data Sheets (for ^{123}I by Tamura *et al*. 1980). For Auger and CK transition rates, the values were obtained from Chen (1979) and McGuire (1972 & 1975). For O-shell rates, the work of Kassis *et al*. (1983) was used. Radiations with yields of less than 10^{-3} were excluded because they constitute a negligible contribution to the absorbed dose compared to the more abundant radiations. In the calculations, they assumed any vacancies created in the valence shell would be filled immediately. This fast neutralization approach is assumed in most condensed phase spectra. Recent experiments by Rao and co-workers on radioprotection against Auger cascades from DNA bound ^{125}I indicate that the indirect action of radical species plays a major role in causing damage to the radiosensitive targets, thereby suggesting a limited role for charge neutralization in the Auger effect in the condensed phase. Howell noted that the conventional spectra published by MIRD and ICRP result in a net emitted energy 3.5 times smaller than their detailed spectra. This difference is significant in that it points out the importance of low-energy Auger electrons in dosimetry in volumes with diameters < 1 μm and confirms that conventional spectra are inadequate for such purposes. They proposed a radiation waiting factor w_R of 20 for DNA-incorporated Auger emitters causing stochastic effects, based on the experiments of Howell *et al*. (1993), performed with a mouse testes model, showing that there is a linear relationship between the RBE of ^{125}I and the fraction of activity bound to DNA. They reported that approximately 14.9

Auger electrons are emitted on average per decay of ^{123}I. The following assumptions were highlighted in the report:

- The first assumption is that the electron transition probability data used are for atoms containing only a single inner shell vacancy (frozen orbital approximation). As the electron-cascade in the atom progresses, the number of vacancies rapidly increases, and the effect of multiple vacancy configurations on the transition rates is not known. Whereas the calculated yields and energies of the higher-energy Auger electrons agree well with experimental data, data on the very-low-energy electrons are limited.
- The second major assumption concerns the calculation of Auger electron energies. With the exception of the spectra of Pomplun *et al*., all the Auger spectra calculations have used the (Z + 1) approximation of Chung and Jenkins. However, it should be pointed out that the frozen orbital approximation was also used for the transition rates in these calculations. Since Pomplun's calculation method dynamically calculates the binding energies, it may result in a more accurate estimation of the Auger electron energies. It should be noted that the binding energies of the outer orbitals involved in Coster-Kronig transitions may be quite different when the Auger emitter is bound to a large molecular structure in a biological system. Hence, this method may not offer any overall increase in the accuracy of dose calculations.
- The third major assumption concerns the issue of charge neutralization in the condensed phase. Again, with the exception of Pomplun *et al*., all calculations of this type have assumed that vacancies created in the valence shell are immediately filled by electrons from the continuum (fast neutralization). Not making this assumption sharply reduces the calculated number of Auger electrons emitted, and results in a residual ionization potential on the atom, the energy of which must be locally deposited over some unknown spatial dimensions.

Pomplun *et al*. (1992) revised the original ^{125}I calculations of Charlton and Booz (1981). They pointed out that although the original average radiation spectrum was sufficient; energy conservation was significantly violated for some individual ^{125}I decays in the original MC code. Pomplun *et al*. (1992) used the quantum mechanical computer code of Desclaux to obtain binding energies for atoms with multiple inner shell vacancy configurations. This approach results in an exact energy balance between the nuclear transition energy and the total energy carried by the emitted electrons, photons and potential energy of the atom. Using this approach, the number and energy distribution of Auger electrons emitted by ^{123}I decay were calculated. The upper limit of electrons produced per ^{123}I decay was found to be 6.4 (one cascade only in 84% of the decays and also no neutralization during the decay). While the Auger electron spectrum of ^{123}I and ^{125}I are identical, the total frequency of Auger electrons and energy deposited by ^{125}I is about twice that of ^{123}I [55]. In 2012 Pomplun *et al.*

revised their ^{123}I spectrum by validating their existing MC program to photon-induced Auger cascades in noble gasses and not relying on pre-calculated electron energy values [56]. In this study it was found that between 1 and 25 electrons were emitted per ^{123}I decay with an average of 6.4 Auger electrons per decay. They speculated that 2.4 electrons per decay originate from the N shells, and when added to the ICRP value will result in a good agreement of their overall mean spectra of emitted particles.

Emission data used by Geant4 v9.6.0

The low energy processes include the photo-electric effect, Compton scattering, Rayleigh scattering, gamma conversion, bremsstrahlung and ionization [11]. X-ray fluorescence and Auger electron emission by excited atoms are also considered. All processes involve two distinct phases: the calculation and use of total cross sections, and the generation of the final state. Both phases are based on the theoretical models and on utilization of evaluated data. The data used for the determination of cross-sections and for sampling of the final state are extracted from a set of publicly available evaluated data libraries: the Evaluated Photons Data Library (EPDL97), the Evaluated Electrons Data Library (EEDL), the Evaluated Atomic Data Library (EADL), and the binding energy values based on data of Scofield. These libraries provide the following data relevant for the simulation of Geant4 low energy processes:

- total cross-sections for photoelectric effect, Compton scattering, Rayleigh scattering, pair production and bremsstrahlung;
- subshell integrated cross sections for photo-electric effect and ionization;
- energy spectra of the secondaries for electron processes;
- scattering functions for the Compton effect;
- binding energies for electrons for all subshells;
- transition probabilities between subshells for fluorescence and the Auger effect.

Geant4 uses the Livermore Evaluated Atomic Data Library (EADL), which contains data to describe the relaxation of atoms back to neutrality after they are ionised. Electron capture from the atomic K, L and M shells is simulated by producing a recoil nucleus of (Z − 1, A) and an electron-neutrino back-to-back in the centre of mass. Since this leaves a vacancy in the electron orbitals, the atomic relaxation mode (`G4AtomicRelaxation`) is triggered in order to produce the resulting x-rays and Auger electrons. In the electron capture decay mode, internal conversion is also enabled so that atomic electrons may be ejected when interacting with the nucleus. An important competitive channel to gamma emission is internal conversion. To take this into account, the photon evaporation database (used by the

`G4PhotoEvaporation` class) was extended to include internal conversion coefficients. The calculation of the Internal Conversion Coefficients (ICCs) is done by a cubic spline interpolation of tabulated data for the corresponding transition energy. These ICC tables, which were labelled Band ($1 \leq Z \leq 80$) and Rösel ($81 \leq Z \leq 98$), are widely used and were provided in electronic format by staff at Livermore Brookhaven National Library. The reliability of these tabulated data has been reviewed (comparable within a 10% uncertainty) [11].

2.3.2. Calculations and Computer modelling

The following studies involved computer calculations regarding dose estimations due to Auger emitting radionuclides.

Humm *et al*. presented a third report for the AAPM in 1994 [57]. The report reviews the dosimetry of Auger emitters at the molecular, cellular, and organ levels, and discusses the merits and shortcomings of each approach with respect to their capacity to predict biological effect. The electron range-energy relationship for unit density matter by Cole (1969) is given; Sastry and Howell frequently use this method to obtain absorbed doses to various target volumes containing electron emitting sources. Also described is Berger's (1973) dimensionless dose-point kernel which is valid for electrons down to 500 eV; and Booz *et al*.'s (1983) extrapolation of Berger's data. Using this method, the energy absorbed in a 10 μm diameter sphere of unit density water is 5.1 keV per ^{123}I decay using Howell's AAPM spectra and 5.2 keV per ^{123}I decay using Humm's (1989) spectra. Monte Carlo electron track codes by Paretzke (1987), Terrisol *et al*. (1978), Zaider *et al*. (1983), and Wright *et al*. (1990) are mentioned. Goddu *et al.* (1994, [58]) used Cole's approach and provided absorbed dose per unit cumulative activity values for Auger emitting radionuclides. For a unit density sphere with diameter of 8 μm, the energy deposited is 4.9 keV per ^{123}I decay.

Bousis *et al*. (2012) used an in-house MC code to perform transport calculations of electrons from internalized ^{123}I, ^{125}I, and ^{131}I [14]. All electrons were followed down to 13.6 eV. For energies < 10 keV, inelastic cross sections are calculated semi-empirically from the Born and Bethe theories (Inokuti, 1971) [59]. Elastic cross sections are obtained from the screened Rutherford formula replaced at low energies by the Brenner-Zaider parameterization (Brenner and Zaider, 1983). For a more detailed discussion of the MC code and the models used, see Bousis *et al*. (2012) [60]. Results were averaged over 10^6 decays. The Auger emission spectrum of ^{123}I was taken from the AAPM Nuclear Medicine Task Group Report by Howell (1992). They simulated a Raji cell with cell radius of 7.70 μm and unit density; often used to model a typical lymphoma B-cell (Griffiths *et al*., 1999). The nucleus had a radius of 5.775 μm ($0.75 \times r_{cell}$). The emission of photons with energies 3 – 4 keV and 27 – 30 keV were ignored since it was found that they contribute less than 1% to the total dose at the spatial scale. Other simulations included lymphocytes having a cell radius of 5 μm and a nuclear

radius of 4 μm. In these simulations they found the energy deposited in the cell was 5.4 keV per ^{123}I decay when distributed in the entire cell [14].

Raisali *et al*. (2013) used the G4EMLOW physics list of the Geant4-DNA extension in calculations of DNA single- and double-strand breaks due to the decay of ^{123}I and ^{125}I. Two different simple geometries of a 41 base pair of B-DNA made of unit density water were simulated and used as scoring volumes. The spectrum of ^{123}I Auger electrons given by Pomplun (1992) was used with an average of 6.4 electrons per decay. They found that for ^{123}I Auger electrons the average number of double-strand breaks due to direct hits is approximately twice the number of double-strand breaks due to indirect hits [15].

Freudenberg *et al*. (2011) used the low energy package in Geant4 for dose quantification and for the assessment and comparison of the biological effectiveness for different radiation qualities. The biological experiments involved the exposure of the rat thyroid cell line PC-C13 to radionuclide solutions which contained ^{131}I, ^{188}Re, ^{90}Y or ^{99m}Tc. For self-dose, a unit density water sphere with 12 μm diameter was used as the sensitive dose-scoring volume; no distinction was made between the cytoplasm and the nucleus. Decay sites were randomly sampled from a homogeneous distribution inside the entire volume. The irradiation period was chosen to be 1 h for all experiments and calculations. Self-dose for ^{131}I was found to be 0.46 mGy/Bq·s. They found that the self-dose increases as the energy of the emitted particle decreases. This behaviour is related to the stopping power of electrons that increases as the particle energy decreases. Strongly pronounced is the self-dose for ^{99m}Tc that emits low energy Auger- and IC-electrons. On the one hand it has an increased stopping power compared to beta emitters; on the other hand these electrons have very short ranges. Hence, the irradiation due to neighbouring cells is minor for ^{99m}Tc and other low energy electron emitting radionuclides. They noted that many authors use analytical expressions like dose point kernels or stopping power expressions for dose estimation, yet Monte Carlo simulations offer higher flexibility and comfort if the correct simulations of the physical interactions are done. The group's results compared well to similar calculations by Stabin and Konijnenberg (using the EGS4 code) and MCNP simulations [5].

Ivanchenko *et al*. (2012) presented a review article of the low energy models used in the Geant4 toolkit [42]. "Standard" models are selected by default in Geant4 and are based on analytical computations, whereas the "low energy" models are based on evaluated data libraries (EPDL97 or "Livermore" models) or on re-engineering of the 2001 version of the Penelope Monte Carlo code. This article focuses on physics models with regards to photons. The group shows that the use of the "low energy" sub-package is necessary to simulate dose depositions due to secondary electrons produced from the ~980 eV photoelectrons originating from the oxygen L-shell. Such photoelectrons can travel distances larger than the chromatin filaments (30 nm) and should be tracked for the modelling of DNA damage.

Francis *et al*. (2011) presented stopping powers and ranges of electrons, protons and alpha particles in liquid water using the Geant4-DNA extension. Results converge for highly energetic particles, but differences are observed for low energies when the applied theoretical models begin to diverge from each other. The results however show good agreement between the analytical calculations obtained from the Geant4-DNA simulations and data published in the ICRU reports. It was shown that electrons with energies < 1 keV have ranges < 100 nm. It was recommended that Geant4-DNA processes for energies above 1 eV for electrons, 1 keV for protons and 10 keV alpha particles should undergo further validation [43], [46].

Warters and Hofer (1977) studied radiation-induced mitotic delay due to ^{125}I incorporated into CHO cells. In the study, the cumulative dose from ^{125}I uniformly distributed in the nucleus to various subcellular regions was calculated using a computer code developed by Hofer *et al*. (1975). It was assumed the CHO cells were spheres of radius 6.4 μm, the nuclei spheres of radius 3.9 μm and that the cellular membrane was 9 nm thick. It was found that the absorbed dose to the cell was approximately 8.1 mGy per ^{125}I decay [22]. This corresponds to an energy deposition of 55.59 keV per ^{125}I decay.

Nikjoo *et al*. (2008) presented a paper providing a brief review of the physics of Auger electrons and discusses questions such as which type of interactions can occur following the decay of an Auger emitter and how the electron vacancies are generated [41]. A list of important sources of electron data available in various databases around the world was presented. The paper provides, for the first time, the initial vacancy distribution for the ^{124}I radionuclide using an in-house MC code with the known models for sub-eV interactions. Similar to the other radioiodines, the highest absorbed energy for electrons (300 eV) was 20 – 25 eV in water with ranges < 20 nm. Larger ranges were found for higher energy electrons but with lower absorbed energies.

Stepanek *et al*. (1996) presented a paper which documents the calculation of radiation spectra and of radial dose distributions around a point source for 24 radionuclides [1]: nuclides potentially useful for therapy by emission of Auger electrons - ^{51}Cr, ^{64}Cu, ^{67}Ga, ^{73}Se, ^{75}Se, , ^{77}Br, ^{80m}Br, ^{94}Tc, ^{99m}Tc, ^{114m}In, ^{115m}In, ^{123}I, ^{124}I, ^{125}I, ^{167}Tm, ^{193m}Pt, and ^{195m}Pt; nuclides potentially useful for therapy by α- particles with additional emission of Auger electrons – ^{212}Bi, ^{211}At, and ^{255}Fm; and nuclides potentially useful for electron Auger-therapy with simultaneous PET diagnosis – ^{73}Se, ^{94}Tc, and ^{124}I. Calculations of the emission spectra were calculated using the computer program IMRDEC which reads the decay schemes from the ENSDF. The atomic data as well as the atomic relaxation probabilities are obtained reading the EADL. The radial dose distributions were calculated using the IMR version of the MC code GEANT (1993). The calculations were performed in a soft tissue sphere of 10 nm

radius assuming that the radionuclide is placed in the centre. The average dose for ^{123}I was found to be 2.05 mGy-hour/decay.

2.3.3. Biological experiments

Kassis *et al*. studied the implications of ^{123}I incorporated into the DNA of V79 cells [3]. They assumed a cell diameter of 10 μm and a nuclear mass of 2.7×10^{-10} g of unit density, corresponding to a nuclear radius of 4 μm [61]. An average of 11 Auger electrons per decay for ^{123}I was assumed based on spectra by Sastry & Rao (1984), Charlton & Booz (1981), and Feinendegen (1975). They calculated the average energy deposited in the nucleus per ^{123}I decay in the nucleus to be 4.9 keV due to γ's and electrons based on the range-energy relationship by Cole (1969) [62]. At a 37% survival level, a total dose to the nucleus of 0.79 ± 0.09 Gy was obtained for ^{123}IUdR, corresponding to 277 ± 29 nuclear decays. The contribution of extracellular and cytoplasmic ^{123}I decays to the radiation dose to the nucleus was found to be negligible. They concluded that since the emitted Auger electrons have ranges of only a few nanometers in tissue, the sensitive sites in the nucleus correspond to intracellular volumes with diameters in the region of 3 – 5 nm. In spite of the different average number of Auger electrons emitted per decay, the three Auger emitters ^{77}Br, ^{123}I, and ^{125}I studied (if incorporated into the DNA) yield essentially the same RBE value of ~7 for cell killing when compared to 250 kVp X-rays, in accordance with results from a similar study done by Makrigiorgos *et al*. (1989) [3], [63], [64]. They found that the mean lethal dose (D_{37}) to the nucleus is the same for all three the nuclides. In other studies with V79 cells, Kassis *et al*. found an RBE of 4.5 for 3-acetamido-5-[^{125}I]-iodoproflavine ($A^{125}IP$) when compared to 250 kVp X-rays. The $A^{125}IP$ molecule is not covalently bound to DNA, but is still incorporated into the nucleus of the cell. They assumed that the V79 cell nucleus absorbed 29.2 keV per ^{125}I decay [65]. Makrigiorgos *et al*. calculated that the energy deposited in the nucleus per ^{123}I decay in the cytoplasm equals 0.33 keV, assuming the diameters of the nucleus and the cell are 8.00 μm and 10.3 μm [64].

Slabbert *et al.* performed a cytokinesis-block micronucleus assay on human lymphocytes and CHO cells exposed to 4-[^{123}I]-iodoantipyrine [13]. The antipyrine carries the ^{123}I across the cell and nuclear membrane to permit the deposition of Auger electrons close to cellular DNA. The same cell lines were exposed to [^{123}I]NaI or ^{123}I-HSA (human serum albumin). These molecules do not cross the cell membrane and the decay of the radionuclide only serves as an extracellular source of 159 keV low-LET γ-radiations. It was found that the iodoantipyrine was 3.7 times more effective than the HSA in producing a biological response in the lymphocytes and only 1.6 times more effective in the CHO cells. They concluded that damage from extracellular decays is probably due to the emitted γ's and damage from intranuclear decays is due to the low energy electrons, similarly found by Kassis *et al*. (1992).

Warters and Hofer (1977) studied radiation-induced mitotic delay due to ^{125}I incorporated into CHO cells by ^{125}IUdR [22]. The cell number and ^{125}I content per cell in each sample were determined immediately after the labelling and wash procedures, and various times thereafter by counting the labelled CHO cells in a Coulter particle counter and using a well-type crystal-scintillation counter. Aliquots of the labelled cell suspensions were retained to permit autoradiographic evaluation of the labelling index; which was found to be around 98% for all sample groups. The calculated energy deposition of 55.59 keV per ^{125}I decay per cell was used to perform dosimetry calculations in order to compare the ^{125}I induced cell division delay to that of 250 kVp external X-rays.

Howell and Bishayee (2002) investigated the biological effects of non-uniform distributions of DNA-incorporated ^{125}I (IUdR) in the Chinese hamster V79 cell line. They maintained the cells at 10.5°C for 72h to allow the accumulation of radiation damage in the absence of cell division. After washing, aliquots of cell suspension were taken to determine the mean radioactivity per cell using a 3" NaI well crystal (overall counting efficiency of 0.53 for the 35.5 keV characteristic γ-ray). They assumed the mean diameter of a V79 cell was 10 μm and its nucleus 8 μm based on work by Howell *et al*. (1991, [66]). They used the dosimetry model of Goddu *et al*. (1994) and the ^{125}I radiation spectrum by Howell (1992) [67], [4]. Using this model they calculated D_{37}[6] (^{125}IdU) to be 1.15 Gy and found a corresponding RBE of 12 when compared to ^{137}Cs gamma rays [68].

Howell *et al*. (1993), using spermatogenesis in mouse testis, showed that the lethality of ^{125}I is linearly dependent on the fraction of the radioactivity in the organ that is bound to DNA. They found that ^{125}IUdR produces an RBE of 7.9 in these cells when compared to external 120 kVp X-rays or internal irradiation with the γ-ray emitter ^{7}Be [69]. They theorised that by removing the absorbed dose contributions of the low LET radiation constituents, an RBE value of 13 could be obtained solely for the Auger electrons. They assumed a dose absorbed of 0.30 Gy/MBq obtained from previous work by Rao *et al*. (1990, [70]) in their calculations.

Miyazaki and Fujiwara (1981) described the mutagenic and lethal effects of ^{125}IUdR incorporated into the DNA of V79 Chinese hamster cells [71]. These effects were compared to effects on cells of 170 kVp external X-rays exposed in a frozen or room temperature state. The cells had a 14 hour labelling time for the ^{125}IUdR, after which the cells were washed to remove unincorporated ^{125}IUdR and plated at a final density of 5-10 × 10^5 cells/ml. It was found that 85-90% of the cells were labelled with ^{125}IUdR, revealed by CsCl equilibrium centrifugation analysis. The determination of incorporated activity in each sample was done using a γ-scintillation spectrometer. The activity-dose conversion was done using a value of 1.3 cGy / ^{125}I decay per single V79 cell nucleus. Finally, RBE values for ^{125}I decays in DNA were found to be ~11 for the 6TG^r mutagenesis and ~10 for cell inactivation.

[6] The dose required to produce a 37% survival in the cell population.

In the work by Narra *et al*. (1992), the spermhead survival in mouse testis was used to investigate the radiotoxicity for ^{123}IMP (N-isopropyl-p-iodoamphetamine), ^{131}IUdR (iododeoxyuridine), and ^{125}IdC (iododeoxycytidine) [72]. The cellular activity is localized in the cytoplasm for ^{123}IMP, and in the DNA of the cell nucleus for ^{131}IUdR and ^{125}IdC. The biological clearance from the testes was determined by measuring the radioactivity contained within each testis using a NaI well counter. The subcellular activity distribution was done in the following way: the testicular cells were isolated and the cytoplasmic and nuclear fractions were separated. Aliquots of these fractions were counted for radioactivity and the fraction of total cellular activity found in the two compartments was obtained. The nuclei were further processed to obtain the fraction of nuclear activity bound to DNA. The absorbed dose to the testis was calculated using conventional MIRD techniques; the values if the mean energy emitted per transition for the radionuclides were taken from Weber *et al*. (1989). Assuming a uniform distribution of the radiochemical in the testis, the absorbed dose per unit cumulated activity was calculated. In this work, compared to the D_{37} of 120 kVp external X-rays, the RBE value of ^{125}IdC was found to be 8.7 ± 1.4, and the RBE values of ^{123}IMP and ^{131}IUdR are essentially equal to 1.

In a similar study, Rao *et al*. (1989) found the RBE of ^{125}IUdR in mouse testis to be 7.9 ± 2.4 when compared to 120 kVp external X-rays [73]. It was found that 98% of the injected activity of ^{125}IUdR was quickly eliminated from the testis; the biological half-life being 0.18 hours. The remainder was cleared with a long half-life of 308 hours. To determine the macroscopic radionuclide distribution in the testes, several testes were removed, frozen and sliced into ten sections. Each slice was weighed and the activity it contained assayed. The radioactivity per gram of tissue was essentially the same in all sections, indicating a fairly uniform distribution of radioactive material. In the calculations it was assumed a single ^{125}I decay in the nucleus of a spermatogonial cell (9 μm cell diameter, 5 μm nucleus diameter) deposits 10.5 keV in the radiosensitive cell nucleus.

Yasui *et al*. (2001) investigated delivering a cytotoxic dose of radiation (from ^{125}IUdR) to the cell nucleus of the estrogen-receptors expressing human breast cancer cell line, MCF-7 [74]. After the incubation incorporation period, the cells were collected by trypsinization, washed, and an aliquot of a known number of cells was counted in a well-type γ-ray counter to determine the incorporated activity. The cellular uptake of the activity was estimated using ^{125}IVME2 (E-17α[^{125}I]-iodovinyl-11βmethoxyestradiol) and a nonradioactive 17β-estradiol competitor. To calculate the RBE, the ^{125}IUdR decays per cell were converted to centigrays as 0.742 cGy / ^{125}I decay. The RBE for survival of the MCF-7 cells exposed to ^{125}IUdR decays relative to a 1 Gy ^{137}Cs γ-ray exposure was calculated to be 4.5.

2.3.4. Summary

Track structure simulation codes remain the only tools able to reproduce in detail energy deposits in small biological structures, such as the cell nucleus or the DNA molecule and its surroundings [43], [75].

In more or less all computer simulations of real processes, there are many restrictions and uncertainties due to limited available input data, such as the transition rates, the influence of molecular versus atomic structure, and the velocity of charge neutralization [56].

For Auger emitters bound to DNA, high RBE values have been reported and a radiation weighting factor[7] w_R of 20 (similar to that of α-particles, fast neutrons, fission fragments and heavy ions) or more have been proposed [35], [36], [69]. For those Auger electron emitters that enter the cell but are not bound to DNA, RBE values between 1.5 and 8 (an average ~4) have been found for different endpoints in cell studies [61], [76].

Given in Table 2.2 are numbers of Auger and Coster-Kronig electrons and Internal Conversion electrons emitted per decay of ^{123}I, and in Table 2.3 the total energy available for these electrons per ^{123}I decay, as determined by the various authors discussed above.

The biological effects of Auger emitters have been extensively studied in a variety of *in vitro* and *in vivo* experiments [8], [77]. *In vivo*, rodent spermatogenesis has been utilized as a model system to evaluate the cytotoxicity of a range of Auger emitters including ^{55}Fe, ^{99m}Tc, ^{111}In, ^{114m}In, ^{123}I, ^{125}I, and ^{210}Tl. *In vitro*, the cytotoxic effects of ^{35}S, ^{75}Se, ^{51}Cr, ^{67}Ga, ^{77}Br, and a range of compounds labeled with ^{123}I and ^{125}I, have been studied in a variety of human and rodent cell lines and model culture systems [1], [36]. Representative of various results reported are an increase of biological effectiveness by a factor of 7–12 for ^{125}I when the radionuclide is incorporated into DNA following administration as ^{125}IUdR, RBE values of around 4 for ^{125}I localized in the nucleus, but not directly bound to DNA, and RBE values of around 1 when ^{125}I is localized in the cytoplasm [69], [65], [70], [22], [8].

[7] Used to calculate the equivalent dose, which represents the stochastic effects of ionizing radiation.

Table 2.2. Electron frequency data with regards to ^{123}I.

Auger & Coster-Kronig per decay	*IC per decay*	*Auger & CK Energies (keV)*	*Reference*
2.9	0.15	0.699 – 30.1	ICRP (1983)[1] [51]
8.9			Humm (1984)[2,3]
13.2		Avg: 19.3	Charlton & Booz (1981) [52]
11			Sastry & Rao (1984), Kassis (1990) [3]
14.9	0.15	0.0298 – 30.2	Howell (1992)[2,3] [4] / AAPM
6.4	0.15	0.0285 – 30.3	Pomplun (1992,2012)[2] [55] [56]

[1]No transition with N or higher shells; [2]Neutralization of all vacancies during metastable states; [3]Instantaneous neutralization of valence shell vacancies during cascades

Table 2.3. Available electron energy from the decay of ^{123}I.

	Energy (keV/decay)		
Reference	*IC*	*Auger + CK*	*Total*
ICRP [51]	20.074	7.484	27.558
Howell / AAPM [4]	20.104	7.545	27.649
Pomplun [55]	19.491	6.482	25.973

Chapter 3: Experimental Procedures

3.1. Radiobiology

In this study, the cytokinesis blocked micronucleus assay was used to analyze the effects of γ-radiation from a ^{60}Co-source on rat brain endothelial (bEND5), Chinese hamster ovary (CHO-K1) cells, and isolated and stimulated human lymphocytes. Linear-quadratic dose-response curves were then determined for these cell lines. This assay was also used to determine the biological response of human lymphocytes from two individual donors exposed to DNA incorporated ^{123}I.

The relevant ^{60}Co linear-quadratic equation was then used as reference curve to determine the relative biological effectiveness of the Auger electron emitting ^{123}I.

The REC ethics reference clearance number is S12/04/091 obtained from Stellenbosch University to undertake research experiments with biological samples and radioactive substances under the supervision of Prof. J P Slabbert and Mr. P Beukes of iThemba LABS.

3.1.1. Calibration of the ^{60}Co-teletherapy unit

As with any commercial or therapy units which are in use, the ^{60}Co-unit (Eldorado 76, Atomic Energy of Canada Ltd.) at iThemba LABS needs to undergo annual quality assessments. The main objective is to determine the dose rate and shutter correction time of the unit; as well as the current activity of the radioactive source.

^{60}Co undergoes β^--decay to an excited state of ^{60}Ni which promptly de-excites to a stable state by mainly emitting two γ-rays with energies 1.173 MeV and 1.332 MeV. This isotope has a half-life of 5.27 years (and hence a decay constant of 3.60×10^{-4} days^{-1}) [24].

According to the certificate of measurement, the unit had an activity of 292.3 TBq measured on 10 August 1999.

The activity $A(t)$ of a source, at a time t, can be determined using the exponential decay law

$$A(t) = A_0 e^{-\lambda t} \tag{3.1}$$

from the initial activity A_0.

Theoretically, the exposure rate (in R/h) due to a source with activity A (Bq), at a distance r (cm), with photon energies E_i (MeV), yields y_i and mass energy absorption coefficients μ_{en}/ρ (cm/g) for air, can be calculated from [78]:

$$\dot{X} = (5.263 \times 10^{-6}) \frac{A}{r^2} \sum_i y_i E_i \left(\frac{\mu_{en}}{\rho}\right)_i \tag{3.2}$$

A very convenient resource is the Rad Pro Calculator [79]. It incorporates on-line databases of photon energies, their yields and mass energy absorption coefficients of various materials and elements. Using this application, the exposure rate of a gamma emitting radionuclide can easily be calculated according to equation (3.2). The exposure rate (R/h) in air can be converted into an absorbed dose rate in air (Gy/h) by multiplying by a quality factor of 0.00877 [80].

The IAEA recommends the use of a cylindrical ionization chamber (volume 0.1 – 1 cc) for the calibration of ^{60}Co gamma ray beams and provides protocols based on absorbed dose to water calibration coefficients [81]. The absorbed dose to air $D_{Co,air}$ in the air cavity can be converted into absorbed dose to water $D_{Co,w}$ by making use of the Bragg-Gray cavity relationship [18]. With a known calibration coefficient $N_{Co,w}$ for the specific chamber (determined for a ^{60}Co beam quality at a standards laboratory), the fully corrected chamber signal M_{Co} allows the determination of the absorbed dose to water as follows:

$$D_{Co,w} = M_{Co} N_{Co,w} \tag{3.3}$$

Absorbed dose measurements were done on the ^{60}Co-teletherapy unit at iThemba LABS on 5 June 2013. A 0.66 cc cylindrical Farmer ionization chamber, along with a Farmer 2570 Dosimeter (electrometer), was used to obtain the measured values. The absorbed dose, in gray (Gy), can then be obtained by multiplying the measured value M_{Co}, in radiation units (RU), corrected for ambient air temperature and pressure, with the calibration factor $N_{Co,w}$. The dosimetry system which was used has a calibration factor $N_{Co,w}$ of 0.7610 Gy/RU.

The irradiation setup consisted of a field size of 30 × 30 cm^2 and a source-to-surface distance (SSD) of 75.6 cm. A 6 mm thick Perspex sheet was placed at 75 cm to act as build-up material and ensure electronic equilibrium. A 4.9 cm thick slab of Perspex was placed 3.5 cm from the build-up material to aid in dose deposition due to backscatter (Figure 3.1). The ionization chamber was placed on top of the build-up sheet at the center of the square field.

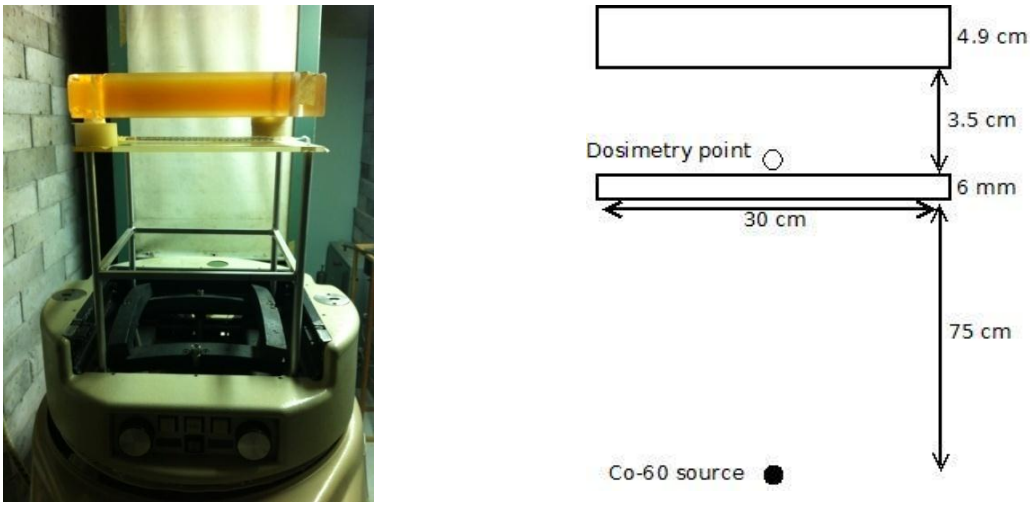

Figure 3.1. The ^{60}Co teletherapy unit (left) and the schematic of the experimental setup (right).

Firstly, the temperature and air pressure were recorded, since the ionization chamber is open to ambient air and therefore subject to atmospheric variations. These were input into the dosimeter to automatically adjust the measurements.

Secondly, determination of the shutter correction time was done by measuring the absorbed dose (in RU) for exposure times with increments of 0.1 min. This measurement was performed for exposure times of 0.1 – 0.9 minutes and 1.5 minutes. Plotting the exposure time as a function of measured dose (in Gy, once multiplied by the calibration factor) results in a linear relationship with the reciprocal of the slope giving the dose rate of the unit (in Gy/min) and the intercept giving the shutter correction time (in min).

Thirdly, an absorbed dose (in RU) was then measured for an exposure time of 1.0 min using the ^{60}Co-unit. This measurement was repeated 5 times. Multiplying each value with the calibration factor gives the dose rate (in Gy/min). The average value can be compared to the reciprocal slope of the exposure time-dose curve.

3.1.2. Cell preparation and irradiation

It is important to perform all work, with regards to the transportation or addition of chemicals to the cells, in a sterilized environment. All of the experimental work, except perhaps for the fixation and arresting of the cells, should be done inside a laminar flow cabinet, under sterile conditions and wearing latex gloves and lab coats.

The culturing, harvesting and micronucleus assay of the bEND5 and CHO cells are similar. The following reagents are required during the micronucleus assay for these cells in the G2/S phases:

- Cytochalasin B (5 mg / 3.3 ml dimethylsulfoxide)
- RPMI 1660, cell culture medium
- Trypsin
- Hypotonic solution KCl (75 mM, 5.6 g for 1 litre, kept at 4°C)
- Ringer solution (9 g NaCl + 0.42 g KCl + 0.24 g $CaCl_2$ for 1 litre)
- Methanol / Acetic acid / Ringer solution (with ratio 4 / 1 / 5, kept at 4°C)
- Methanol / Acetic acid (with ratio 4 / 1, kept at 4°C)

The bEND5 cells were allowed to grow to confluence; incubated at 37°C in a humidified atmosphere of CO_2. On the day of irradiation, the cells were trypsinized from the culture flasks. A haemocytometer was used to obtain a cell count of approximately 3×10^5 cells/ml. Cell culture medium was added to the cell mixture as needed in order to obtain the required concentration. Tubes were labeled according to the planned exposure values (namely 0 – 4 Gy in 0.5 Gy increments, hence 9 dose values). Into each of these tubes, 1 ml of the

concentrated cell mixture and 4 ml of the medium was added. The tubes were then individually irradiated using the ^{60}Co teletherapy unit.

After the irradiation, the contents of each tube were divided into 2 wells of a 6-well plate. Hence 2.5 ml of irradiated cell mixture per cell culminating in 18 separate samples. Noting the time, 3.8 µl of Cytochalasin B was added to each well to block cytokinesis. The cells were then stored in an incubator at 37°C overnight (approximately 20 – 24 hours). Any storing time longer than 16 hours will result in the increased formation of multinucleated cells instead of just binucleated cells.

After incubation, any liquid and cells in suspension were transferred from their well to a correspondingly labeled test tube. The remaining cells, adhered to the surfaces of the well, were trypsinized into their respective test tubes using 2 ml of medium to deactivate the trypsin. The transportation of cells, from one vessel to another, needs to be done as carefully as possible, as it will determine the amount of cells available for plating onto slides. After this, the cells can be fixed and slides can be made.

In a similar procedure, the CHO-K1 cells were harvested after incubation by trypsinization. A cell count of approximately 1.5×10^5 cells/ml was obtained. Nine small Petri dishes (diameter of 35 mm) were labeled according to the exposed dose; each containing a (22 mm side length) glass cover slip. Into each of these dishes, 0.2 ml of CHO-K1 cells and medium were added, and then individually irradiated. Similarly, cyt-B was added after irradiation, and the cells were incubated for approximately 24 hours. Afterwards, the supernatants were removed, the seeded cells treated with a hypotonic solution of 75 mM KCl and fixed once with a 1/3 methanol/acetic acid solution for 5 min. Supernatants were then removed; the cover slips were allowed to air dry and then stored at room temperature until slide staining and micronucleus scoring.

The following reagents are required for the isolation and micronucleus assay of lymphocytes:

- Histopaque (polysucrose gradient with density 1.077 g/ml)
- Cytochalasin B (5 mg / 3.3 ml dimethylsulfoxide)
- Complete medium: 79% RPMI 1660 cell culture medium
  1% penicillin / streptomycin
  20% foetal bovine serum
- Phytohaemagglutinin (PHA-M)
- Phosphate buffered saline (PBS)
- Hypotonic solution KCl (75 mM, 5.6 g for 1 l, kept at 4°C)
- Ringer solution (9 g NaCl + 0.42 g KCl + 0.24 g $CaCl_2$ for 1 l)
- Methanol / Acetic acid / Ringer solution (with ratio 4 / 1 / 5, kept at 4°C)
- Methanol / Acetic acid (with ratio 4 / 1, kept at 4°C)

Whole blood was obtained from two male donors using Vac-U-Test tube with Lithium Heparin as anticoagulant. The tubes were centrifuged for 10 minutes at 180 relative centrifugal force (rcf) (~1000 rpm) and 24°C to separate the serum from the blood cells. After the serum floating on the cells has been removed (leaving a 5 mm layer on top of the cells, since this may contain some lymphocytes), 2 ml room temperature sterile PBS was mixed into each tube. The content of each Vac-U-Test tube was then carefully layered onto 3 ml Histopaque, prepared in 15 ml conical test tubes, being careful not to mix the two solutions (Figure 3.2). The conical tubes were then centrifuged for 30 min at 180 rcf, with slower acceleration and deceleration speeds. Following centrifugation, several layers of cells and serum are clearly visible. The erythrocytes collect at the bottom of the tube and a cloud of lymphocytes accumulate in the plasma-Histopaque interphase (Figure 3.3). The serum/PBS mixture was removed, leaving a 5 mm layer directly above the cloud of lymphocytes. The cloud of lymphocytes was collected and suspended in 10 ml PBS in new conical tubes. This lymphocyte/PBS mixture was the centrifuged for 10 min at 180 rcf to remove all serum factors. The supernatant was discarded and the lymphocyte pellet was suspended in 5 ml warm complete medium. At this point, the cell number per sample was kept constant by pooling the isolated lymphocytes from each donor, and determining the number of cells per ml in this cumulative sample using a haemocytometer. From this lymphocyte stock, cultures containing approximately 2.5×10^6 cells (± 8%) in 5 ml complete medium were made in 10 ml tissue culture tubes.

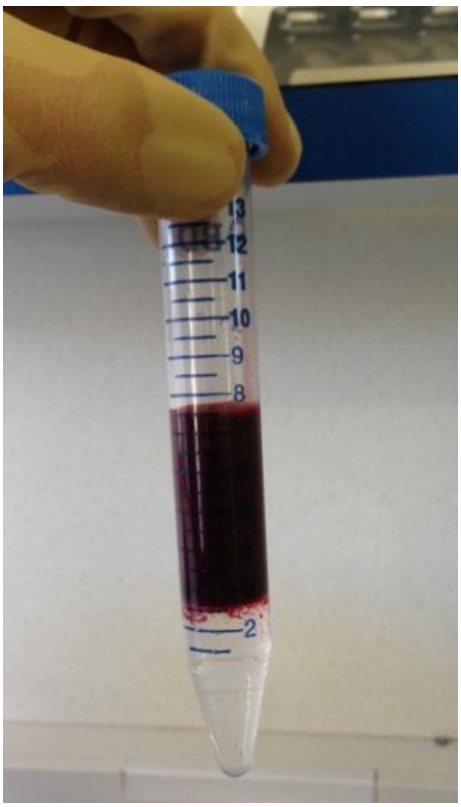

Figure 3.2. Whole blood on top of Histopaque.

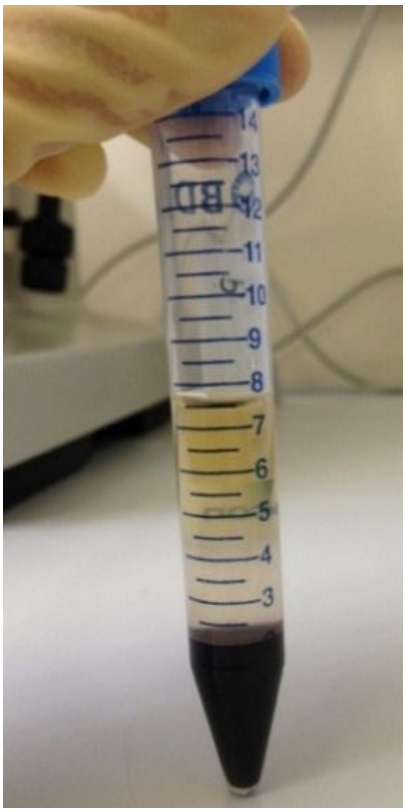

Figure 3.3. Serum, lymphocyte, Histopaque and erythrocyte layers.

At this point the lymphocyte cultures can be irradiated using the ^{60}Co-teletherapy unit to investigate micronuclei inductions by the ionizing γ-rays.

To each culture, 100 µl of PHA was added to stimulate and induce cell growth and division. The cultures were placed in an incubator (37°C, 5% CO_2 in air) at a 45° angle to increase the surface area and enhance gas exchange. The caps of the tubes should be loosened / unscrewed once in the incubator to allow gas exchange. After 44 hours of incubation, 10 µl of cyt-B was added to each culture to prevent cytokinesis and produce multi-nucleated cells. The cultures were then incubated for a further 28 hours, after which the cultures were stopped by hypotonic solution of KCl and fixed, followed by the slide preparation, staining and micronuclei scoring.

3.1.2.1. ^{60}Co irradiations

The samples were individually irradiated using a ^{60}Co teletherapy unit at iThemba LABS-NRF, Somerset West. The irradiation setup consisted of a field size of 30 × 30 cm^2 and a source-to-surface distance (SSD) of 75.6 cm. A 6 mm thick Perspex sheet was placed at 75 cm to act as build-up material and insure electronic equilibrium. A 4.9 cm thick slab of Perspex was placed 3.5 cm from the build-up material to aid in dose deposition due to backscatter (see Figure 3.1).

3.1.2.2. ^{123}I exposures

The thymidine analogue 5-[^{123}I]-iodo-2-deoxyuridine (^{123}IUdR) was prepared and used to incorporate ^{123}I into the DNA of human lymphocytes (see Appendix B). Certain volumes of ^{123}IUdR (corresponding to an activity concentration of ^{123}I) were added to the lymphocyte culture suspensions 44 hours post culture start-up. The cells were allowed 1 hour to incorporate the ^{123}IUdR after which the residual ^{123}IUdR was removed:

The lymphocytes were centrifuged for 10 min at 1000 rpm and room temperature. The ^{123}IUdR/complete medium mixture was removed (being careful not to disturb the cell pellet). The lymphocyte pellet was suspended in 1 ml warm complete medium and transferred to new tissue culture tubes.

A NaI-well counter was used to measure the number of disintegrations (counts) occurring over 60 seconds for every sample, ensuring the dead time was not more than 25%. This results in an estimation of the activity incorporated by the lymphocytes. The activity measurements took into account background counts and detector counting efficiency as will be described in Section 3.1.4. The lymphocytes were kept at room temperature for 24 hours to accumulate damage, after which warm 4 ml complete medium, 100 µl PHA and 10 µl cyt-B

was added to each culture tube. The tubes, with loosened caps, were placed in the incubator at a 45° angle for 28 hours.

3.1.3. Slide preparation and MN scoring

After a total culturing period of 72 hours the cell cultures were terminated. The termination of cell cultures and fixation steps were as follows: centrifuge the tubes for 8 min at 1000 rpm. Discard the supernatants using Pasteur pipettes, being careful not to discard the pellet of cells at the bottom of the tube. Slowly (while vortexing) add 7 ml cold KCl. This helps the cell regain its spherical structure and stop cell growth. Centrifuge the tubes for 8 min at 1000 rpm. Discard the supernatants as previously; a small cloud of cells should be visible. Slowly (while vortexing) add 5 ml of methanol/acetic acid/Ringer solution. This helps the cell keep its spherical/oblong structure. Store the tubes overnight at 4°C.

The tubes were centrifuged for 10 min at 1000 rpm on the day of slide preparation. The following fixation steps were repeated 3 times: Discard the supernatants. While vortexing, slowly add 5 ml of methanol/acetic acid to each tube. Centrifuge the tubes for 8 min at 1000 rpm. Forty µl of the fixed cells were dropped onto clean slides and air dried. The remaining cells in the tube can be kept in refrigerated storage [82].

Two methods were employed in the cell staining and micronucleus scoring: a manual and a semi-automated method.

In the manual method, a working solution of Acridine Orange stain was made by adding 0.5 ml Acridine Orange solution to 45 ml buffer solution (pH 6.8). The microscope slide was immersed in the working solution of Acridine Orange for 1 min. The slide was then rinsed with distilled water. Finally, the microscope slide was immersed in the buffer solution (pH 6.8) for 1 min to de-stain. A drop of buffer solution was placed on the slide and a cover slip was carefully mounted on top of it, avoiding any bubble formation. The edges of the cover slip were sealed with Cutex to prevent the drying of the slide. The MNi per BN cell were then counted by hand (up to 200 cells), using a ZEISS Axio Scope A1 and FITC filter. The Acridine Orange stain causes the cell nucleus to fluoresce a green/yellow colour while the cytoplasm emits an orange/red colour when stimulated with UV light (see Figure 3.4).

In the semi-automated method, under low light conditions a drop of DAPI Vectashield was added to each slide to stain the nuclei. The slides need to be dry with no condensation. The slides were then each covered with a cover slip and allowed to dry for approximately 10 min. The MSearch Module of the Metafer 4 automated imaging system was used to numerate the number of micronuclei in binucleated cells, after which the positive results were visually verified [33].

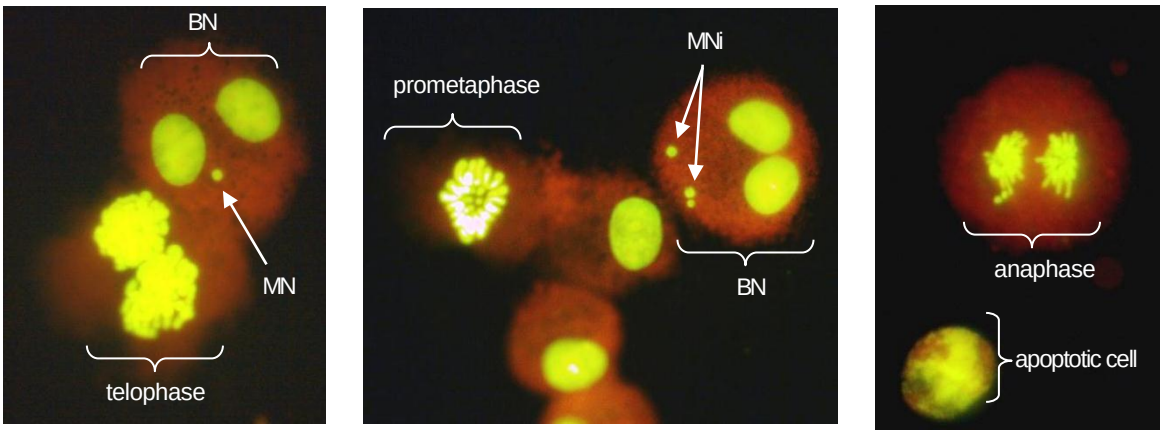

Figure 3.4. CHO-K1 stained with Acridine Orange. The cytoplasm emits an orange/red colour whereas the nuclei are a yellow / bright green colour. Pictured are some cells in varying phases of mitosis.

The resulting DNA damage due to the radiation was quantified by numerating the number of MNi per BN cell. To analyse the obtained results, the number of MNi per BN cell was normalized to 500 BN cells. This value was then plotted against the dose and a linear-quadratic curve was fitted to the data points (equation (2.2)).

3.1.4. The Radiobiology and Radionuclide Production detectors

The ^{123}I labeled deoxyuridine was obtained from the Radionuclide Production (RP) Department at iThemba LABS. A certain activity in a certain volume is produced (~1 mCi/ml). The activity was measured by the RP using a certified radioisotope (dose) calibrator. A typical dose calibrator consists of an ionization chamber (the detector), a high voltage power supply, a current-to-voltage amplifier / electrometer, and an electronic display unit through which it is possible to select the radioisotope to be calibrated. Dose calibrators use a well-type ionization chamber to measure the total amount of ionization produced by the radioactive sample. The ionization chamber contains a gas (usually Argon) under high pressure and has two electrodes with a voltage difference between them. When the tube or vial containing the radioisotope is placed in the chamber, the gas is ionized, the ion pairs move toward the anode and cathode, and an electrical current flows between them. This current is proportional to the activity of the isotope under investigation. A dose calibrator, like the one at RP, is used for assaying relatively large quantities (i.e. > 100 µCi) of γ-ray emitting radioactivity.

The Radiobiology (RB) Department at iThemba LABS uses a non-certified Canberra (model 802 series) NaI-well type scintillation detector with a photomultiplier tube to measure the activities in samples by means of a multi-channel analyzer (MCA) operated at 0.7 kV. The Silena EMCA 2000 software is used to collect and display the number of gamma ray emissions

as well as the energy of the gamma rays emitted by the radionuclide. This detector system is specifically designed to measure very low activities (i.e. < 1 μCi) of γ-ray emitting radioactivity.

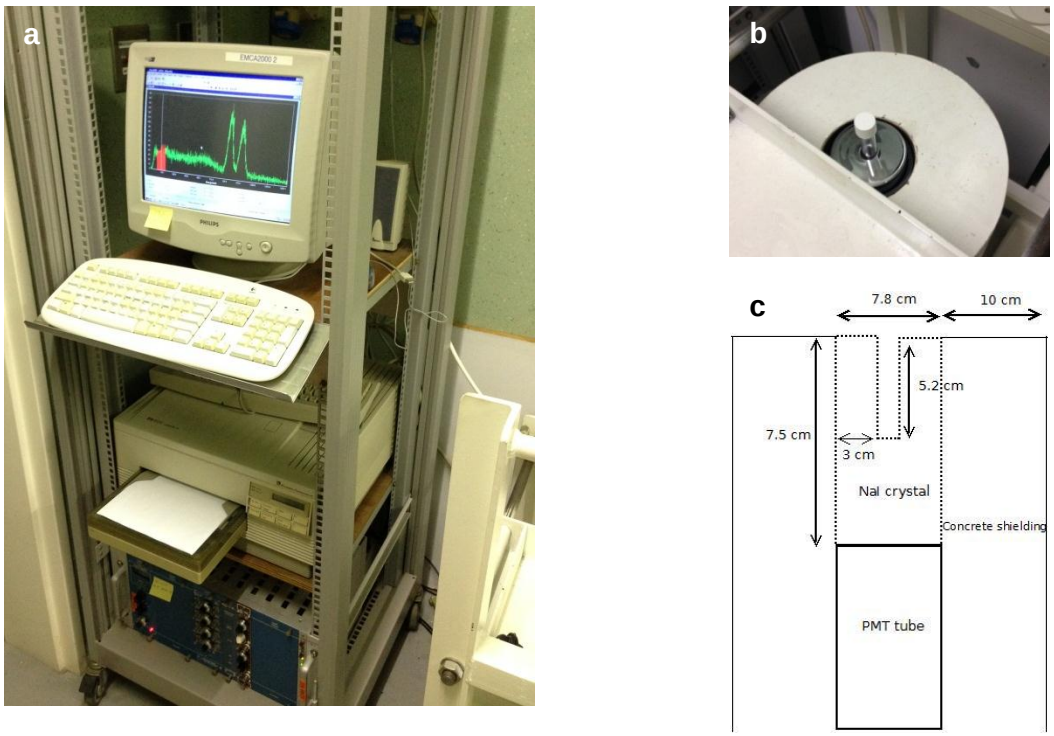

Figure 3.5. The experimental setup of the NaI well-counter. The electronics are shown in (a) with the NaI well detector next to the rack (b) and the schematics of the detector shown in (c).

The channel number-to-energy conversion of the RB detector was done using a certified calibration source (i.e. ^{60}Co). This involves measuring the spectrum of the source and finding a correlation between the channel number and the known energy of characteristics peaks (i.e. the 1173 keV and 1332 keV γ-rays).

Next, the linearity test involves determining if the detector readout is linear for sources varying from the kBq to MBq range. This was done by diluting various volumes of Na^{123}I in 1 ml water to obtain a series of samples with activities ranging from 10 nCi to 1 μCi of which the activities were measured using the RB detector.

Gamma radiations can pass through relatively large distances before an interaction takes place. Therefore, the detection efficiency is usually less than 100%. It is necessary to know the counting efficiency of the detector for γ-ray spectrometry of unknown activity in samples. To quantitatively determine the activity of a radionuclide in samples measured with a detector, the associated absolute full-energy peak (FEP) (also known as photopeak) efficiency is required. The absolute, full-energy peak efficiency can be defined as:

$$\varepsilon_{abs} = \frac{C_\gamma - \frac{T_\gamma}{T_b} C_b}{A\ V\ I_\gamma T_\gamma} \tag{3.4}$$

where ε_{abs} is the absolute full-energy peak detection efficiency (number of counts detected per number of γ-rays emitted by source), C_γ is obtained by subtracting the continuum counts under the peak from the gross counts, and C_b is the background counts. T_γ and T_b are sample live (measurement) time and background live time measurements, respectively. A is the number of nuclear decays per second (the activity concentration in Bq/ml) of standard source, V the volume of the sample and I_γ is the probability per nuclear decay for that specific γ-ray (the branching ratio).

The detection efficiency of the detector can be measured using a certified source of known activity. It is important to use calibration sources which have activities in the measurement range of your detector and which emit photons with energies similar to the ones you propose to detect.

In this study $Na^{123}I$ in NaOH with a known activity concentration (determined by RP) was used to perform the linearity test and calibration of the NaI-detector. A known activity of the $Na^{123}I$ was diluted to various concentrations in 1 ml. For ^{123}I, the photopeak under considering was the 159 keV γ-ray with I_γ = 0.8325 [24]. The disintegrations over 60 seconds from every sample were obtained using the RB detector. These values were then compared to their corresponding RP value to determine the absolute full-energy peak detection efficiency.

The composition of the 1 ml cell suspension which incorporated the ^{123}I we wish to measure with the RB detector is different (e.g. it contains C, O, H, K, etc.) to the $Na^{123}I$ diluted in NaOH we determine the efficiency from. We assume however that the difference in self-absorption of the 159 keV in the cell suspension is negligible when compared to the NaOH solution.

To determine the incorporated activity A (in Bq) in the cell samples, the net counts in the area of the 159 keV photopeak was used to determine the activity of the suspected radionuclide in the samples by using the following equation:

$$A = \frac{C_\gamma - \frac{T_\gamma}{T_b} C_b}{T_\gamma I_\gamma \varepsilon_{abs}} \tag{3.5}$$

where the symbols are the same as described above for equation (3.4).

3.1.5. S-phase fraction of lymphocytes using BrdU

During the S-phase of the cell cycle, thymidine analogues can be incorporated into the DNA strand. This can be used to determine the amount of cells which were in S-phase at a certain time and therefore could incorporate the ^{123}IUdR. Lymphocytes were isolated and stimulated as described in the previous sections. Approximately 44 hours post culture start-up, 50 µl of Bromodeoxyuridine (BrdU) was added to the tissue culture tube. The cells were placed in the

incubator for an additional 1 hour in order to incorporate the BrdU. After this, the content of the tube was transferred to a conical tube, the tube was centrifuged for 10 min at 1000 rpm and the supernatant was removed. The pellet was washed again using 5 ml complete medium in order to remove any remaining BrdU before the culture was terminated. After the supernatant was removed, the cells were fixed using cold KCl and Methanol / Acetic acid / Ringer's solution as previously described. The following day, the cells were washed using the Methanol / Acetic acid solution and microscope slides were prepared using 40 µl of the cell suspension. These slides were kept in the refrigerator until an anti-BrdU immunostaining procedure was performed.

The final slides were stained with DAPI and covered with a coverslip. Approximately 1000 mononucleated cells were counted using automated Metafer system and a DAPI filter. All of the identified cells were then re-evaluted by hand under an FITC filter to determine if BrdU is present. This indicates if the cell was in S-phase at the time of labelling or not.

The binucleation index of the lymphocyte from the same culture, as those which were labelled with the BrdU, was determined. The cells were stimulated as previously described, but at 44 hours post culture start-up, 10 µl of cyt-B was added; and the cells cultured for a further 28 hours before termination and fixation. The Metafer automated imaging system was used to count the number of mononucleated and binucleated cells within a defined area on the microscope slide.

3.1.6. Determination of cell sizes

The dependence of the dose absorbed on the size and geometry of the cell is clear from the definition of absorbed dose (see equation (3.6) later) and the knowledge of the range of charged particles (Section 2.3), particularly the low energy electrons produced in the decay of ^{123}I. For this reason, experimental measurements of the diameters of CHO cells and isolated and stimulated lymphocytes were made.

The cells were isolated and cultured as previously described. At 44 hours post culture start up, 50 µl of each cell suspension was placed on microscope slides and covered with a coverslip and viewed under a microscope. Calibrated software was used to measure the diameters of the cells, as can be seen in Figure 3.6.

The diameter of the nucleus was taken to be 80% of the total cell diameter to coincide with and compare to similar work done by Kassis *et al*. [3] and Bousis *et al*. [14]. The nuclear membrane (also called the nuclear envelope) was considered to be 40 nm thick and the cell membrane 7 nm thick [83], [84], [85].

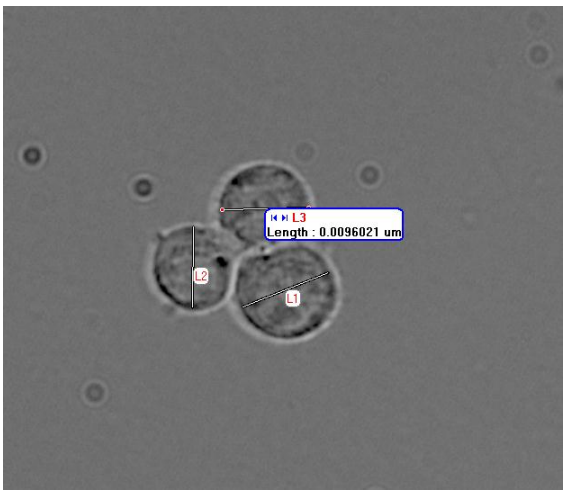

Figure 3.6. An example of the diameter measurements of lymphocytes in culture.

3.2. Monte Carlo simulations

The absorbed dose is a non-stochastic quantity applicable to both directly and indirectly ionizing radiations. For indirectly ionizing radiations, energy is imparted to matter in a two-step process: the indirectly ionizing radiation transfers energy as kinetic energy to secondary charged particles; these charged particles then transfer some of their kinetic energy to the material (resulting in dose absorbed) and also lose some of their energy in the form of radiative losses (bremsstrahlung, in-flight annihilation) [18].

The absorbed dose is related to the stochastic quantity “energy imparted”. The absorbed dose is defined as the mean energy imparted $\bar{E}$ by ionizing radiation to matter of mass *m* in a finite volume *V* by:

$$D = \frac{\bar{E}}{m} \tag{3.6}$$

The mass of a spherical shape can be obtained using the density and the volume, or the radius if it is known:

$$\begin{aligned} m &= \rho \times V \\ &= \rho \times \frac{4}{3}\pi r^3 \end{aligned} \tag{3.7}$$

The absorbed dose is therefore dependent on the type of ionizing radiation, the elemental make up, the density (and hence mass) and the volume of the geometry being considered.

In order to accurately represent the cell geometry, diameter measurements were done on lymphocytes and CHO cells.

The ^{60}Co simulated geometry was set up to replicate the experimental setup with regards to the source location and type, collimation, build-up and backscatter, the Petri dish and cellular media (densities, etc.). The energy and the dose deposited by the ^{60}Co source (γ-rays,

primary and secondary electrons) was then be quantified in the effective Petri dish volume by the Monte Carlo simulation. This basic simulation was done to determine the accuracy and reliability of Geant4 for the main objective regarding the simulation of energy depositions due to Auger electrons from the full decay of ^{123}I (incorporated into the anatomy of a cell).

Simulations were done to determine the energy deposition in the cell and nucleus, when the ^{123}I source is randomly (uniformly) distributed throughout the nucleus, the cytoplasm, the cell, one neighbor cell away, or in a 1 cc volume. Additionally, calculations using the Livermore Low Energy and the DNA physics lists were compared.

In all simulations, the `RanecuEngine` random number generator was used and the computer's clock used to set the initial seed [39].

3.2.1. ^{60}Co simulations

Geant4 was used to simulate the experimental setup and decay of a ^{60}Co-source and determine the energy deposition in a certain volume. From these simulations, an equation relating activity to dose rate was determined. The predicted dose rate was then compared to measured values.

Geant4.9.6 and Microsoft Visual C++ 2010 Express was used on a Windows 7, Intel Core2 Duo @ 2x2 GHz, 3 GB RAM platform to perform the Monte Carlo simulations.

3.2.1.1. Geometry and Physics

In a world geometry filled with air at standard temperature and pressure, a 6 mm thick Perspex build-up was placed at 75 cm from the source, and a 4.9 cm thick slab of Perspex was placed 79.1 cm from the source to act as backscatter material (see Figure 3.1 and Figure 3.7). The source was placed at the origin and a volume of water (having dimensions of r = 2.65 cm, h = 4 mm, ρ = 1 g/cm^3) was placed at 75.6 cm. Two different simulations were constructed: a full isotropic decay of a ^{60}Co-source (the "^{60}Co-setup"), and an energy- and directionally-biased simulation (the "Biased-setup"). The biased simulation was done investigate the effects and contributions of the non-characteristic emissions of ^{60}Co to the deposited dose and dose rate. Simulations were run up to 10 MBq (10^7 ^{60}Co decays). All materials were defined according to their composition stated in the NIST materials database (built into Geant4) [39].

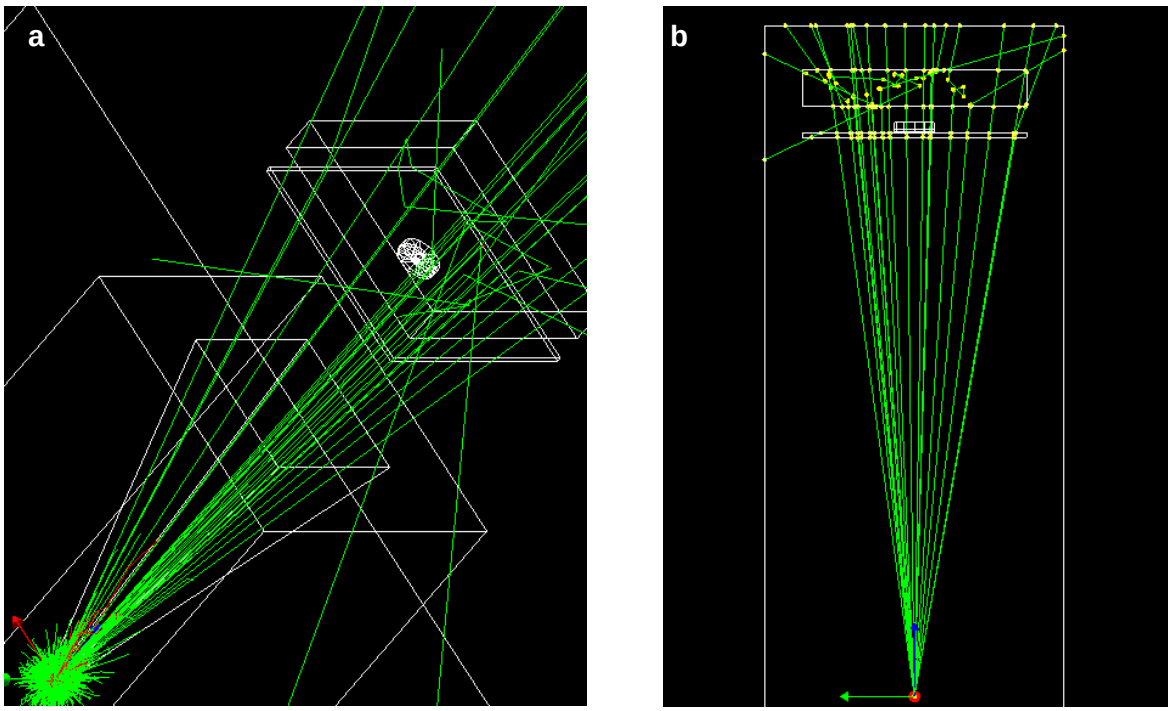

Figure 3.7. The Geant4 simulations for the ^{60}Co-setup (a) and the biased-setup (b) are shown. Photon tracks and electron tracks are coloured green and red respectively.

In the ^{60}Co-setup, a uranium housing with a 10 × 10 cm^2 square-aperture was placed around the origin, to produce a 30 × 30 cm^2 collimated field at 75 cm. In this simulation, the ^{60}Co-atoms were allowed to isotropically β^- -decay to their ^{60}Ni ground state, producing all of the documented particles and their spectrum of energies (see Figure 3.7.a).

In the physics list, the interaction processes were individually set for each type of particle, e.g. photons (photoelectric effect, Compton and Rayleigh scattering, gamma conversion), electrons and protons (ionization, bremsstrahlung, multiple scattering) with energies between 250 eV and 100 GeV. This user-defined modular physics list was used in order to incorporate the `G4RadioactiveDecay` class and further using the same processes and libraries as defined in the `QBBC` physics list. The stationary ^{60}Co-atoms were generated by using the `G4ParticleGun` class.

In the Biased-setup, the characteristic 1.173 and 1.332 MeV pair of γ-rays were produced and considered as one decay. These photons were emitted within an angle θ = 11.2° in the forward direction (see Figure 3.7.b). The built-in `QBBC` reference physics list was used to govern the particle interaction processes in this simulation [40]. The two γ-rays produced in each event were generated using the `G4GeneralParticleSource` class and the `multiplevertex` function enabled. The computed dose value should then be scaled by the corresponding fraction of the full solid angle (Ω / 4π), to compensate for the reduced solid angle representing the isotropic emissions. The following degree-to-solid angle conversion formula was used:

$$\Omega = 2\pi\,(1 - \cos\theta) \tag{3.8}$$

3.2.1.2. Dosimetry

A certain activity (Bq = disintegrations/sec) of source material was simulated and the energy deposited per second, in the investigated volume, was calculated. A cylindrical volume of water was placed away from the source and the energy deposited by any particle within this volume was recorded. Since the density and the volume of the scoring volume was known, the energy deposition rate was then converted to an absorbed dose (Gy = J/kg) rate.

3.2.2. ^{123}I simulations

In this section we describe the methods and code behind the simulation of the decay of ^{123}I using Geant4. Simply put, we wish to determine the energy deposited by particles produced in the decay of ^{123}I, at certain regions, in a sphere representing a cell.

Geant4.9.6 and Microsoft Visual C++ 2010 Express was used on a Windows 7, Intel Core i7, 8 GB RAM platform to perform the Monte Carlo simulations.

3.2.2.1. Geometry and Physics

The definition of the volumes was done in the `DetectorConstruction` initialization file. The geometry of the cell comprises of a sphere with radius r_{cell} of unit density water (`G4_WATER`), a 40 nm thick nuclear membrane with inner radius r_{nucl} – 40 nm and a 7 nm thick cellular membrane with inner radius r_{cell} – 7 nm both made out of ICRU soft tissue equivalent (`G4_TISSUE_SOFT_ICRU-4`) material [39]. The nuclear radius is set to be $r_{nucl} = 0.8 \times r_{cell}$. The world geometry was either set to be the spherical volume or a cylinder of unit density water (with height z_{cyl} and radius r_{cyl}) centred on the spherical structure.

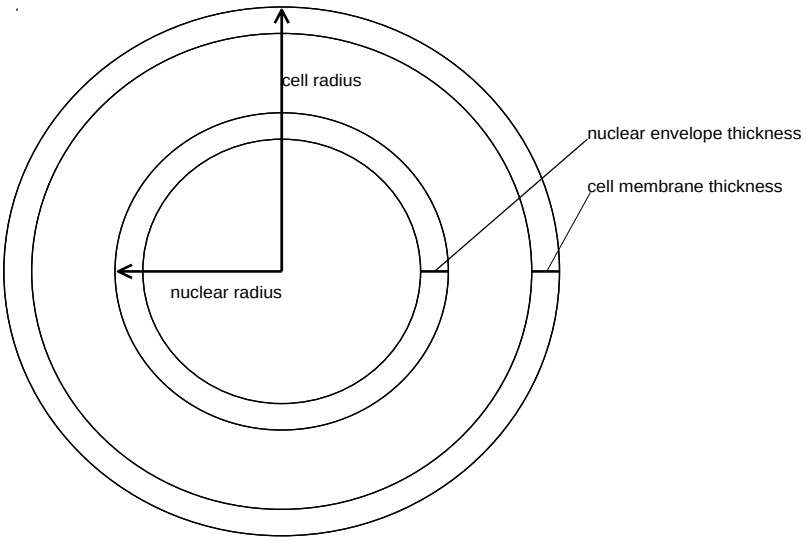

Figure 3.8. Schematic of the spherical cell geometry.

The definition of the radiation source was done in the `PrimaryGeneratorAction` initialization file and used the `G4ParticleGun` class. The source was set to be a neutral, stationary, unexcited ^{123}I atom (Z = 53, A = 123) randomly situated at a vector point $\boldsymbol{p}$ within the nucleus ($p_{x,y,z} \leq r_{nucl}$), the cytoplasm ($r_{nucl} < p_{x,y,z} \leq r_{cell}$), the cell ($p_{x,y,z} \leq r_{cell}$), one neighbor cell away ($r_{cell} < p_{x,y,z} \leq r$ = 15 μm), or in a 1 cc volume ($r_{cell} < p_{x,y} \leq r_{cyl} = \sqrt{1/\pi}$ cm and $r_{cell} < p_z \leq z_{cyl}$ = 0.5 cm).

The physics considered in the simulation was defined in the `PhysicsList` initialization file, a class of `G4VModularPhysicsList`. Default cut values were set to be 1 nm. The physics list governing electromagnetic interaction was set to be either `G4EmDNAPhysics` or `G4EmLivermorePhysics`. The `G4RadioActiveDecayPhysics` class was used to simulate the radioactive decay of the source particle. Nuclear limits were imposed to only allow the radioactive decay of particles with Z = 53 and A = 123. Bosons, Leptons, Mesons, Baryons, and Ions were constructed and transportation physics was added. The de-excitation (`G4Decay`) and fluorescence, Auger and Coster-Kronig electron, and Particle Induced X-ray Emission (PIXE) processes were activated. The minimum production cuts for photons, electrons and positrons were set to either 990 eV (default) or 250 eV.

3.2.2.2. Dosimetry

A histogram manager initialization file `HistoManager` used the data analysis framework `ROOT` to manage the histograms produced during the simulation [86]. Histograms to accumulate the following data were created: the energy deposited by electrons for *N* decays along the cell radius, the energy deposited by electrons per decay along the cell radius, the total energy deposited for *N* decays along the cell radius, the total energy deposited per decay along the cell radius, the energy deposited by electrons per decay in the nucleus, the energy deposited by electrons per decay in the cell, the total energy deposited per decay in the nucleus, the total energy deposited per decay in the cell, the projected range of charged particles produced by the decay per 100 decays, the electron energy-emission spectrum per 100 decays, the photon energy-emission spectrum per 100 decays, the electron frequency spectrum (of the ^{123}I decay) per 100 decays and the gamma-ray frequency spectrum (of the ^{123}I decay) per 100 decays.

During the `RunAction`, the following values are stored or computed as well as their root-mean-square (RMS) deviations: by the electrons or by all the particles (charged and uncharged) – the total energy deposited in the nucleus, the total energy deposited in the cell; the average projected range of the charged particles; the number of electrons and gammas produced during the decay of ^{123}I. At the end of the run, the average value of the above values are calculated for the entire run (the accumulation of all of the events) to give a corresponding value and RMS per decay of ^{123}I.

The population variance of a finite population of size N with values x_i is given by

$$\sigma^2 = \frac{\sum_{i=1}^{N} x_i^2}{N} - \left(\frac{\sum_{i=1}^{N} x_i}{N} \right)^2 \tag{3.9}$$

The standard deviation σ (also called the RMS deviation) is then computed as the square root of the variance.

The `EventAction` class stores the following values which occurred during that event: the energy deposited by electrons in the nucleus and the entire cell, the energy deposited by all particles in the nucleus and the cell, the number of electrons and gammas produced during the decay of ^{123}I. The corresponding histograms are filled with the aforementioned values at the end of each event.

In the `TrackingAction` class, before any interactions take place, if the parent atom of an electron or a gamma-ray is an ^{123}I or ^{123}Te particle, then the electron/gamma-ray is numerated and the emission and frequency histograms are updated. Once these charged particles have reached the end of their track, their displacement from their point of origin is recorded as the projected range of that particle. For the range calculations, the world geometry was set as a sphere (with $r = 3 \times r_{cell}$) around the cell. For the more energetic particles, their tracks will end when they leave the world geometry.

In the `SteppingAction` initialization class, the energy deposited E along a step is obtained and randomly distributed along the step by choosing a random point $\boldsymbol{p}$ between the `preStepPoint` and `postStepPoint` (also including those points) to represent the location of the energy deposition. Regardless of the type of particle or the region within the cell, the energy E deposited along a step is tallied as the energy deposited in the cell as well as the corresponding histograms and if the displacement from the origin $p \leq r_{nucl}$ then the energy E is added to the energy deposited in the nucleus as well as updating the corresponding histograms. If the particle is an electron, the same criteria and processes are followed and the corresponding variables and histograms reserved for electrons are updated.

3.3. Intersection of Radiobiology and Monte Carlo simulations

The knowledge of absorbed dose is required for evaluation of observed radiobiological effects and to predict or compare the effectiveness of different radionuclides. Furthermore, in radiation therapy exact dose calculation is essential for treatment planning. The RBE can be expressed by the ratio of the absorbed doses of two different radiation qualities which produce the same specified effect. This value is dependent on the spatial distribution of the energy imparted, the density of ionisations per path length of ionising particles and the

reference radiation [35]. The RBE_M is expressed by the ratio of the initial slopes of the dose-effect curves (see section 2.1.5) for the studied radiation and the reference radiation.

We note again that the biological effect of certain radiations (like Auger electrons emitted close to cellular DNA) isn't directly proportional to the delivered dose. Since the delivered dose on a cellular level is not directly measurable using current instrumentation, scientists and physicians have developed a correlation between the biological effect and delivered dose through trial and error using the concept of RBE [5]. An alternative method of theoretically predicting the delivered dose in a cell is by using Monte Carlo simulations. These simulations however, have to describe the biological composition and geometries of the material as accurately as possible, as well as the interactions of different particles with the materials.

3.3.1. Methodology and rationalization: Activity conversion & RBE calculations

We aim to convert the energy imparted by the incorporated activity A_0 in a mass m of cells into an absorbed dose value D. In order to use the calculated average energy deposited within a cell per decay of ^{123}I ($\bar{E}$, in units of eV, 1 eV = 1.6 × 10^{-19} J), the number of decays which occurred in the mass of cells needs to be determined. ^{123}I has a half-life τ of 13.2 h or 47520 s (the decay constant $\lambda = \frac{\ln(2)}{\tau}$). The activity at a time t is given by:

$$A(t) = A_0 e^{-\lambda t} = A_0 e^{-\ln(2)t/\tau} \tag{3.10}$$

The number of disintegrations after a time Δt would then be given by:

$$N(\Delta t) = \int_0^{\Delta t} A(t)dt = \frac{A_0 \tau}{ln(2)}\left[1 - e^{-ln(2)\Delta t/\tau}\right] \tag{3.11}$$

If the activity in equation (3.11) has units of Bq (disintegrations·s^{-1}) then the half-life must be in seconds as well. Following from equation (3.6) the absorbed dose in the mass m (in kg, calculated using equation (3.7) to calculate the mass of one cell) of cells is determined by:

$$D\,[Gy] = \frac{N(\Delta t) \cdot \bar{E} \cdot 1.6 \times 10^{-19}}{m} \tag{3.12}$$

There are uncertainties in the total number of disintegrations N, the average energy deposited per decay in the cell E, and the mass m of the estimated 2.5 × 10^6 cells. These uncertainties will be addressed in section 3.3.2.

The relative biological effectiveness (RBE) is expressed as the ratio of the absorbed doses of two different radiation qualities which produce the same specified effect. The dose producing the effect y can be determined by solving for D in the fitted dose-response curves (see equation (2.2)).

$$RBE = \frac{D_{reference}}{D_{test}} = \frac{D_{linear-quadratic}}{D_{linear}} = \frac{-\alpha_{reference} + \sqrt{\alpha_{reference}{}^2 + 4\beta y}}{2\beta} \div \frac{y}{\alpha_{test}} \quad (3.13)$$

Then dose limiting RBE (RBE_M) is calculated by taking the ratio of the initial slopes of the dose-effect curves for the studied radiation and the reference radiation.

$$RBE_M = \frac{\alpha_{test}}{\alpha_{reference}} \quad (3.14)$$

3.3.2. Propagation of uncertainties

If *x, y, z,…* are directly measured counts or related variables for which we know σ_x,σ_y, σ_z,… then the standard deviation from any quantity *u(x,y,z,…)* derived from these counts (ignoring co-variance in the σ_x,σ_y, σ_z,…) can be calculated from the variance [23]:

$$\sigma_u^2 = \left(\frac{\partial u}{\partial x}\right)^2 \sigma_x^2 + \left(\frac{\partial u}{\partial y}\right)^2 \sigma_y^2 + \left(\frac{\partial u}{\partial z}\right)^2 \sigma_z^2 + \ ... \quad (3.15)$$

The uncertainty of the number of disintegrations after a time Δt would then be given by

$$\sigma_N = \frac{\sigma_{A_0}\tau}{ln(2)}\left[1 - e^{-ln(2)\Delta t/\tau}\right] \quad (3.16)$$

and (from equation (3.5))

$$\sigma_{A_0} = A_0 \cdot \sqrt{\left(\frac{\sigma_\varepsilon}{\varepsilon_{abs}}\right)^2} \quad (3.17)$$

assuming no uncertainty in Δt. Following from equation (3.12), the variance of the dose is then given by

$$\sigma_D^2 = \left(\frac{E}{m}\right)^2 \sigma_N^2 + \left(\frac{N}{m}\right)^2 \sigma_{\bar{E}}^2 + \left(-\frac{N\bar{E}}{m^2}\right)^2 \sigma_m^2 \quad (3.18)$$

Similarly from equation (3.13), the RBE has a variance given by

$$\sigma_{RBE}^2 = \left(\frac{1}{D_{test}}\right)^2 \sigma_{D,reference}^2 + \left(-\frac{D_{reference}}{D_{test}^2}\right)^2 \sigma_{D,test}^2 \quad (3.19)$$

And the RBE_M variance is given by

$$\sigma_{RBE_M}^2 = \left(\frac{1}{\alpha_{reference}}\right)^2 \sigma_{\alpha,test}^2 + \left(-\frac{\alpha_{test}}{\alpha_{reference}^2}\right)^2 \sigma_{\alpha,reference}^2 \quad (3.20)$$

Chapter 4: Results & Discussion

4.1. Radiobiology results

In the following sections we discuss the results obtained from the calibration of the ^{60}Co-teletherapy unit, the detection efficiency of the RB detector, the micronucleus assay of cells exposed to ^{60}Co γ-rays and ^{132}IUdR, the determination of the S-phase fraction of the lymphocyte cultures as well as the measured cell diameters of lymphocytes and CHO cells.

4.1.1. Calibration of the ^{60}Co-teletherapy unit

By using equation (3.1), we determined from the calibration certificate that the activity of the source on the day of calibration was 48.4 TBq.

According to equation (3.2), the dose rate at a distance of 75.6 cm in air, is theoretically calculated to be 7.22 mGy/s.

The temperature and pressure on the day of calibration were 19.6°C and 1029 hPa respectively, measured using an electronic thermometer and barometer. The dose was measured as described in section 3.1.1. As shown in Figure 4.1, the dose rate of the ^{60}Co-unit is 0.490 ± 0.005 Gy/min (or 8.16 ± 0.08 mGy/s) and the correction which should be incorporated (subtracted) from exposure times is 0.01 min (solving for x when y = 0).

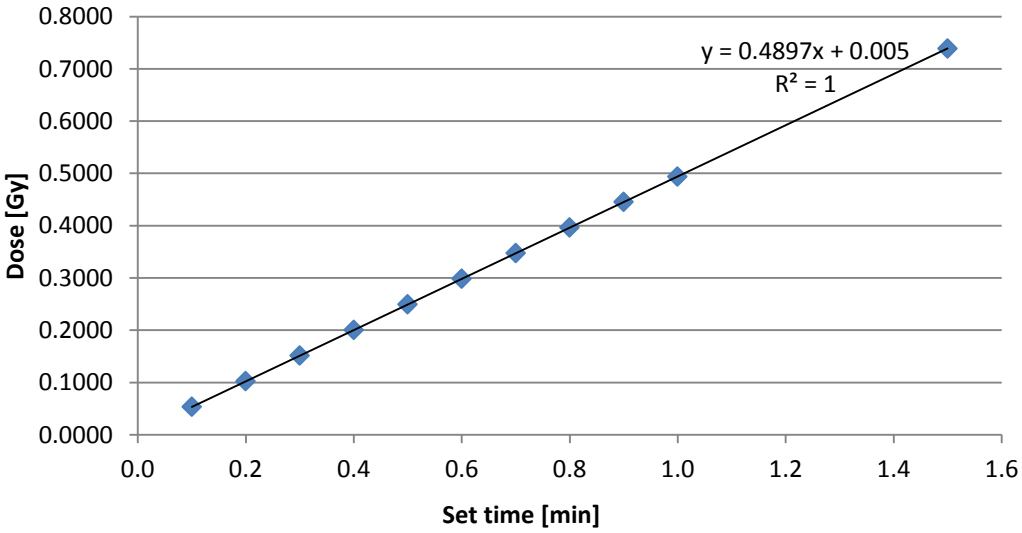

Figure 4.1. Dose measured during a set time.

We see there is a 12% difference between the theoretical dose rate (7.22 mGy/s) of equation (3.2) and the measured dose rate (8.16 ± 0.08 mGy/s). The theory calculations do not take into account the increased dose deposition due to backscatter, nor from the build-up material. The measured dose rate will be compared to the dose rate predicted by Monte Carlo simulations using Geant4 (see section 4.2.1).

4.1.2. Radiobiology and Isotope Production detectors

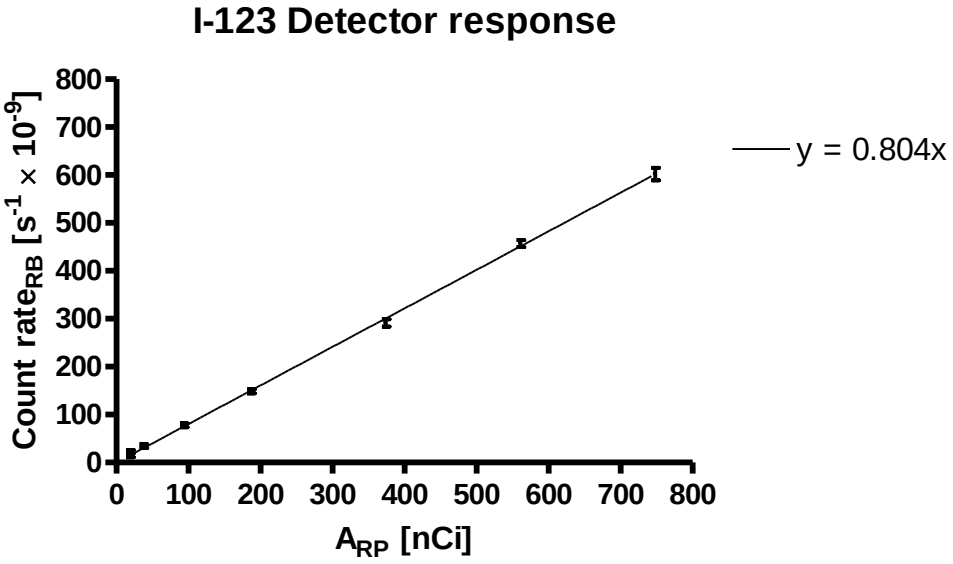

Figure 4.2. Linearity and efficiency calibration of the NaI-detector. The activity measured by RP is shown on the x-axis and the count rate of the RB detector on the y-axis.

As described in section 3.1.4, a linearity test was performed on the NaI well-detector in the Radiobiology (RB) Department. Various activity concentrations of $Na^{123}I$ in NaOH, obtained from the Radionuclide Production (RP) Department using their certified radioisotope calibrator, were diluted in water to make a 1 ml volume. The results are shown in Figure 4.2. A clear linear detection response is present for activities ranging from 10 nCi to 1 µCi. From this fitted line, the detection efficiency of the NaI detector can also be determined (see equation (3.4)). It was found that $I_\gamma \times \bar{\varepsilon}_{abs}$ = 0.804 ± 0.006 for the 159 keV γ-ray. This will be used as described in equation (3.5) to determine the incorporated activity in the various cell samples. For ^{123}I, the photopeak under considering was the 159 keV γ-ray with I_γ = 0.832 ± 0.002 [24], hence the average absolute full-energy peak detection efficiency of the NaI well-counter is $\bar{\varepsilon}_{abs}$ = 0.966 ± 0.008.

4.1.3. Micronucleus assay

4.1.3.1. ^{60}Co exposures

We note that a substantial background of free and fragmented chromosomes is present in the bEND5 cell culture slides when viewed under the microscope. This may possibly be due to the granular structure of the bEND cells and ruptured nuclei; most probably caused by the chemicals used during the preparation and trypsinizing procedures. The intracellular distribution of MNi in cytokinesis blocked CHO-K1 cells, bEND5 cells, and lymphocytes of donor 1 and 2 following exposure to graded doses of ^{60}Co γ-rays are given in Table 4.1,

Table 4.2, Table 4.3 and Table 4.4 respectively. The micronuclei per 500 binucleated cells can be calculated using the following equation:

$$\frac{\sum_{i=0}^{f} i \cdot n_i}{\sum_{i=0}^{f} n_i} \times 500 \quad (4.1)$$

where *i* represents the number of micronuclei in a binucleated cell, n_i is the number of times *i* micronuclei occurred in the scored cells and $\sum_{i=0}^{f} i \cdot n_i$ is the total number of micronuclei observed in the total number $\sum_{i=0}^{f} n_i$of binucleated cells.

Table 4.1. Average ^{60}Co dose-response for the CHO-K1 cells.

	Micronuclei frequency per binucleated cell						
Dose [Gy]	*0*	*1*	*2*	*3*	*4*	*MNi/500BN*	*± σ (MNi/500BN)*
0.0	185	15	0	0	0	37.5	9.7
0.5	180	19	0	1	0	55.0	11.7
1.0	171	27	2	0	0	77.5	13.9
1.5	167	30	2	1	0	92.5	15.2
2.0	159	34	7	0	0	120.0	17.3
2.5	129	56	14	1	0	217.5	23.3
3.0	133	46	16	3	2	237.5	24.4
3.5	125	51	18	5	1	265.0	25.7
4.0	110	66	18	5	1	302.5	27.5

Table 4.2. Average ^{60}Co dose-response for the bEND5 cells.

	Micronuclei frequency per binucleated cell							
Dose [Gy]	*0*	*1*	*2*	*3*	*4*	*5*	*MNi/500BN*	*± σ (MNi/500BN)*
0.0	854	55	5	0	0	0	35.6	4.4
0.5	467	64	8	0	0	0	75.1	8.3
1.0	296	73	13	2	0	0	136.7	13.3
1.5	157	57	16	4	1	0	219.0	21.7
2.0	151	64	21	7	2	0	271.3	23.6
2.5	198	134	55	19	3	1	387.2	21.7
3.0	55	26	15	7	1	0	396.9	43.6
3.5	92	54	30	11	2	1	416.8	33.2
4.0	174	53	42	15	5	1	355.7	24.8

Dose points above 2.5 Gy reach a plateau and are therefore not included in the fitting of curve.

Table 4.3. Average ^{60}Co dose-response for lymphocyte donor 1.

Dose [Gy]	*Micronuclei frequency per binucleated cell*						*MNi/500BN*	*± σ (MNi/500BN)*
	0	*1*	*2*	*3*	*4*	*5*		
0.00	1198	7	1	0	0	0	3.7	1.2
0.05	1252	9	0	0	0	0	3.6	1.2
0.10	1269	9	1	0	0	0	4.3	1.3
0.20	1241	12	1	0	0	0	5.6	1.5
0.50	1234	37	1	0	0	0	15.3	2.5
1.00	768	59	3	0	1	0	41.5	5.0
2.00	847	190	32	4	1	1	127.9	7.7
4.00	249	107	48	15	3	1	313.2	19.2

The 0.05 Gy, 0.10 Gy and 0.2 Gy points are too small to be accurately measured without a pan-centromeric probe and are therefore not included in the fitting of the curve.

Table 4.4. Average ^{60}Co dose-response for lymphocyte donor 2.

Dose [Gy]	*Micronuclei frequency per binucleated cell*					*MNi/500BN*	*± σ (MNi/500BN)*
	0	*1*	*2*	*3*	*4*		
0.00	1722	13	4	0	0	6.0	1.3
0.25	757	16	0	0	0	10.3	2.6
0.50	1529	53	5	2	0	21.7	2.6
1.00	1127	68	8	0	0	34.9	3.8
2.00	724	130	13	3	0	94.8	7.4
3.00	500	168	45	8	0	195.6	11.6
4.00	635	195	70	6	1	196.8	10.4

Dose points above 3.0 Gy reach a plateau and are therefore not included in the fitting of the curve.

The micronuclei present in 500 binucleated cells per dose point when exposed to ^{60}Co γ-radiation for the rat brain endothelial (bEND5), Chinese hamster ovarian cell (CHO), and the two lymphocyte donors are displayed in Figure 4.3, along with their fitted linear-quadratic response curves; the coefficients of which are given in Table 4.5.

Error bars are present for the bEND5 and CHO-K1 cell lines and the lymphocyte donors, but may in some cases be smaller than the representing symbol due to the scales of the axes. The CHO-K1 cell line was available to be scored by Acridine Orange. Scoring cells by hand is extremely time consuming and strenuous.

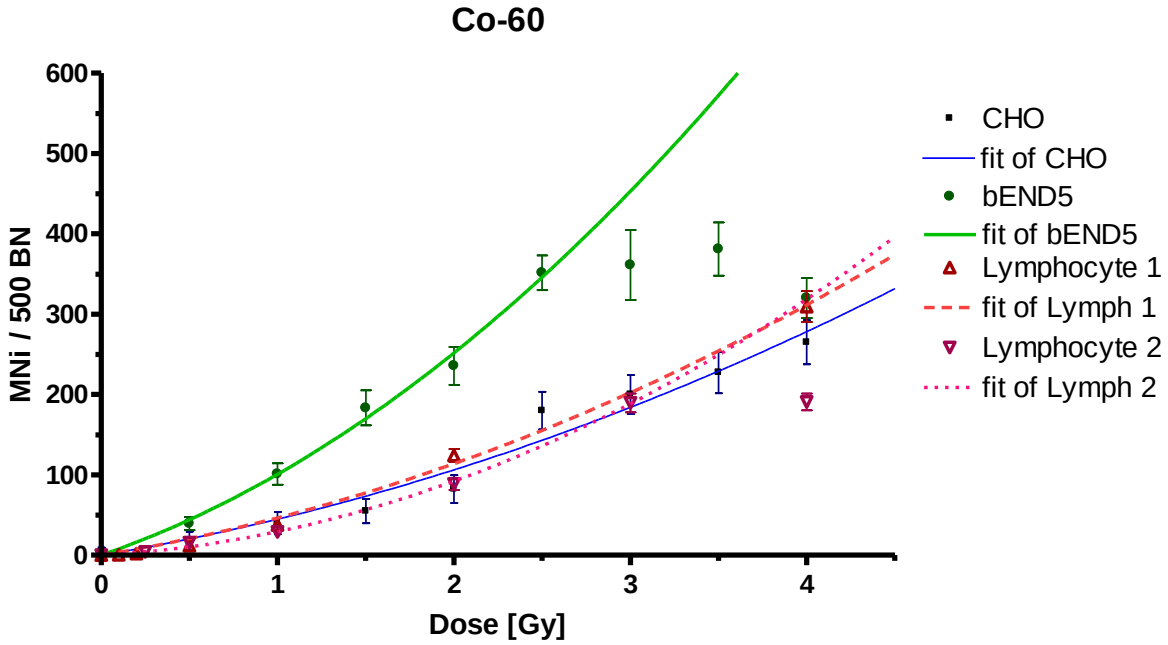

Figure 4.3. Dose-response of cell lines when exposed to ^{60}Co radiation. The fitted linear-quadratic curves for the CHO and bEND5 cells are shown as solid lines and those of the two lymphocyte donors are shown as dotted lines.

For the bEND5 cells we see that points above 2.5 Gy reach a plateau and similarly for the second lymphocyte donor above 3.0 Gy, indicating that the cells have been saturated by the radiation. This retarded response can be attributed to radiation induced mitotic delay, apoptosis and necrosis, which limit the number of BN cells viable for scoring. From Figure 4.3 we can see that the bEND5 cells are significantly more radiosensitive than the CHO-K1 cells, also indicated by the larger α-value in Table 4.5. Also given in Table 4.5 is the dose response curve for the average micronucleus response for a group of 10 lymphocyte samples exposed to ^{60}Co γ-radiation, determined by Willems *et al*. in a study of automated micronucleus scoring for population triage in case of a large scale irradiation event [34].

Table 4.5. The coefficients of the ^{60}Co radiation dose-response fits for MNi/500BN frequencies.

Cell line	*α* (Gy^{-1})	*β* (Gy^{-2})
CHO-K1	36.6 ± 11.2	8.2 ± 3.4
bEND5	75.7 ± 12.2	25.1 ± 5.8
Lymphocyte 1	35.9 ± 7.3	10.5 ± 2.0
Lymphocyte 2	12.3 ± 3.2	16.8 ± 1.2
Gen. Lymphocyte [34]	19.7 ± 0.4	15.9 ± 0.2

From the two sets of lymphocyte data we can see there is an inter-donor variability in the dose-response (by a factor of 2.9) and hence radiosensitivity. This inter-donor variability was

also observed by Slabbert *et al*. (2010) and Vral *et al*. (1994) [87], [32]. Slabbert *et al*. also noted that lymphocytes have been observed to be more radioresistant to ^{60}Co irradiation compared to CHO cells (i.e. lymphocytes have a smaller α value) [13]. The CHO cells being more radiosensitive to ^{60}Co radiation when compared to lymphocytes was seen in the current study, especially with regards to donor 2 and the general lymphocyte response. From Figure 4.3 we can see a difference in radiosensitivity for each cell line, as discussed in Section 2.1.3.

We see that the linear-quadratic dose-response and inter-donor variation of radiosensitivity for our two lymphocyte donors is similar to that of Willems *et al*. and Slabbert *et al*. studying micronuclei inductions in stimulated human lymphocytes exposed to ^{60}Co γ-radiation [34], [87].

The linear-quadratic trend is present in all three cell lines, as it should for the low LET γ-rays. The values for each dose point will differ when compared to values available in literature, as they are dependent on the specific cell line, the scoring method used and the cell culture itself [28].

The above equations which describe the dose-response of lymphocytes exposed to ^{60}Co γ-rays will be used as reference radiation in following RBE calculations.

4.1.3.2. ^{123}I exposures

5-[^{123}I]-iodo-2-deoxyuridine was obtained from the Radionuclide Production Department at iThemba LABS. The addition and exposure of lymphocytes from two male donors was done as explained in Section 3.1.2. The biological response to the ^{123}I irradiation was investigated using the cytokinesis-blocked micronucleus assay as described in Section 3.1.3.

We note that significant amounts of cells were lost during the washing procedures, ultimately resulting in only one slide per dose point being available for scoring by hand using fluorescence microscopy. The incorporated activity-response for both lymphocyte donors are shown in Figure 4.4. On this figure, the activity incorporated by the cells (measured using the NaI well-counter) and the induced micronuclei (MNi) in 500 binucleated (BN) cells are shown. We note that the measured activity remaining after the washing procedure is an overestimate of the true incorporated activity; since extracellular activity is always present due to inefficient washing procedures e.g. supernatant containing ^{123}I may remain after a wash step to prevent the reduction of the cell pellet. Even though some activity may be located within the medium surrounding the cells, it was assumed that all of the measured activity was incorporated into the DNA of the lymphocytes – hence an overestimation of the true incorporated activity. In future, alternate methods in separating the unincorporated activity from the cells could be investigated.

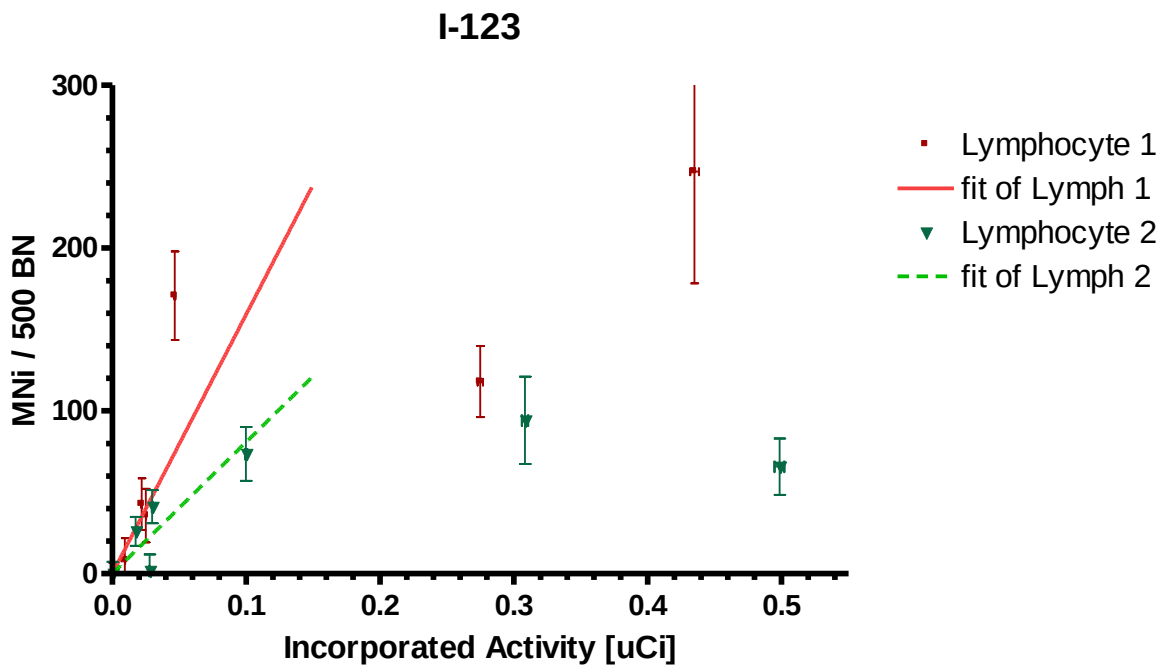

Figure 4.4. Activity - response curve for lymphocytes which incorporated ^{123}I.

Horizontal error bars are present at each data point but may be too small to see due to the scale of the horizontal axis. As shown on Figure 4.4, a linear activity-response was established for the first few points; the parameters of the fitted lines are given in Table 4.6. Similarly to the ^{60}Co-exposures, there are points which deviate from the linear relationship at higher activities. Likewise, the deviation from linearity can be attributed to radiation induced mitotic delay, apoptosis and necrosis, which limit the number of BN cells viable for scoring. The linear dose response is indicative of the high-LET nature of the Auger electrons if emitted close to cellular DNA [13]. Studies of radioactive iodine (or any other Auger emitter) incorporated directly into the DNA of human T-lymphocytes have not been reported thus far in literature. Similar to the ^{60}Co-exposure, a significant variation in the biological response can be noted for the two lymphocyte donors (by a factor of 2.0). Studies have reported a reduction in the variation of inter-donor radiosensitivities of T-lymphocytes for other forms of high-LET radiation like fast neutrons and α-particles when compared to low-LET radiation like ^{60}Co γ-rays [87], [28], [32]. This effect was also seen in the current study (reducing from 2.9 to 2.0).

Table 4.6. The coefficients of the ^{123}I activity - response fits for MNi / 500 BN frequencies.

Cell line	*α (μCi^{-1})*	*R^2*
Lymphocyte 1	1592 ± 186	0.90
Lymphocyte 2	808 ± 121	0.83

In the following sections it will be attempted to convert the incorporated activity (μCi) into an absorbed dose (Gy) value in order to compare the ^{123}I exposures to ^{60}Co exposures.

4.1.4. S-phase fraction of lymphocytes

As described in Section 3.1.5, the fraction of lymphocytes in S-phase 44 hours post start-up was determined using lymphocytes from donor 2. The fraction of T-lymphocytes which incorporated the BrdU was found to be 0.220 of the scored lymphocytes. This indicates the number of the 2.5×10^6 cells seeded in each culture which would have incorporated the ^{123}IUdR during the exposure period. Personal communication with lymphocyte donor 1 reported approximately the same fraction in previous S-phase studies at 44 hours using BrdU.

The same lymphocyte culture of donor produced a binucleation index[8] of 35.7%, 72 hours post culture start-up. The larger binucleation index is due to the fact that, not only the cells which were in S-phase at 44 hours post culture start-up but also the cells after and perhaps before the S-phase (at 44 hours) are prevented from performing cytokinesis and will as such present as binucleated cells.

4.1.5. Cell sizes

The average cell diameter and resulting cell radius, measured as described in Section 3.1.6, for the lymphocytes and CHO cells are shown in Table 4.7.

Table 4.7. Average cell diameters and radii.

	Cells counted	*Diameter ± σ (μm)*	r_{cell} *± σ (μm)*	*Volume (μm^3)*
Lymphocyte	54	9.76 ± 1.69	4.88 ± 0.85	~ 486
CHO	93	11.64 ± 1.11	5.82 ± 0.55	~ 826

For comparison, Warters and Hofer assumed the CHO cells were spheres of radius 6.4 μm (~ 1098 μm^3) in their dosimetry work [22]. It has been reported by the IAEA that G_0 peripheral small lymphocytes have large dense nuclei surrounded by relatively little cytoplasm. They have a cell diameter of around 6 μm and the volume is estimated to be around 110 μm^3 [18], [20]. Under the influence of PHA, the lymphocytes are transformed into blastoid cells, and the volumes of the nucleus and of the whole cell increases. Peripheral lymphocytes 48 hours after stimulation have a cell volume of about 500 μm^3, as compared with ~110 μm^3 before stimulation. The cytoplasmic volumes are ~50 μm^3 before and ~350 μm^3 after stimulation. Nuclear volume increases from about ~50 μm^3 (45% of the entire cell) to ~150 μm^3 (30% of the entire cell) following stimulation.

[8] The fraction of the total cells scored which had two main nuclei.

The diameter of the lymphocyte nucleus in our current calculations was taken to be 80% of the total cell diameter to coincide with similar work done by Kassis *et al*. [3] and Bousis *et al*. [14]. The nuclear membrane was considered to be 40.0 nm thick and the cell membrane 7.00 nm thick [83], [84], [85].

4.2. Monte Carlo simulations results

In the following sections the results of the Geant4 simulations with regards to the ^{60}Co and ^{123}I work as previously discussed will be described.

4.2.1. ^{60}Co simulations

Shown in Figure 4.5 are the data points for the Biased- and ^{60}Co-setups as described in section 3.2.1, as well as the fitted curve of the Biased-setup and the same curve scaled to compensate for the reduced solid angle.

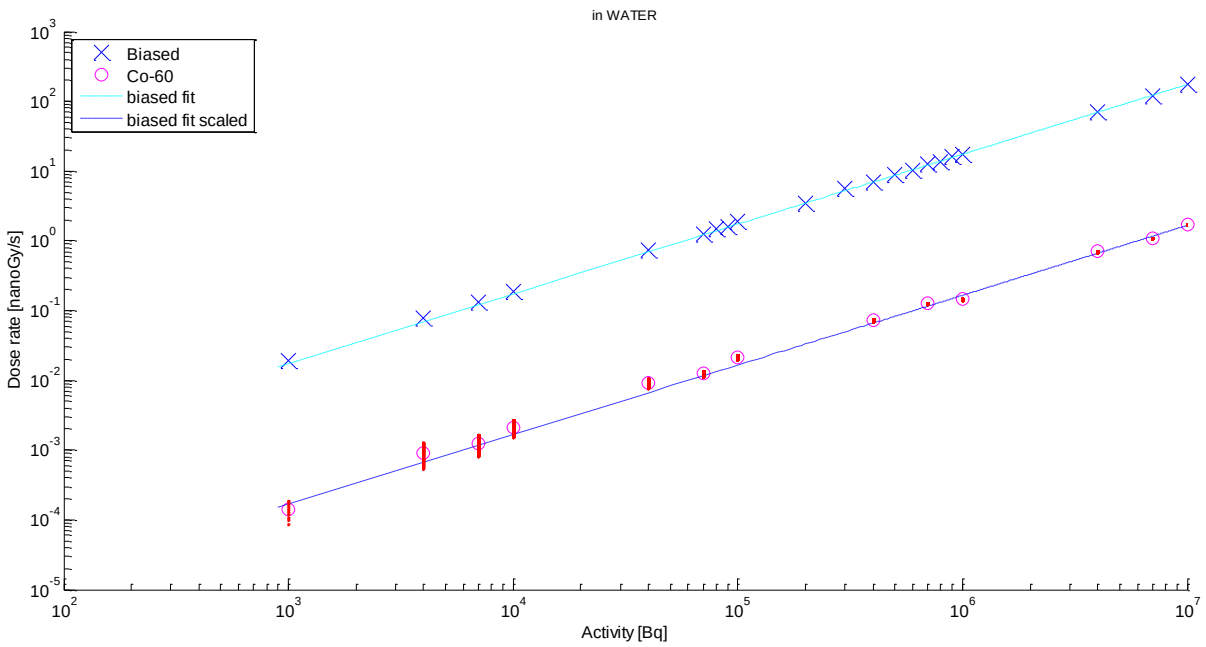

Figure 4.5. Dose rate (nGy/s) as a function of Activity (Bq) for the Biased- and ^{60}Co-simulations.

Since this scaled curve, fitted to the Biased-simulated data points, matches the ^{60}Co-setup data points, it can be concluded that the solid angle scaling is correct and that the effect of the other particles produced in the full isotropic decay of ^{60}Co can be considered to be negligible. The fitted curves of the “Biased” (once scaled to compensate for the decreased solid angle) and ^{60}Co simulated data points are given by the following respective two linear equations, with dose rate in nGy/s and activity in Bq:

$$\dot{D} = \frac{0.1197}{4\pi}(174.2 \times 10^{-7}) \cdot A \tag{4.2}$$

$$\dot{D} = (1.663 \times 10^{-7}) \cdot A \tag{4.3}$$

The 95% confidence interval for the above dose rates can be obtained by multiplying $\dot{D}$ with 0.3%. Given in Table 4.8 are the comparisons between the measured dose rate and those predicted by the fitted equations (4.2) and (4.3) when working with the documented activity (48.4 TBq) of the therapy units' source; as well as the percentage difference between the measured and the simulated value.

Table 4.8. Comparison of measured and simulated dose rate values.

	Dose rate (mGy/s)	% difference
Measured value	8.16 ± 0.08	0
(4.2) Biased simulation	8.03 ± 0.03	1.6 ∓ 0.3
(4.3) ^{60}Co-simulation	8.05 ± 0.03	1.4 ∓ 0.3

The Monte Carlo simulations give the most accurate results when the coefficients in the above equations were calculated assuming a full isotropic decay of the ^{60}Co source. Overall, Geant4 produces results with an accuracy of at least 98%. If a similar volume of blood (ρ = 1.06 g/cm^3) was used in the Geant4 simulations, an increase of only 0.6% was seen in the dose rate, when compared to that of water (ρ = 1.00 g/cm^3), due to the increased density and more complex composition of the blood material in the scoring volume.

Depicted in Figure 4.6 are the dose rate curves for when the build-up and backscatter slabs are included or neglected in the Biased simulation. A difference of 28% in dose deposition exists for the two cases, indicating the effect the build-up and backscatter material has on the deposited dose.

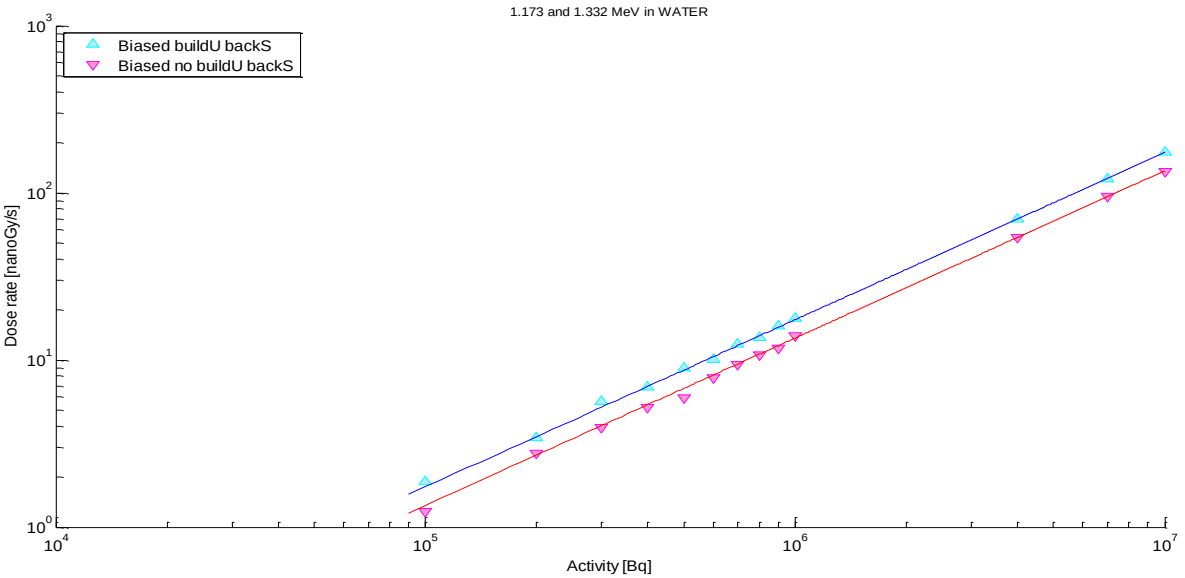

Figure 4.6. Influence of the build-up and backscatter in dose deposition.

The main advantage in doing the Biased simulation is the computational time. Simulating 7×10^6 Bq decays result in a computational time of 55.9 min for the Biased setup and 149.7 min for the ^{60}Co-setup. Normal teletherapy units have activities in the 10^{13} Bq region which would result in a computational time of years for current personal computers.

4.2.2. ^{123}I simulations

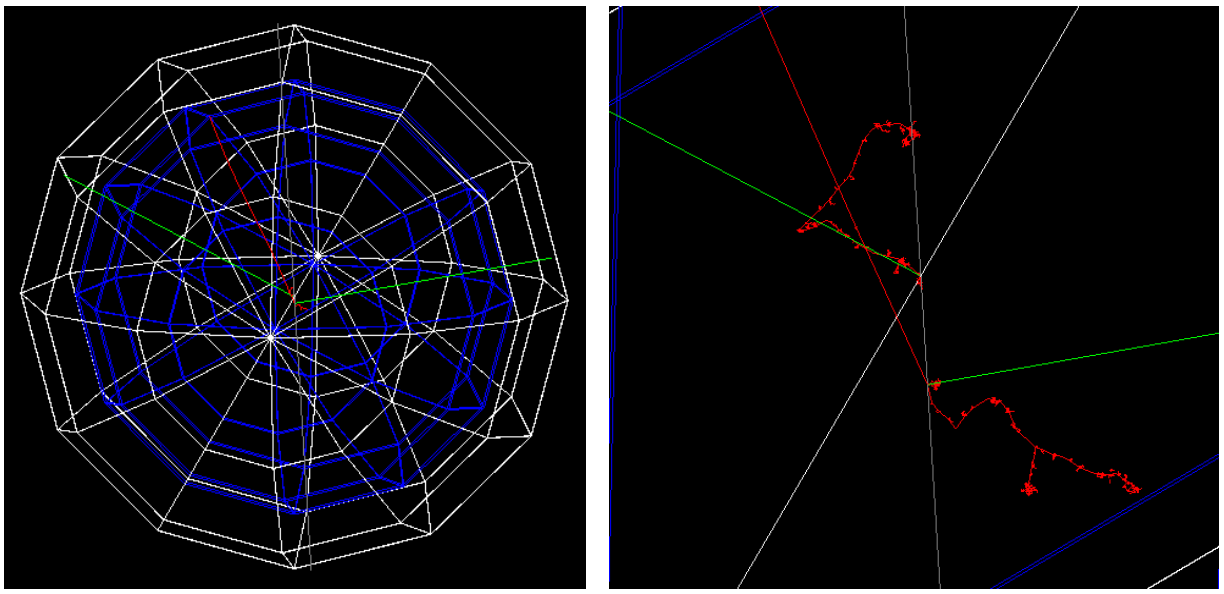

Figure 4.7. Particle tracks resulting from the decay of one I-123. The left figure shows the sphere representing the lymphocyte with the nucleus shown in blue. In the shown example, a 127 keV IC electron (red) and two X-rays (green) were produced and can be seen leaving the cell. The right figure shows the dense ionization clusters of the low energy electrons (when the center of the left figure is enhanced) emitted during the relaxation process foretelling the high-LET nature of the Auger electrons.

Dose dependence on size

In the following computations, the Livermore Low Energy physics list (default production cuts) was used to simulate the energy deposition in the cell (nucleus + cytoplasm) by all particles produced by the decay of 10^6 ^{123}I-atoms randomly generated within the nucleus. Table 4.9 shows the resultant average energy deposited in the cell per ^{123}I decay for various cell radii, as well as the computational time required to perform the 10^6 simulated decays in that geometry. It is interesting to note that the computational time decreases as the size of the (already very small) sphere increases. This may be because the multiple-scattering approximation used in the Livermore physics list performs better for larger geometries and more corrections need to be calculated for smaller geometries.

Table 4.9. Average energy deposited in the cell per ^{123}I decay as a function of cell radius.

r_{cell} (μm)	$\bar{T}_{cell}$ (keV) ± σ (eV)	Time (min)
4.8773	4.660 ± 0.005	104.3
5.8199	5.036 ± 0.005	103.7
6.0000	5.116 ± 0.006	99.9
10.000	6.294 ± 0.008	90.0

For comparison, the energy absorbed in a 5 μm radius sphere of unit density water can be calculated to produce 5.1 keV per ^{123}I decay using Howell's AAPM spectra and 5.2 keV per ^{123}I decay using Humm's (1989) spectra and Cole's (1969) electron range-energy relationship [57], approximately 0.5 keV higher than was found in the current study. It was already discussed in section 2.3.1 that the spectra by Howell and Humm include the N and O shell electrons and the spectrum used by Geant4 and the ICRP do not.

The energy deposited in the volume increases linearly with the cell radius (an increased volume). As shown in Figure 4.8, this increase can be described by the fitted linear equation:

$$E\ [keV] = 0.3062 \cdot r_{cell}\ [\mu m] + 3.245 \tag{4.4}$$

The small slope indicates that a large increase in cellular radius will not result in a large increase in deposited energy, and that the largest fraction of the energy available for emission is already deposited within a 5.0 μm radius. We note that the total energy deposited per decay does level off for volumes with cell radius above 200 μm. These results are not reported in the current study.

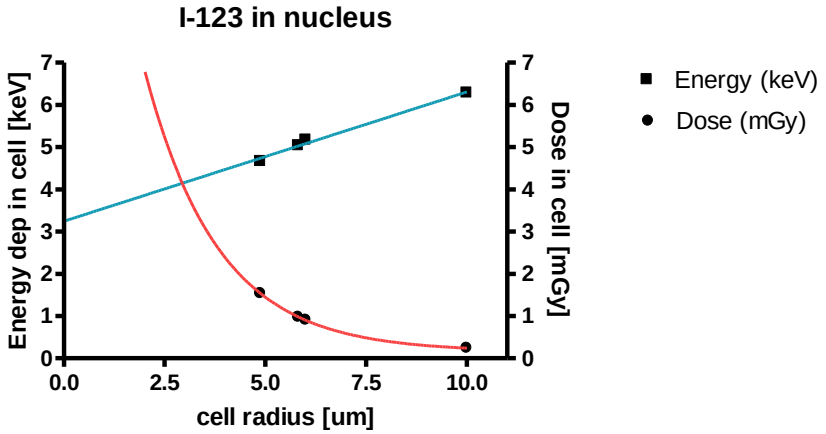

Figure 4.8. Absorbed energy (left axis) and dose (right axis) dependence on cell radius.

Figure 4.8 shows the trend of the absorbed dose per decay as the size of the cell increases. The decaying trend can be surmised from equations (3.6) and (3.7) and can be described by the fitted equation:

$$D\ [mGy] = 19.98 \cdot e^{-0.55 \cdot r\ [\mu m]} + 0.16 \tag{4.5}$$

We see that the absorbed dose decreases rapidly when the radius of the cell is increased from 2.5 μm to 5.0 μm. It is essential that the correct cell size is used in the simulations, as it will eventually influence the RBE calculations.

Source distribution in various regions

In the following computations, the Livermore Low Energy physics list was used to simulate the energy deposition in the cell and nucleus by particles produced by the decay of 10^6 ^{123}I-atoms, with r_{cell} = 4.88 μm and a 990 eV production cut value. Table 4.10 shows the average energy deposited in the nucleus and the entire cell per ^{123}I decay by the electrons ($\bar{E}$) or all particles ($\bar{T}$, including ions and photons) for when the ^{123}I sources were randomly generated in (i) the nucleus (r_{nucl} = 0.8× r_{cell}); (ii) the cytoplasm; (iii) the cell; (iv) one neighbour cell away, or (v) a 1 cm^3 volume. Table 4.11 shows the total energy deposited in those regions due to all of the 10^6 ^{123}I decays.

Table 4.10. Average energy deposited per ^{123}I decay in various cell regions.

	$\bar{E}_{nucl}$ (keV) ± σ (eV)	$\bar{E}_{cell}$ (keV) ± σ (eV)	$\bar{T}_{nucl}$ (keV) ± σ (eV)	$\bar{T}_{cell}$ (keV) ± σ (eV)
i	4.217 ± 0.004	4.653 ± 0.005	4.224 ± 0.004	4.660 ± 0.005
ii	0.576 ± 0.003	4.178 ± 0.004	0.576 ± 0.003	4.184 ± 0.004
iii	3.486 ± 0.004	4.557 ± 0.004	3.491 ± 0.004	4.564 ± 0.004
iv	0.024 ± 0.000	0.053 ± 0.000	0.024 ± 0.000	0.053 ± 0.000
v	0.000	0.000	0.000	0.000

Bousis *et al*. (2012) used an in-house MC code and the spectrum of Howell *et al.* [4] and considered a cell with cell radius 5 μm and nuclear radius 4 μm. They found the energy deposited in the cell to be 5.4 keV per ^{123}I decay when distributed in the cell; the energy in the nucleus to be 5.1 keV per ^{123}I decay when distributed in the nucleus, and 0.56 keV per ^{123}I decay in the nucleus when distributed in the cytoplasm [14]. It was already discussed in section 2.3.1 that the spectra by Howell (AAPM) differ from the spectrum used by Geant4.

Table 4.11. Total energy deposited per 10^6 ^{123}I decays in various cell regions.

	E_{nucl} (GeV) ± σ (keV)	E_{cell} (GeV) ± σ (keV)	T_{nucl} (GeV) ± σ (keV)	T_{cell} (GeV) ± σ (keV)
i	4.22 ± 3.66	4.65 ± 4.53	4.22 ± 3.66	4.66 ± 4.53
ii	0.58 ± 2.55	4.18 ± 4.20	0.58 ± 2.55	4.18 ± 4.20
iii	3.49 ± 3.75	4.56 ± 4.46	3.49 ± 3.75	4.56 ± 4.46
iv	0.05 ± 0.50	0.11 ± 0.77	0.05 ± 0.50	0.11 ± 0.77
v	0.000	$0.98\times10^{-6} \pm 0.07\times10^{-3}$	0.000	$0.98\times10^{-6} \pm 0.07\times10^{-3}$

From Table 4.10 and Table 4.11, comparing the energy deposited by the electrons to the energy deposited by all particles, we see that most of the energy deposited within the nucleus and the cytoplasm are from electrons, most probably the low energy electrons (Auger and CK), similarly found by Bousis *et al.* [14]. There is a large energy deposition within the nucleus when the ^{123}I is distributed within the nucleus or the entire cell, in contrast to when the ^{123}I only decays in the cytoplasm or outside the cell. This also indicates that the majority of the energy is deposited by the low energy electrons and that they cannot significantly contribute to the nuclear dose if the ^{123}I does not decay inside the nucleus.

A small cross-dose (from the neighbour cells) is present, which is most probably due to the internal conversion electrons or the characteristic gamma and X-rays, also indicating that the Auger electrons have ranges much smaller than the diameter of a cell in which they deposit their energy. Similar aspects were examined by Sastry *et al*. (1985, [57]), Goddu *et al*. (1994, [67]) and Freudenberg *et al*. (2011, [5]) who found that the self-dose dominates even when the cell is in a cluster of cells containing Auger emitters localized in their nuclei.

The energy deposited within the cellular volume when the sources are distributed randomly around it in a 1 cc volume can be considered to be negligibly small. Hence, only activity absorbed into a cell will contribute the dose absorbed in the mass of cells.

Various nuclear radii have been reported and used in calculations when considering cellular dosimetry in cells representing lymphoma. To this end we investigate the influence on the cellular dose if we decrease our nuclear radius from 0.8× r_{cell} to 0.5× r_{cell}.Table 4.12 shows the average energy deposited in the nucleus and the entire cell per ^{123}I decay by the electrons ($\bar{E}$) or all particles ($\bar{T}$, including ions and photons) for when the ^{123}I sources were randomly generated in the nucleus (r_{nucl} = 0.5× r_{cell}). We see a decrease in the amount of energy deposited within the nucleus and only a 1.5% increase in the energy deposited within the entire cell when the radius of the nucleus is reduced from 80% to 50% of the cell radius.

Table 4.12. Average energy deposited per decay in the nucleus = 0.5*cell.

$\bar{E}_{nucl}$ (keV) ± σ (eV)	$\bar{E}_{cell}$ (keV) ± σ (eV)	$\bar{T}_{nucl}$ (keV) ± σ (eV)	$\bar{T}_{cell}$ (keV) ± σ (eV)
3.806 ± 0.003	4.722 ± 0.005	3.812 ± 0.003	4.728 ± 0.005

Energy deposition dependence on production cuts

In the following computations, the Livermore Low Energy physics list was used to simulate the energy deposition in the cell and nucleus by particles produced by the decay of 10^6 ^{123}I-atoms, with r_{cell} = *4.88* μm. The tables below compare the average energy deposited in the

nucleus and the entire cell due to the electrons, to all the particles, as well as the computational time; obtained when using the default 990 eV or the forced 250 eV production cut values (see section 2.2.1 and 2.2.3). Table 4.13, Table 4.14, and Table 4.15 respectively show the results when the sources are randomly generated in the nucleus ($r_{nucl} = 0.8 \times r_{cell}$), the cytoplasm and the entire cell.

Table 4.13. ^{123}I source within the nucleus.

	990 eV	*250 eV*
$\bar{E}_{nucl}$ *(keV) ± σ (eV)*	4.217 ± 0.004	4.168 ± 0.003
$\bar{T}_{nucl}$ *(keV) ± σ (eV)*	4.224 ± 0.004	4.175 ± 0.003
$\bar{E}_{cell}$ *(keV) ± σ (eV)*	4.653 ± 0.005	4.571 ± 0.004
$\bar{T}_{cell}$ *(keV) ± σ (eV)*	4.660 ± 0.005	4.578 ± 0.004
Time (min)	104.3	208.0

Table 4.14. ^{123}I source within the cytoplasm.

	990 eV	*250 eV*
$\bar{E}_{nucl}$ *(keV) ± σ (eV)*	0.576 ± 0.003	0.519 ± 0.002
$\bar{T}_{nucl}$ *(keV) ± σ (eV)*	0.576 ± 0.003	0.520 ± 0.002
$\bar{E}_{cell}$ *(keV) ± σ (eV)*	4.178 ± 0.004	4.008 ± 0.004
$\bar{T}_{cell}$ *(keV) ± σ (eV)*	4.184 ± 0.004	4.094 ± 0.004
Time (min)	79.7	156.6

Table 4.15. ^{123}I source within the entire cell.

	990 eV	*250 eV*
$\bar{E}_{nucl}$ *(keV) ± σ (eV)*	3.486 ± 0.004	3.439 ± 0.004
$\bar{T}_{nucl}$ *(keV) ± σ (eV)*	3.491 ± 0.004	3.444 ± 0.004
$\bar{E}_{cell}$ *(keV) ± σ (eV)*	4.557 ± 0.004	4.477 ± 0.004
$\bar{T}_{cell}$ *(keV) ± σ (eV)*	4.564 ± 0.004	4.484 ± 0.004
Time (min)	99.1	197.0

We clearly see an increase in computational time required, since more lower-energy particles are being produced (because the minimum particle production energy was lowered) and need to be tracked.

There is however a decrease in the deposited energy. This follows from the fact that if a particles energy does not exceed the production cut, that particle will no longer produce secondary particles; coupled with the fact that the Livermore Low Energy physics list

approximates the energy deposited and the step length during a step (using the multiple scattering method previously discussed), shows that it noticeably overestimates the energy deposited per track, especially for higher energy particles. The small deviation of deposited energy is however acceptable if the computational time needs to be minimized.

Again we see that there is a significant dependence on the region where the ^{123}I decays, and that the majority of the energy deposited is due to the low energy electrons.

The Livermore- vs DNA physics list

The following results are computed from the energy deposition in the cell and nucleus by particles produced by the decay of ^{123}I-atoms, with r_{cell} = 4.88 μm and the source atoms randomly distributed within the nucleus ($r_{nucl} = 0.8 \times r_{cell}$). Table 4.16 below compares the average energy deposited in the nucleus and the entire cell per ^{123}I decay due to the electrons ($\bar{E}$) or to all the particles ($\bar{T}$), the number of simulated decays with the computational time required, the average range of the charged particles produced during the decay, and the average number of electrons and photons produced during the decay; obtained when using the Livermore Low Energy physics list (990 eV and 250 eV production cuts) or the Geant4-DNA physics list (default production cuts).

Table 4.16. Livermore vs DNA.

	Livermore (990 eV)	*Livermore (250 eV)*	*Geant4-DNA*
$\bar{E}_{nucl}$ *(keV) ± σ (eV)*	4.217 ± 0.004	4.168 ± 0.003	4.07 ± 0.32
$\bar{T}_{nucl}$ *(keV) ± σ (eV)*	4.224 ± 0.004	4.175 ± 0.003	4.07 ± 0.32
$\bar{E}_{cell}$ *(keV) ± σ (eV)*	4.653 ± 0.005	4.571 ± 0.004	4.43 ± 0.38
$\bar{T}_{cell}$ *(keV) ± σ (eV)*	4.660 ± 0.005	4.578 ± 0.004	4.43 ± 0.38
No. of decays	10^6	10^6	10^4
Time (min)	104.3	208.0	140.5
Avg. projected range	3.0 ± 2.9 μm	2.9 ± 2.9 μm	7.9 ± 5.7 μm
Electrons	2.62 ± 1.56	2.63 ± 1.56	2.63 ± 1.56
Photons	1.80 ± 0.54	1.80 ± 0.54	1.76 ± 0.57

We note that up to a 3% difference is present in the energy deposited when computed by the Livermore and DNA physics lists.

We see there is again a difference between the energy deposited in the nucleus and the entire cell. When using the Livermore physics list a difference of 5% (990 eV and 250 eV) is

found and using the DNA physics list we get a 4% difference between the cellular and nuclear deposition.

The energy values computed using either the Livermore or the DNA physics list deviates 4.9 – 9.6% from the 4.9 keV per disintegration value used in activity-to-dose conversion calculations done by Kassis *et al*. [3], Makrigiorgos *et al*. [64] and Goddu *et al*. [58] using Cole's (1969) approach, in which they considered a cell with a cell radius of 5 μm and a nuclear radius of 4 μm. Humm *et al*. (1989) reported that the mean energy deposited in an 8 μm diameter nucleus per ^{123}I decay was approximately 4.88 keV [54].

The computational time required when using the DNA physics list is significantly more than the time required when using the Livermore physics list (990 eV), especially considering 100 times fewer decays are simulated. This is because the DNA physics list simulates each particle's interaction explicitly and does not make use of the multiple scattering method like the Livermore physics list does.

The calculation of the projected range includes all charged particles produced by either the ^{123}I-atom or the excited ^{123}Te-atom. This includes the high energy internal conversion electrons, the low energy electrons as well as the Te-ion. Since the internal conversion electron have ranges far larger than the cell geometry, we can conclude that the majority of the low energy electrons will not have ranges exceeding the tabulated values.

All of the above differences could be explained by the fact that the DNA physics list does not approximate the energy deposited, step length or direction of a step according to some model (such as the Multiple Scattering model, default in the Livermore physics list).

The number of electrons produced on average per decay of ^{123}I is close to the value of 3.05 reported by the ICRP, who also report a value of 1.72 photons emitted on average per decay [51].

The electron range spectrum

The calculation of the projected range includes all charged particles produced by either the ^{123}I-atom or the excited ^{123}Te-atom. This includes the high energy internal conversion electrons, the low energy electrons as well as the Te-ion. Shown in Figure 4.9 is the frequency spectrum per 100 ^{123}I decays of the range of charged particles calculated using the Livermore physics list, and similarly in Figure 4.10 using the DNA physics list. The spectra's range extends to almost $2\times r_{cell}$, in order to obtain an estimate of the fraction of particles which have ranges less than the diameter of the cell.

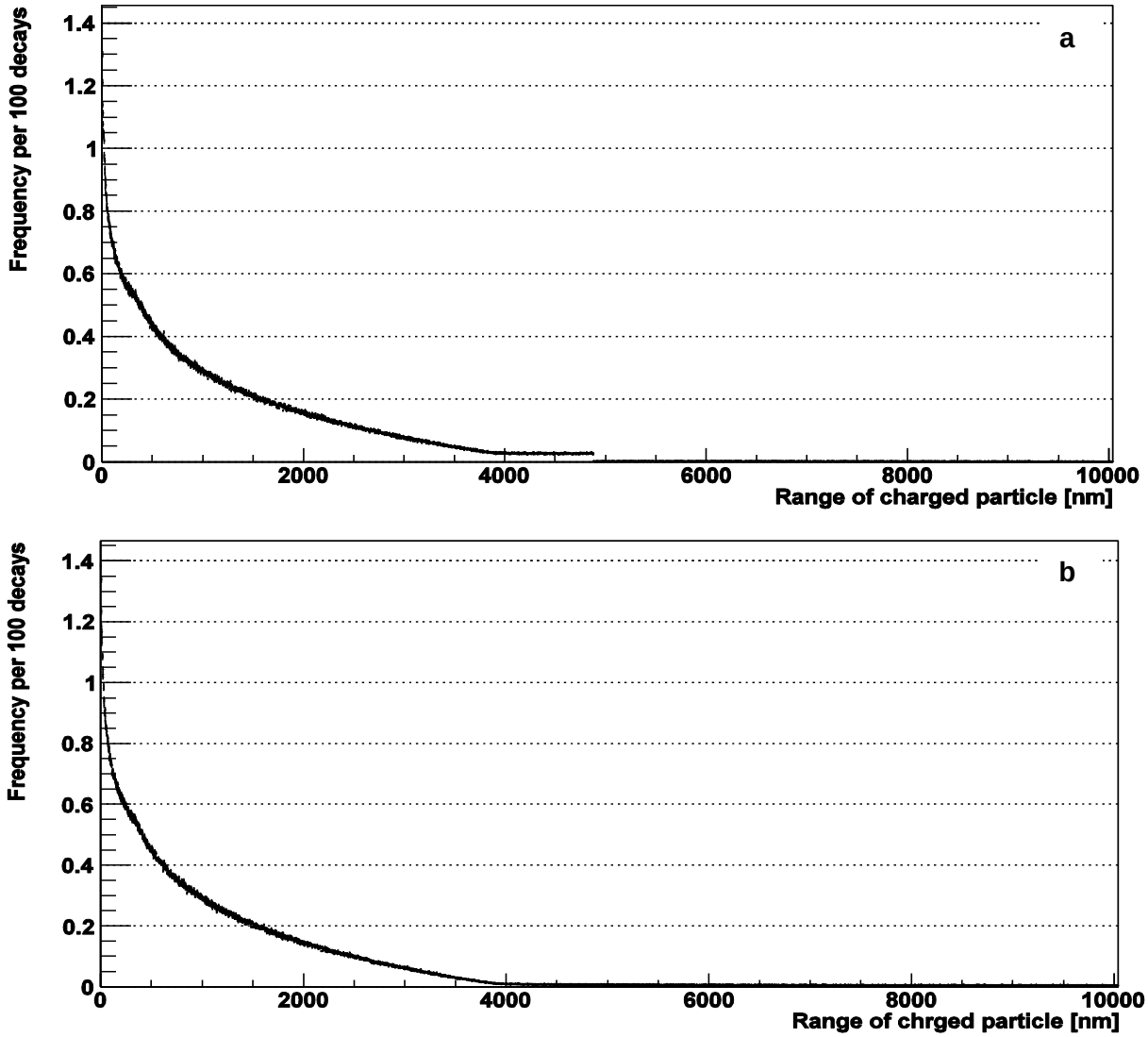

Figure 4.9. Projected range of charged particles emitted during the decay of ^{123}I, computed using the Livermore physics list. Figure (a) shows the results when the nuclear and cellular membranes are present and figure (b) shows the results when the membranes have been removed.

The previous conclusion that the majority of the low energy electrons will not have ranges exceeding the average ranges tabulated in Table 4.16 still holds: from Figure 4.9 and Figure 4.10 particles with ranges larger than 2.5 μm occurs less than 0.1% of the time. From Figure 4.9 however we see that 0.4 – 1.4 of every 100 decays produce particles with ranges less than 500 nm, and from Figure 4.10 we see these charged particles occur 0.3 – 1.0% of the time. We also see a discontinuity at 4.88 μm (where the cell membrane is) in Figure 4.9(a), which is not present in Figure 4.9(b) and Figure 4.10. The effects at thin surfaces may therefore be attributed to the model which approximates the scattering of charged particles used in the Livermore physics list. The membranes have a significant “restraining” effect on the charged particles when using Livermore, resulting in shortened ranges for lower energy charged particles and a higher absorbed dose (also seen in Table 4.16).

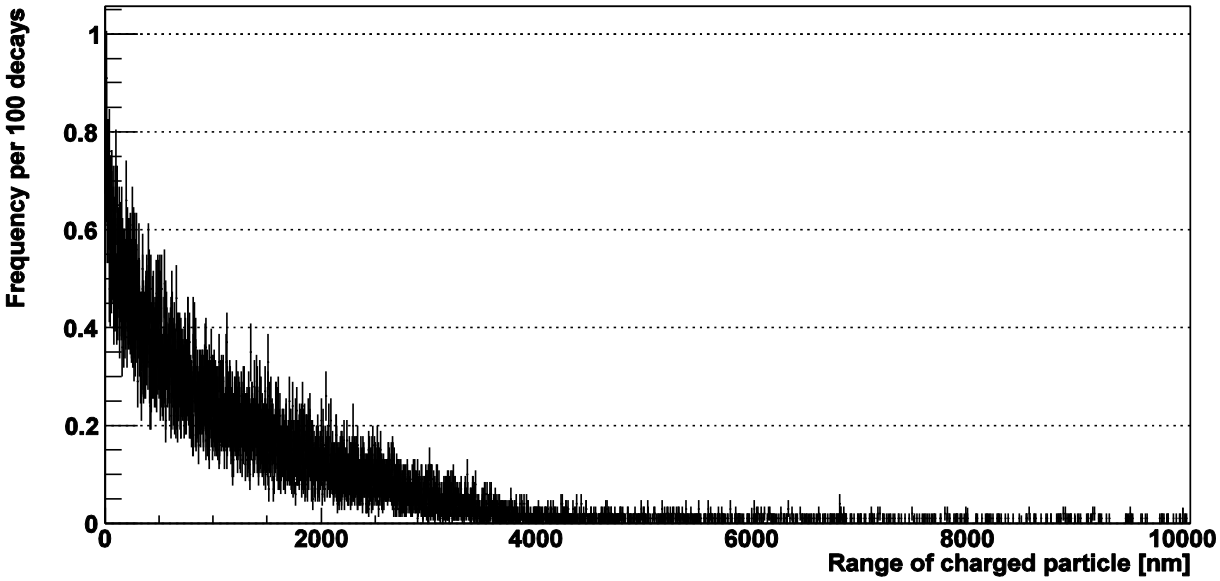

Figure 4.10. Projected range of charged particles emitted during the decay of ^{123}I, computed using the Geant4-DNA physics list.

Energy deposition along the radius

In the following computations, the Livermore Low Energy physics list was used to simulate the energy deposition in the cell and nucleus by particles produced by the decay of 10^6 ^{123}I-atoms, with r_{cell} = 4.88 µm and a 990 eV production cut value. Shown in Figure 4.11 is the average radial energy deposition per decay of an ^{123}I-atom located uniformly in the nucleus and in Figure 4.12 when it is located within the cytoplasm.

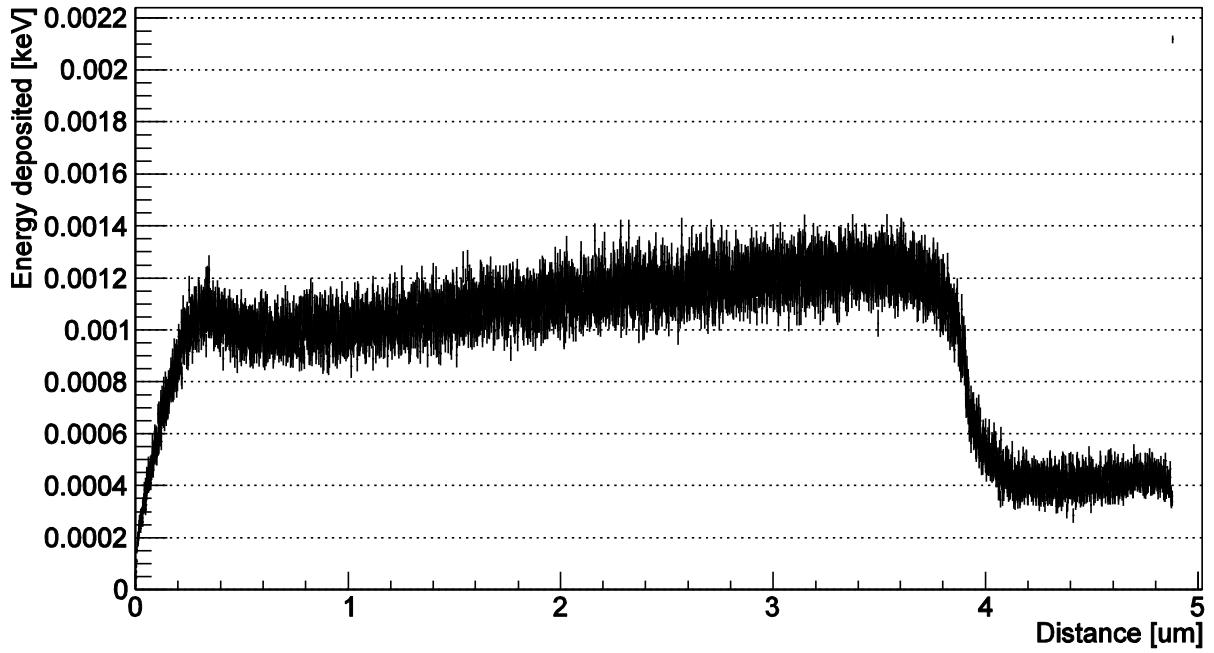

Figure 4.11. Total energy deposited (keV) along the radius (µm), per decay in the nucleus.

From Figure 4.11 we see an increase in deposited energy from the centre of the cell to a distance of approximately 0.3 μm.

Thereafter the energy deposited radially remains relatively constant throughout the nucleus of the cell. This can mostly be attributed to the fact that the ^{123}I atoms were randomly generated within the nucleus and so the low energy particle produced by the decay deposited their energy close to the decay site.

We see a sharp decline in the deposited energy as it reaches the nuclear membrane at about 3.9 μm, after which the energy deposited in the cytoplasm again remains relatively constant. The decrease is because no sources were generated past the nuclear membrane. The plateau past the nuclear membrane however, is probably due to the energy deposited by the internal conversion electrons and characteristic γ-rays and X-rays.

From Figure 4.12 we see that very little energy is deposited within the nucleus when the ^{123}I decays in the cytoplasm, as noted when comparing the values in Table 4.10.

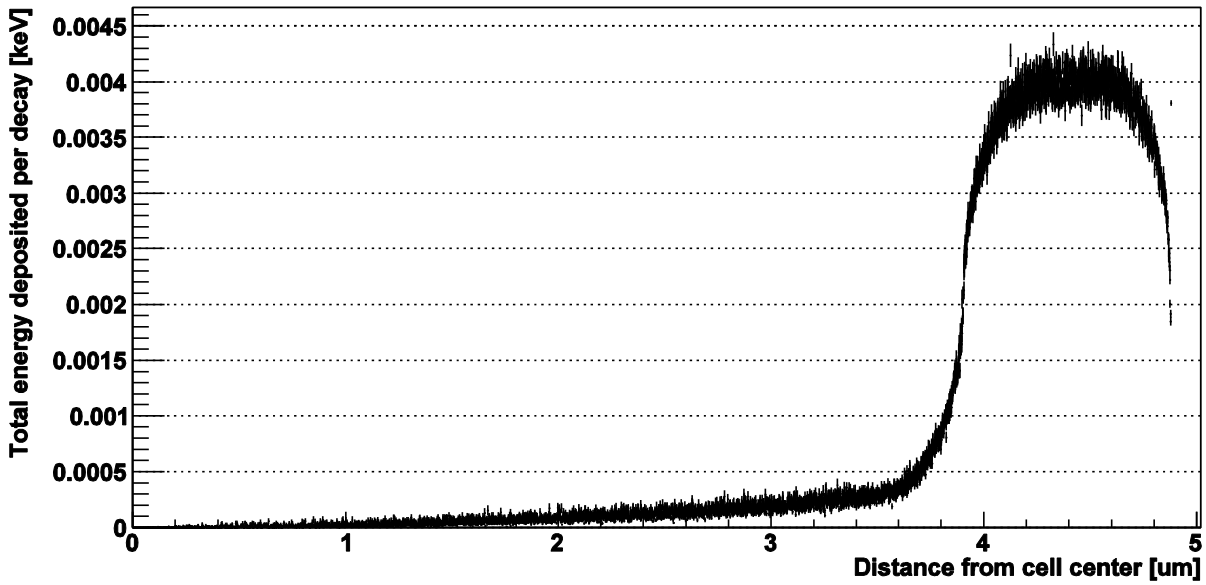

Figure 4.12. Total energy deposited (keV) along the radius (um), per decay in the cytoplasm.

Emission spectra

The number of electrons (internal conversion, Auger and Coster-Kronig) and the number of photons produced on average per decay of ^{123}I is approximately the same for both the Livermore and DNA physics lists, as shown in Table 4.16, with the corresponding frequency emission spectra (produced using the Livermore Physics list) shown in Figure 4.13 and Figure 4.14.

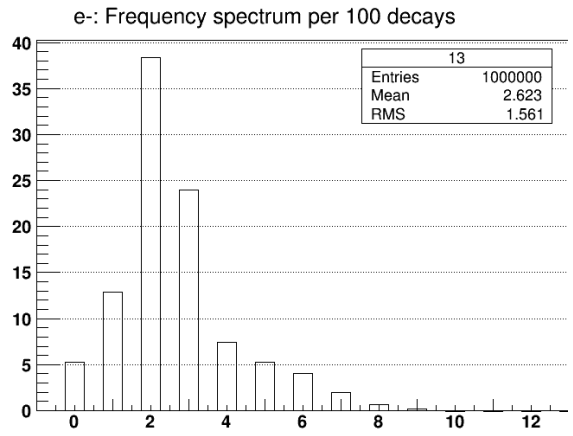

Figure 4.13. Electron emission frequency per 100 ^{123}I decays.

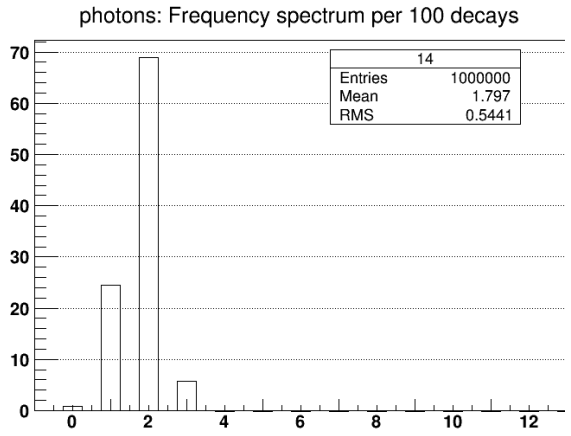

Figure 4.14. Gamma emission frequency per 100 ^{123}I decays.

We see from the above spectrum that approximately 2.6 ± 1.6 electrons (Auger, Coster-Kronig and internal conversion electrons) are emitted in the decay of ^{123}I to the ground state of the ^{123}Te daughter atom. Similarly we see approximately 1.8 ± 0.5 gammas are emitted in the decay of ^{123}I. The values of 3.05 electrons and 1.72 photons emitted on average per ^{123}I decay, estimated by the ICRP, are consistent with our ranges [51]. It is possible to exclude the electrons with energies of 127 keV (the characteristic IC electron) and above from the scoring procedure in order to obtain an estimate of the number of Auger and CK electrons, since the only electrons with energies above 127 keV are IC electrons which occur in 1.8% of the decays [24]. This exclusion was however not done in the current study.

The electron energy-emission spectrum and the gamma energy-emission spectrum generated by Geant4 for 10^6 decay of ^{123}I can be seen in Figure 4.15 and Figure 4.16 below.

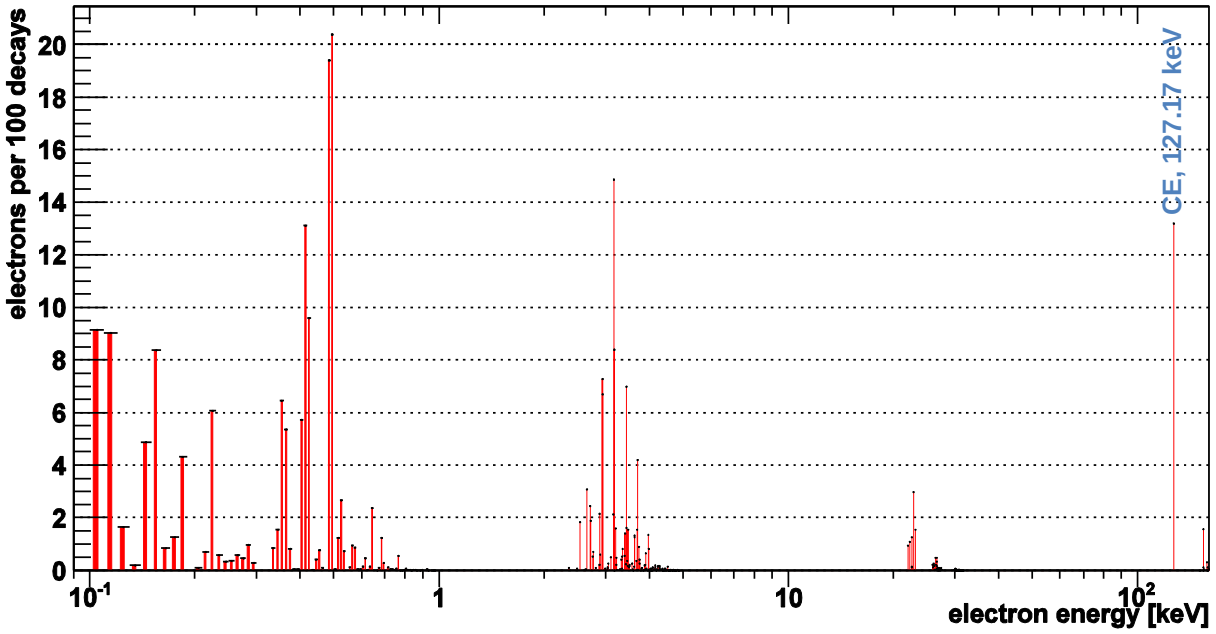

Figure 4.15. Electron energy spectrum associated with the decay of ^{123}I, produced by Geant4.

From the electron emission spectrum in Figure 4.15 we see the characteristic 127 keV internal conversion electron occurring approximately 13.2% of the time. A more enhanced electron energy spectrum can be seen in the Appendix C. We note that there are no electrons emitted in the decay of ^{123}I with energies less than 100 eV. This is because the photon and electron emission spectra of radioactive elements and de-exciting atoms are based on the Evaluated Nuclear Structure Data Files, as mentioned in Section 2.3.1, which do not include emission data below 100 eV. The ICRP similarly use these files for the reporting of their emission spectra.

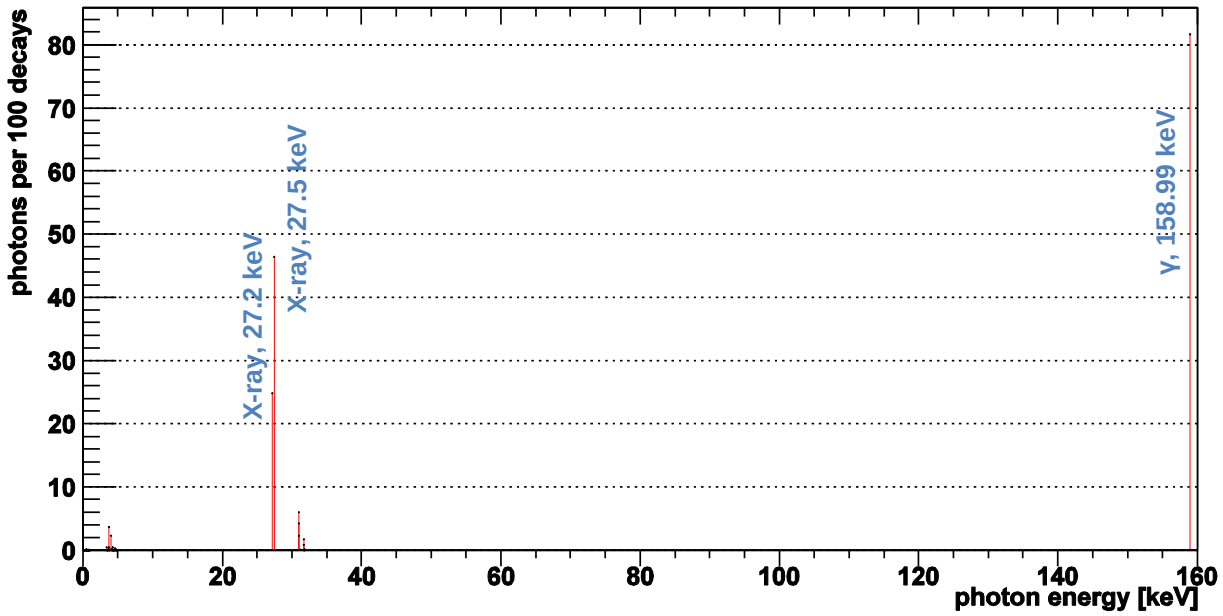

Figure 4.16. Photon energy spectrum associated with the decay of ^{123}I, produced by Geant4.

From the gamma emission spectrum, shown in Figure 4.16, we see that the characteristic 159 keV gamma occurs approximately 82% of the time, and the 27.2 keV and 27.5 keV X-rays occur respectively 25% and 46% of the time – in good agreement with the nuclear data sheets [24]. In Figure 4.17, the gamma emission spectrum of an ^{123}I sample measured using the NaI well-counter (see section 3.1.4) is shown. Present are the 27 keV and 159 keV energy peaks, but also the 186 keV (159 keV + 27 keV) sum peak, the 54 keV (27 keV + 27 keV) sum peak and the 159 keV Compton (scatter) edge (at 100 - 150 keV). The 159 keV peak together with the 186 keV sum peak were considered when determining the activity of a sample using the RB NaI well-counter.

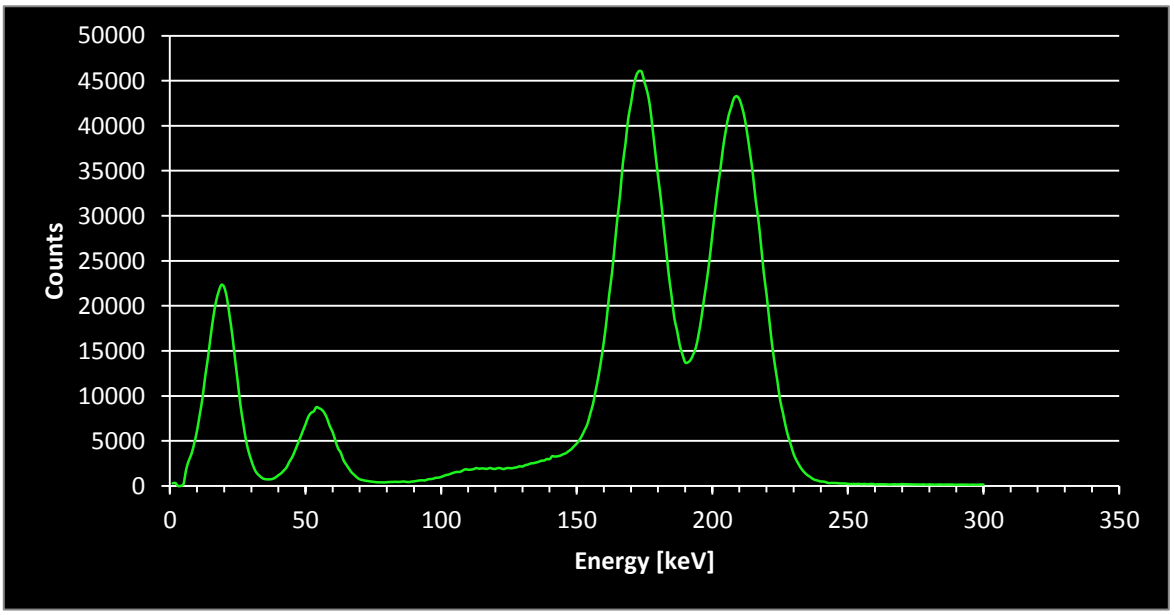

Figure 4.17. Gamma-ray spectrum measured with the NaI well-counter of a 750 nCi ^{123}I sample. The spectrum shown was acquired over a period of 60 seconds. The 27 keV X-ray peak, the 54 keV sum peak, the 159 keV γ-ray peak and its Compton scatter edge, and the 186 keV sum peak are clearly distinguishable on the spectrum.

Energy deposition spectra

The energy deposited within the cell by all the electrons per decay in the nucleus is shown in Figure 4.18, averaged over 10^6 simulated decays of ^{123}I using the Livermore Low Energy physics list with 990 eV production cuts.

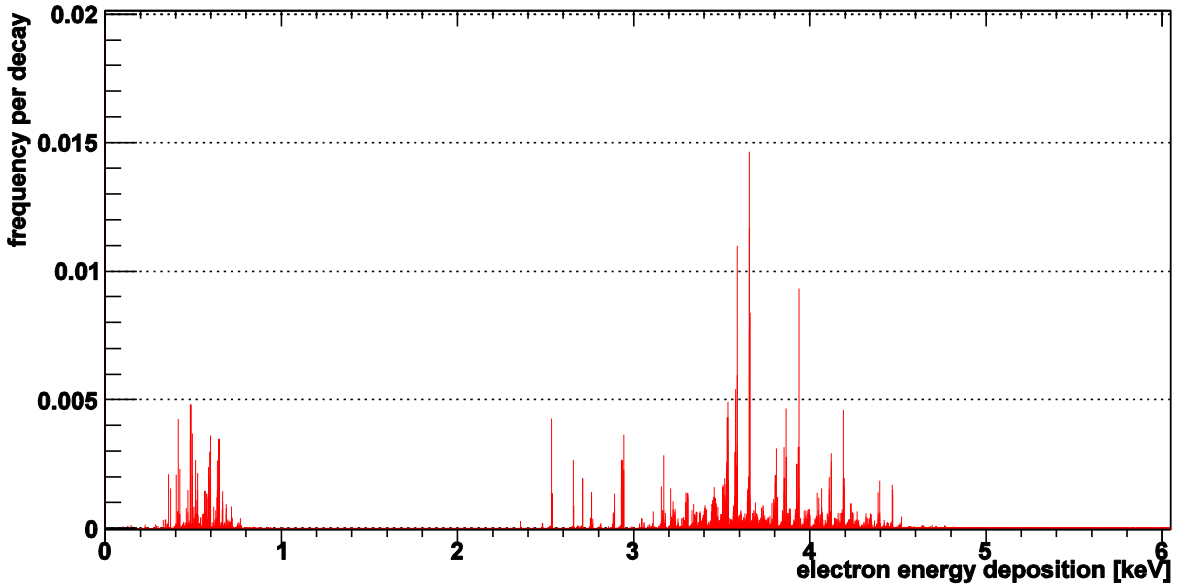

Figure 4.18. Energy deposited in the cell per decay by the electrons.

What is not seen in Figure 4.18 is that in slightly more than 5% of the decays no energy is deposited in the cell by the electrons, in other words no electrons were produced during these decays (as can be seen in Figure 4.13).

4.3. Calculation of the Relative Biological Effectiveness of ^{123}I

The conversion of incorporated activity to absorbed dose was done by assuming that 4.43 ± 0.38 keV was deposited in a cell with radius 4.88 ± 0.85 μm for each ^{123}I decay and following the calculations as described in Section 3.3.1. The resultant intracellular distributions of micronuclei in cytokinesis-blocked lymphocytes for donors 1 and 2 due to the exposure from incorporated ^{123}IUdR are given in Table 4.17 and Table 4.18 respectively. Reported in the tables is the accompanying binucleation index – the fraction of the scored cells which had 2 main nuclei.

Table 4.17. ^{123}I dose-response for lymphocyte donor 1.

	Micronuclei frequency per binucleated cell							
Dose [Gy] ± σ	*0*	*1*	*2*	*3*	*4*	*MNi/500BN*	*± σ (MNi/500BN)*	*BN index %*
0.000 ± 0.000	373	25	2	0	0	36	7	-
0.013 ± 0.001	115	7	0	0	1	45	14	-
0.033 ± 0.003	115	15	2	0	0	72	17	-
0.029 ± 0.003	134	23	1	0	0	79	16	10
0.062 ±0.005	97	31	9	3	0	207	27	17
0.363 ± 0.032	118	39	4	1	0	154	22	17
0.574 ± 0.050	15	13	2	0	0	283	69	4.5

The 0.062 – 0.574 Gy dose points were not considered in the fitting procedure, since they deviate from linearity (see discussion below).

Table 4.18. ^{123}I dose-response for lymphocyte donor 2.

	Micronuclei frequency per binucleated cell							
Dose [Gy] ± σ	*0*	*1*	*2*	*3*	*4*	*MNi/500BN*	*± σ (MNi/500BN)*	*BN index %*
0.000 ± 0.000	374	22	2	0	2	43	7	-
0.037 ± 0.003	208	16	0	0	1	44	10	-
0.023 ± 0.002	376	51	2	0	1	69	9	54
0.039 ± 0.003	344	58	3	0	1	84	10	46
0.132 ± 0.011	170	34	6	1	0	116	17	24
0.407 ± 0.035	72	20	3	0	0	137	27	23
0.658 ± 0.057	145	31	4	0	0	108	17	16

The 0.037 Gy (outlier), 0.407 Gy and 0.658 Gy dose points were not considered in the fitting procedure, since they deviate from linearity (see discussion below).

The background micronuclei (0.00 Gy) are subtracted from each dose point before the fit was applied. The resultant dose-response curves are shown in Figure 4.19. The coefficients of the fitted lines are given in Table 4.19.

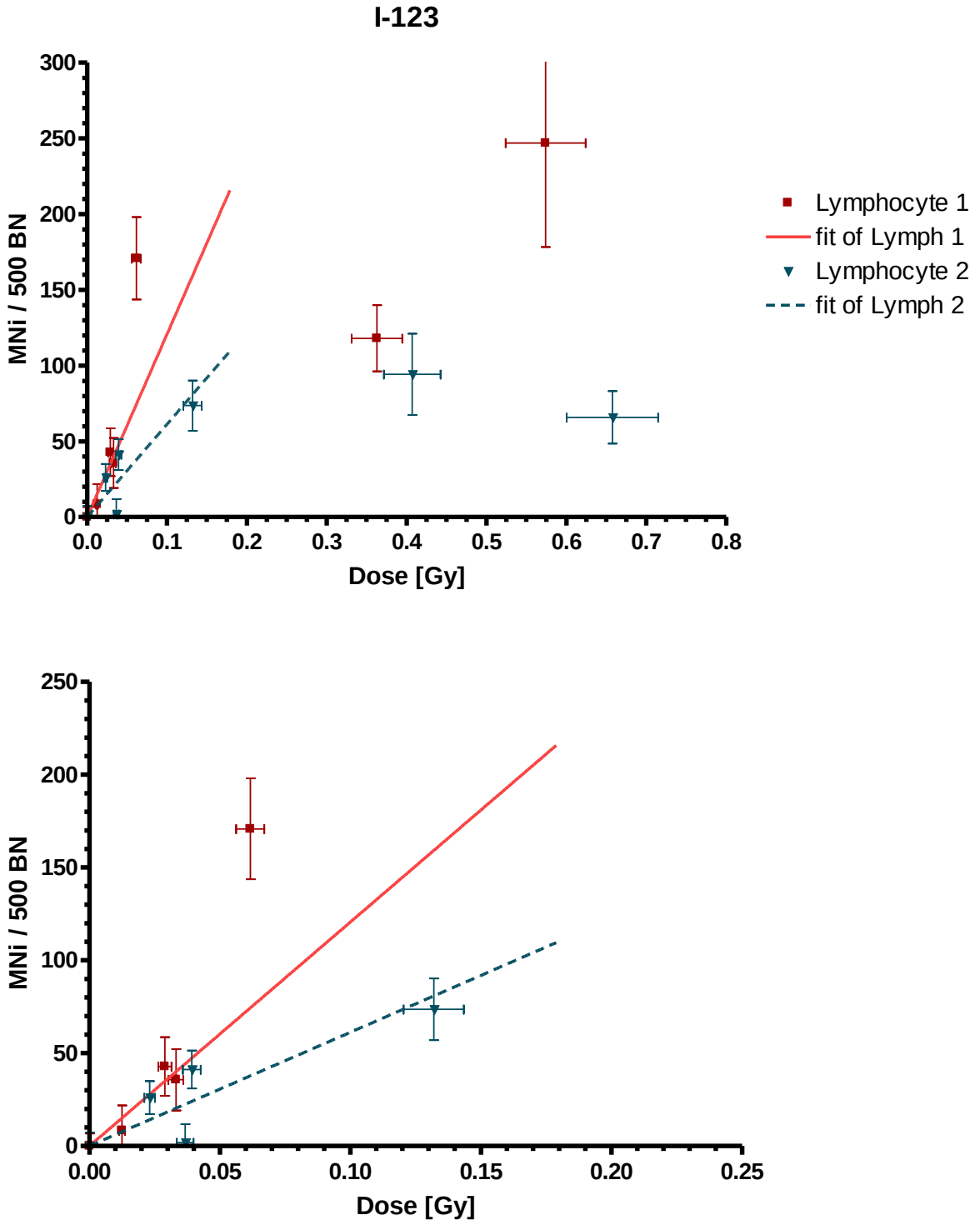

Figure 4.19. ^{123}I dose-response for lymphocytes. The bottom figure shows the enlarged 0.0 – 0.25 Gy dose region of the top figure.

As shown on Figure 4.19, a linear activity-response could be established for the first few points; the α-coefficients of the fitted lines are given in Table 4.19. The biological effectiveness of the ^{123}I irradiations are compared to the corresponding ^{60}Co exposure (Table 4.5) for each of the dose points and the RBEs are calculated as described in Section 3.3.1 using equation (3.13); and the RBE_M are calculated using equation (3.14).

Table 4.19. ^{123}I dose - response coefficients of the linear fits to the MNi / 500 BN cells for the lymphocyte samples.

Cell line	*α (Gy^{-1})*	*R^2*
Lymphocyte 1	1207 ± 141	0.90
Lymphocyte 2	613 ± 92	0.83

The linear dose response is indicative of the high-LET nature of the Auger electrons if emitted close to cellular DNA [13]. The RBEs determined from the dose points of lymphocyte donor 1 in the linear region range from 19 ± 10 to 32 ± 7; and those of lymphocyte donor 2 range from 15 ± 6 to 42 ± 11. The dose limiting RBE_M for lymphocyte donor 1 and 2 are respectively 34 ± 8 and 50 ± 15, calculated using their respective ^{60}Co dose-response curves.

Using the general lymphocyte dose-response to ^{60}Co determined by Willems *et al*. (given in Table 4.5), the RBE_M for lymphocyte donor 1 is 61 ± 7 and for lymphocyte donor 2 is 31 ± 5.

We have noted (section 4.1.3.1) that the ^{60}Co γ-ray dose-response curves of the studied lymphocyte samples compare well with that found in literature. The variation of the RBE values between the two lymphocyte donors is therefore due to the different responses to the high-LET Auger electron exposures. Similar to the ^{60}Co-exposure, a significant variation in the biological response can be noted for the two lymphocyte donors when exposed to ^{123}I (by a factor of 2.0). Studies have reported a reduction in the variation of inter-donor radiosensitivities of T-lymphocytes for other forms of high-LET radiation like fast neutrons and α-particles when compared to low-LET radiation like ^{60}Co γ-rays [87], [28], [32]. This effect was also seen in the current study (reducing from 2.9 to 2.0).

Slabbert *et al*. showed that the dose limiting RBE_M of high-LET particles (neutrons in this case) decreases as the radiosensitivity to ^{60}Co γ-rays increases [87]. Therefore, since lymphocyte donor 1 is more radiosensitive than donor 2, its RBE_M should be smaller than that of donor 2. This response was also seen in the current study, except when using the general ^{60}Co dose-response by Willems *et al.* This is because the general dose-response does not accurately reflect the high radiosensitivity of lymphocyte donor 1 and the low radiosensitivity of donor 2 to ^{60}Co γ-rays.

Various studies on rodent cell lines (e.g. V79 cells, mouse testis and CHO cells) reported an increase of biological effectiveness by a factor of 7–12 for ^{125}I (assumed in the literature to have the same biological effectiveness as ^{123}I) if the radionuclide is incorporated into DNA following administration as ^{125}IUdR when compared to kilo voltage X-rays [3], [68], [69], [71], [72], [73]. For Auger emitters bound to DNA, a radiation weighting factor w_R of 20 has been proposed by the ICRP, which is meant to represent the biological effect of the ionizing radiation [35], [36], [69]. The current calculated RBE values, which are resultant from the

fitted dose-response curves, are significantly larger than the RBE values reported in literature. More data points in the linear dose-response region are needed to improve the estimation of the dose-response for lymphocytes exposed to ^{123}IUdR.

Shown in Figure 4.20 are the RBE values in the linear dose-response regions for the two donors due to the dose from the ^{60}Co and ^{123}I exposures which produced those respective biological responses.

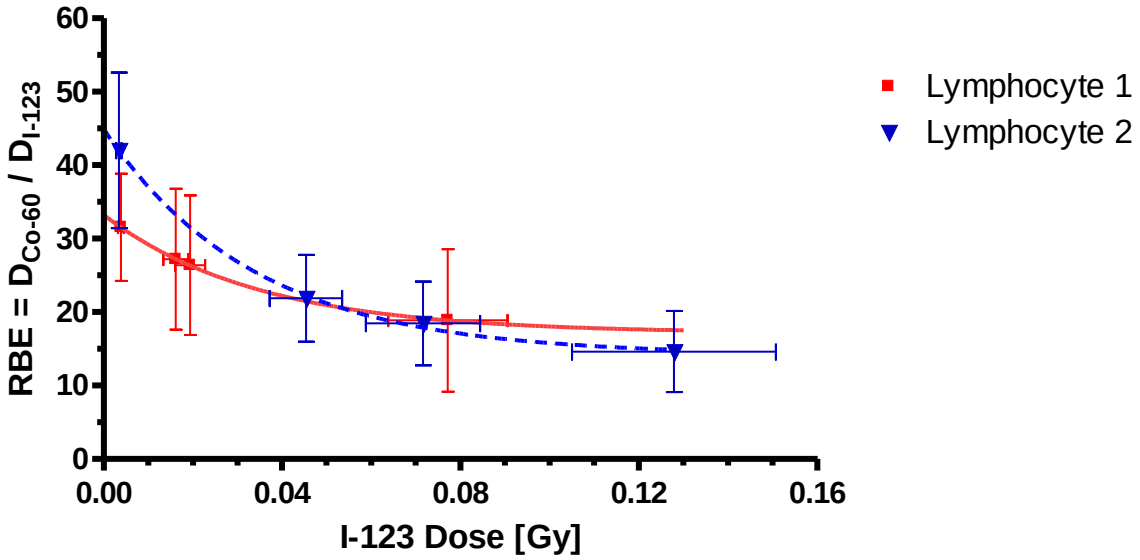

Figure 4.20. RBE of the data points in the linear region of the ^{123}I dose-response curves.

A clear exponential decay trend can be seen for both lymphocyte donors. The fitted curves are described by the equation:

$$RBE = S \cdot e^{-K \cdot D\,[Gy]} + p \tag{4.6}$$

The respective coefficients are given in Table 4.20. We see that as the ^{123}I dose increases, the radiobiological effectiveness tends towards a value of between 14 and 17, very close the radiation weighting factor of 20 recommended by the ICRP.

Table 4.20. Coefficients of the RBE-dose curves for the two lymphocyte donors.

	$S \pm \sigma$	$K \pm \sigma$ [Gy^{-1}]	$p \pm \sigma$
Lymphocyte 1	16.1 ± 0.1	28.8 ± 0.6	17.1 ± 0.1
Lymphocyte 2	30.8 ± 1.1	29.5 ± 3.2	14.2 ± 0.9

We now consider the influence of the S-phase fraction on the activity-dose conversion calculations. Only cells which were entering (or were already in) S-phase at the time the ^{123}IUdR was introduced would be the cells which incorporated the ^{123}I into their DNA. It is these cells which ultimately express the radiation induced damage. This drastically reduces the number of cells (thus far assumed to be 2.5×10^6) which the cumulative energy could have been deposited into, as calculated via equation (3.12).

Figure 4.21 shows the resultant dose-response curves for the linear region of the ^{123}I exposures as well as the ^{60}Co dose-response curves for both lymphocyte donors once the S-phase fraction (section 4.1.4) is included in the dosimetry calculations. The coefficients of the fitted lines are given in Table 4.21, with the same dose points being omitted from the fits as discussed above.

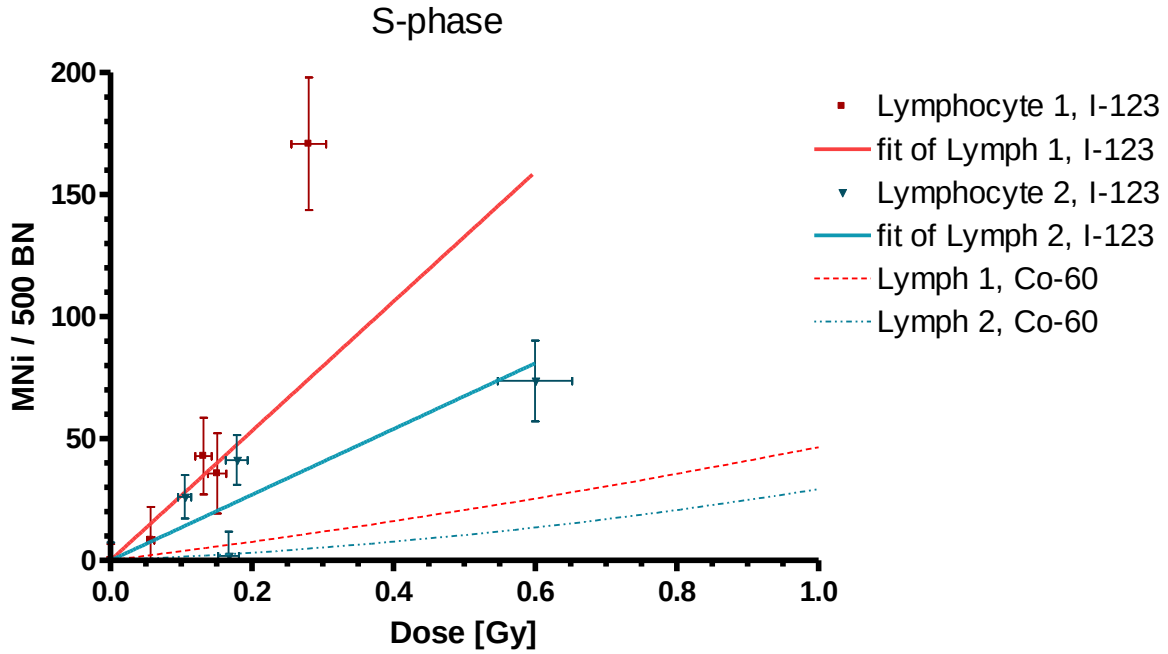

Figure 4.21. S-phase dose-response for lymphocytes exposed to ^{123}I and ^{60}Co.

Table 4.21. ^{123}I dose - response coefficients of the linear fits to the MNi / 500 BN cells for the lymphocytes considering S-phase fractions.

Cell line	α (Gy^{-1})	R^2
Lymphocyte 1	266 ± 31	0.90
Lymphocyte 2	135 ± 20	0.83

The RBEs for each dose point as well as the RBE_Ms are calculated as described previously for both lymphocyte donors with the consideration of S-phase fractions. The RBEs calculated for the dose points of lymphocyte donor 1 in the linear region range from 4 ± 2 to 7 ± 2; and those of lymphocyte donor 2 range from 3 ± 1 to 9 ± 2. The RBE_M for lymphocyte donor 1 and 2 are respectively 7 ± 2 and 11 ± 3, calculated using their respective ^{60}Co dose-response curves.

Using the general lymphocyte dose-response to ^{60}Co determined by Willems *et al*. (given in Table 4.5), the RBE_M for lymphocyte donor 1 is 14 ± 2 and for lymphocyte donor 2 is 7 ± 1.

The inclusion of the S-phase fraction, compared to when it is not considered, reduces the calculated RBEs significantly.

Chapter 5: Conclusions

5.1. Radiobiology

The dose rate of the ^{60}Co-teletherapy unit at iThemba LABS was investigated. The experimentally measured value is compared to that from theoretical predictions. Three cell lines were exposed to γ-rays from this therapy unit and the cytokinesis-blocked micronucleus assay was used to determine the radiation induced damage to the cells. We investigated the S-phase fraction of stimulated human T-lymphocytes using BrdU and also determined the diameter of these lymphocytes in culture. Finally, T-lymphocytes of two male donors were exposed to 5-[^{123}I]-iodo-2-deoxyuridine (^{123}IUdR) in order to investigate the induced damage by mainly the Auger electrons emitted during the decay of ^{123}I.

On 5 June 2013, the ^{60}Co-unit had an activity of 48.4 TBq which yielded a dose rate of 8.16 mGy/s, for the geometrical setup as described in section 3.1.1. The dose rate predicted from theory is 12% lower than the measured value. The calculations using equation (3.2) do not take into account the energy deposition due to backscatter, nor from increased dose deposition due to the build-up material.

Rat brain endothelial cells, Chinese hamster ovary (CHO) cells and human T-lymphocytes were exposed to graded doses of ^{60}Co γ-rays. A linear-quadratic dose-response was found for all three cell lines, as is well documented for low-LET radiation like the ^{60}Co γ-rays. It was seen that the linear-quadratic dose-response for our two lymphocyte donors was similar to that of Willems *et al*. and Slabbert *et al*. studying micronuclei inductions in stimulated human lymphocytes exposed to ^{60}Co γ-radiation [34], [87]. From the dose-response curves, a difference in radiosensitivity was seen between each of the cell lines, with the lymphocytes being more radioresistant than the CHO cell, as noted by Slabbert *et al*. [13]. An inter-donor variability in the dose-response of the two lymphocyte donors was observed (a factor of 2.9). Willems *et al.* also noted this for stimulated human lymphocytes exposed to ^{60}Co γ-radiation.

The average cell diameter and resulting cell radius of isolated and stimulated lymphocytes was found to be 9.76 ± 1.69 μm and 4.88 ± 0.85 μm respectively. Using BrdU, it was found that only 22.0% of the seeded 2.5 × 10^6 lymphocytes were in S-phase 44 hours post culture start-up. This gives an indication of which fraction of the stimulated lymphocytes will incorporate the ^{123}IUdR.

5-[^{123}I]-iodo-2-deoxyuridine was used to incorporate the Auger emitter into the nuclear DNA of human T-lymphocytes from two male donors. The cytokinesis-blocked micronucleus assay was used to determine the radiation induced damage to the cells. A linear activity-response was observed for both the donors, with some deviations from linearity occurring at higher activity points.

The low S-phase fraction strongly points to the fact that significant amounts of ^{123}IUdR remain unincorporated and is likely to be present in the medium surrounding the cells. It was noted that many cells were lost during the washing procedures. In future, new washing procedures should be investigated or adapted to reduce this reduction in cells as well as reduce the amount of activity in the surrounding medium, and more samples and slides should be scored to reduce the statistical uncertainty in the observed biological responses and to obtain a better linear fit.

5.2. Monte Carlo simulations

We simulated the ^{60}Co-teletherapy unit to determine the associated dose rate of this unit by making use of the Geant4 Monte Carlo toolkit. Furthermore, Geant4 was used to investigate the energy deposition due to the decay of ^{123}I in, amongst others, a sphere representing a T-lymphocyte.

On the day of measurement the ^{60}Co-unit had a dose rate of 8.16 mGy/s. The Geant4 ^{60}Co-simulations produced results which deviate by less than 2% from the measured value. It was concluded that either physical dose rate measurements or detailed simulations should be done when estimating the dose rate from such a source.

It was concluded in the present study that only simulations where the ^{123}I is generated within the nucleus need be considered for dosimetry of ^{123}IUdR. This conclusion is based on findings by Kassis, Makrigiorgos, Humm and Slabbert *et al*. ([57], [63], [76], [13]) and results drawn from Table 4.10, Figure 4.11 and Figure 4.12.

The energy deposited within the entire cell by all particles should be considered, since the mass of the entire cell is known with some certainty but that of the nucleus is not; and some energy deposition by higher energy particles (e.g. internal conversion electrons, X-rays and γ-rays) occurs in the cytoplasm as well. Humm *et al*. also highlighted the fact that the absorbed dose to the cell nucleus alone is insufficient to predict the biological effect of an Auger electron emitter localized in the cell nucleus and that the dose to the entire cell volume should be considered [57].

It was decided that the energy estimations using the Geant4-DNA physics list should be used in the dosimetry calculations, since fewer approximations are made during the simulation about the trajectory and interactions of a particle during its track. It was found that 4.43 ± 0.38 keV was deposited in a sphere of unit density water for each ^{123}I decay in the nucleus (r_{cell} = 4.88 μm, r_{nucl} = 0.8× r_{cell}). The influence of the size of the cell nucleus on the energy absorbed in the entire cell was investigated and it was found that a 30% reduction in nucleus size leads to only a 1.5% increase in the energy deposition in the entire cell.

The emission spectra of radionuclides selectable in Geant4 are dependent on and limited by the data available in the Evaluated Nuclear Structure Data Files [11]. The energy and frequency emission spectra for electrons and photons produced by Geant4 during the decay of ^{123}I were found to be similar to those reported by the ICRP as expected, since the ICRP also makes use of the ENSDF [51]. It is possible to use a custom emission spectrum for a radionuclide. This procedure however increases the complexity of the code and most of the electron emission probabilities are theoretically determined and may not be considered correct or reliable by many [4], [51], [55], [56], [50], [11].

The simulation of the energy deposition of particles moving through matter using a Monte Carlo method is highly subjective and reliant on many variables and approximations. The uncertainties associated with dosimetry due to modelling are aptly described by the following extract:

"*Differences in: (i) The cross-section models used for describing the interactions of electrons with water, which is the medium used to approximate the cellular milieu, (ii) the algorithm used to simulate electron transport, and (iii) the employed electron emission spectrum, can lead to sizeable differences in the dosimetry*" – Bousis, Emfietzoglou and Nikjoo (2012, [60])

5.3. The Relative Biological Effectiveness (RBE) of ^{123}I

The dose absorbed in a cell due to the decay of ^{123}I, determined by using Geant4, was used to compare the radiobiological effectiveness of the DNA-incorporated Auger emitter ^{123}I and ^{60}Co γ-rays on isolated and stimulated human T-lymphocytes from two donors.

The conversion of incorporated activity to absorbed dose was done by assuming that 4.43 ± 0.38 keV was deposited in a cell with radius 4.88 ± 0.85 μm for each ^{123}I decay in the nucleus. A linear ^{132}I dose-response was established for both donors, with some deviations from linearity noted at higher dose points.

The RBEs determined from the dose points of lymphocyte donor 1 in the linear dose-response region ranges from 19 ± 10 to 32 ± 7, and those of donor 2 ranges from 15 ± 6 to 42 ± 11. The dose limiting RBE_M for lymphocyte donor 1 and 2 are respectively 34 ± 8 and 50 ± 15.

We have noted that the linear-quadratic ^{60}Co γ-ray dose-response curves of the studied lymphocyte samples compare well with that of literature. The variation of the RBE values between the two lymphocyte donors is therefore due to the different inherent responses to the high-LET Auger electron exposures. A reduction in the inter-donor radiosensitivity variation was seen (from a factor of 2.9 for ^{60}Co γ-rays to 2.0 for ^{123}I), similar to results found in other studies of high-LET radiations with T-lymphocytes [87], [28], [32]. It was found that the RBE_M of the less radiosensitive lymphocyte donor was larger than that of the more radiosensitive donor. This effect was also shown by Slabbert *et al.* working with high-LET neutrons and human lymphocytes [87].

The inclusion of the S-phase fraction of the lymphocytes in the dosimetry calculations was also considered. The resultant RBEs determined from dose points of lymphocyte donor 1 in the linear region range from 4 ± 2 to 7 ± 2, and those of lymphocyte donor 2 range from 3 ± 1 to 9 ± 2. The RBE_M for lymphocyte donor 1 and 2 are respectively 7 ± 2 and 11 ± 3. The inclusion of the S-phase fraction reduces the calculated RBEs significantly (compared to when it is not considered) and produce RBE values which relate well to those reported in literature [3], [68], [69], [71], [72], [73].

There is a clear increase in the biological response for the lymphocytes exposed to DNA-incorporated ^{123}I when compared to ^{60}Co γ-rays. This increase, along with the linear dose-response relationship, indicates the high-LET nature of the Auger electrons if they allowed to deposit their energy close to cellular DNA, which has also been noted for other cell lines when exposed to DNA-incorporated Auger emitters [57], [63], [76].

More biological data points in the linear region are needed to improve the estimation of the dose-response for lymphocytes exposed to ^{123}IUdR. A glaring lack of microdosimetric studies and associated literature with regards to human lymphocytes exposed to DNA incorporated Auger emitters, as well as their effectiveness relative to ^{60}Co γ-radiation, is apparent.

5.4. Overview & Outlook

The effectiveness of the DNA-incorporated Auger emitter ^{123}I to produce micronuclei in human T-lymphocytes relative to that of ^{60}Co γ-radiation was investigated. Studies of DNA-incorporated Auger emitters in human lymphocytes and the comparison to ^{60}Co γ-rays have not yet been reported in literature.

We investigated and demonstrated the feasibility of using Geant4 for the quantification and assessment of cellular dosimetry and the comparison of the biological effectiveness for different radiation qualities. This was similarly attempted by Freudenberg *et al*. (2011) [5]. The estimation of the energy deposition inside any cell line due to the decay of ^{123}I when using the Geant4 Monte Carlo code has not yet been reported on in literature.

Future studies may include ways to refine the estimation of energy deposition in cells due to the decay of an Auger electron emitter, and ways to more accurately measure and estimate the incorporated activity in cells. There is significant scope for further studies of DNA-incorporated ^{123}I in lymphocytes, using a larger group of donors, and other eukaryotic cell lines.

Appendix A - The decay level scheme of ^{123}I

The decay level scheme of ^{123}I obtained from the nuclear data sheets [24], compiled by the *Laboratiore National Henri Becquerel* [Accessed 22 May 2014] (online): http://www.nucleide.org/DDEP_WG/DDEPdata.html

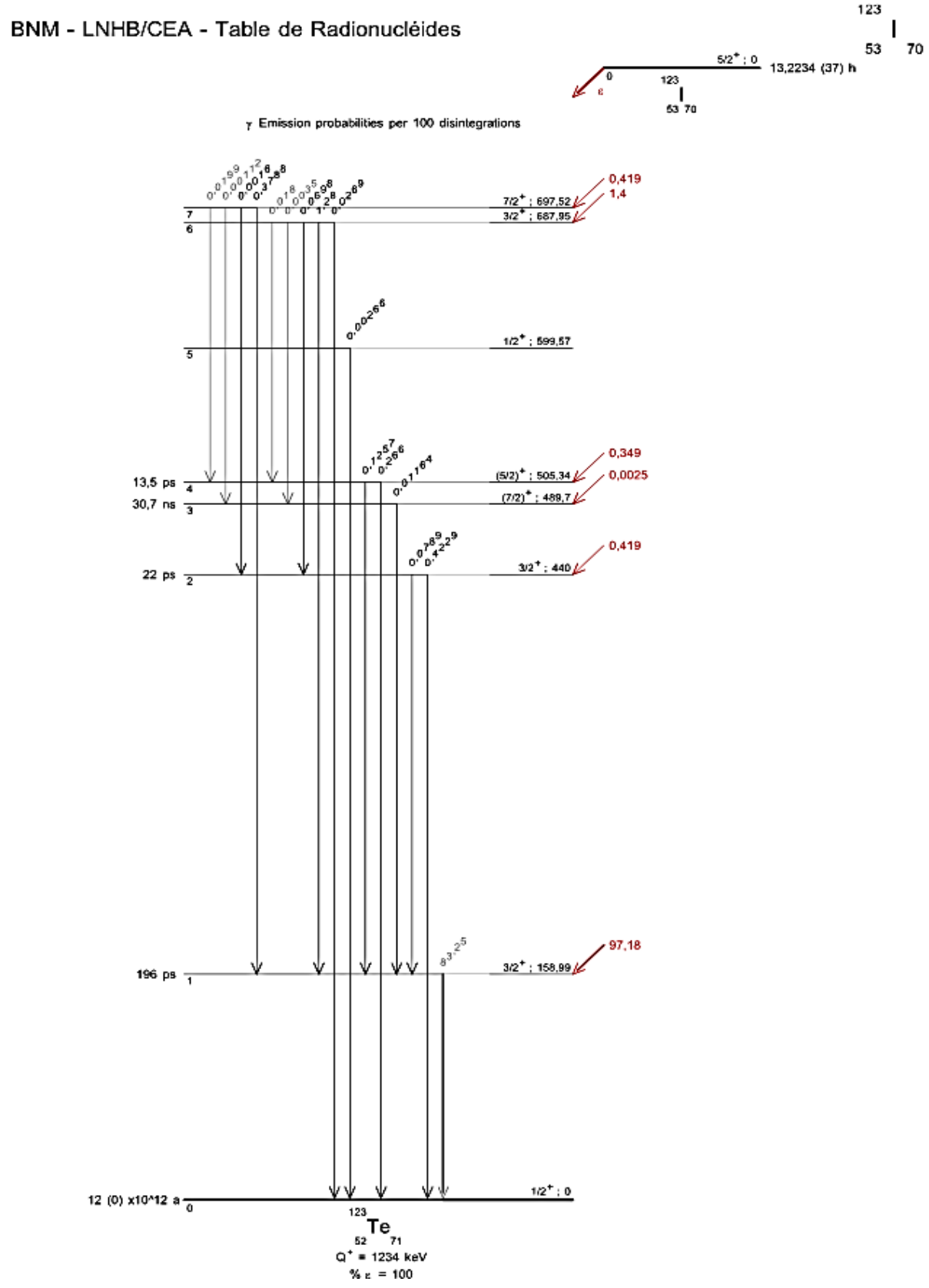

Table 5.1. Summary of the energies of the particles emitted during the decay of ^{123}I [24].

	Energy range (keV)
X-ray emissions	3.34 – 31.81
Gamma emissions	158.97 – 1068.12
Auger electron emissions	2.3 – 31.81
Conversion electron emissions	127.18 – 154.65

Appendix B - The synthesis and labeling of ^{123}IUdR

Description of the synthesis and labeling of the 5-[^{123}I]-iodo-2-deoxyuridine:

The labeling of ^{123}I radionuclide to the precursor 5-trimethylstannyl-2-deoxyuridine (TMS-UdR) was done by Dr Niel Rossouw, a radiochemist at iThemba LABS, following an ion exchange reaction method. This was done by adding a 0.1 M PBS solution (pH 7.4, 35 µℓ), a Na[^{123}I] solution (2-3 µℓ), a solution of TMS-UdR (20 µg) in ethanol (2 µℓ), and a solution of chloramine-T trihydrate (50 µg) in water (2 µℓ). The components were mixed for 10-15 min after which a solution of $Na_2S_2O_5$ (30 µg) in water (3 µl) was added. The mixture was then injected into a high-pressure liquid chromatography column and the pure product fraction of 5-[^{123}I]-iodo-2-deoxyuridine was collected between 23 and 24 minutes. This was diluted to the required activity using RPMI growth medium and added to cell cultures.

Appendix C - The extended electron energy spectrum of ^{123}I

The extended electron energy spectrum produced by Geant4 for the decay of ^{123}I:

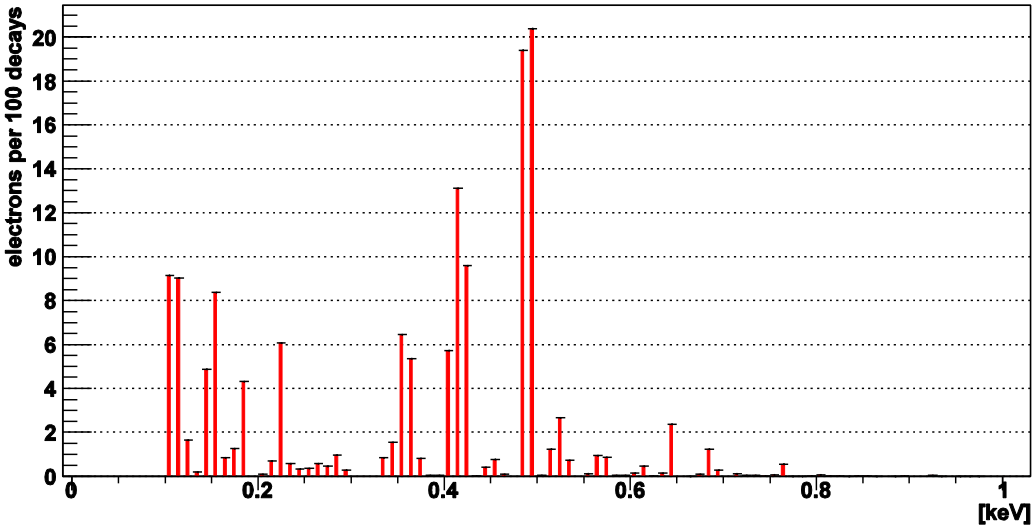

Figure 5.1. Electron energy spectrum 0.1 keV to 1 keV.

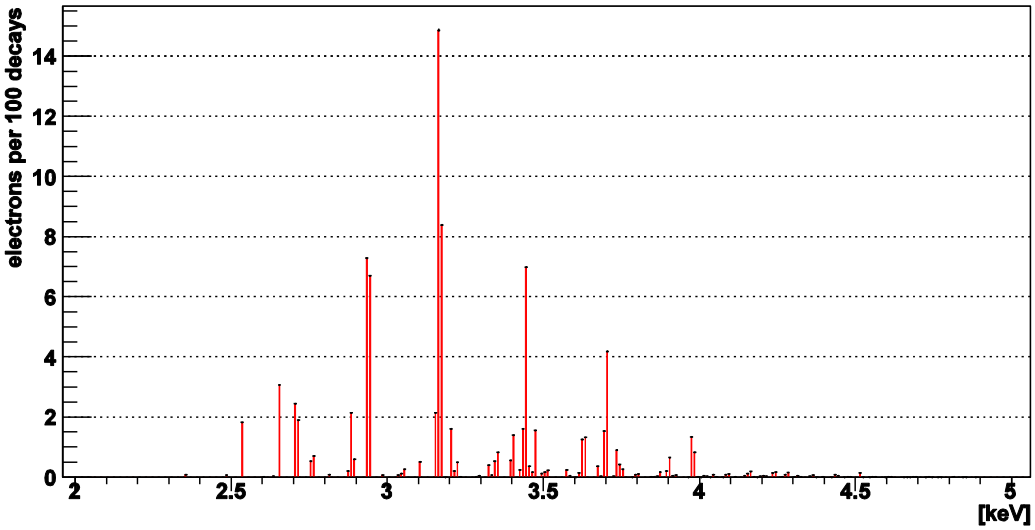

Figure 5.2. Electron energy spectrum 2 to 5 keV.

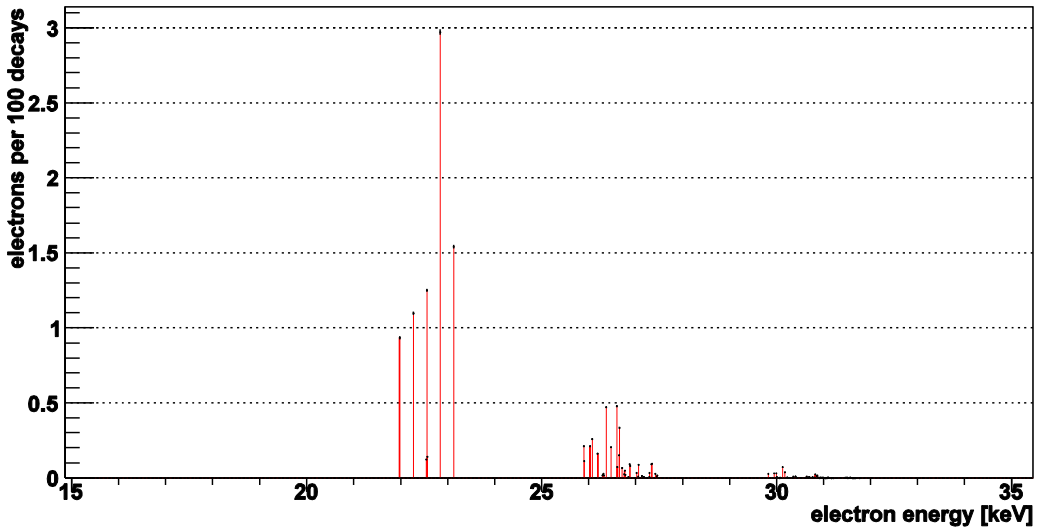

Figure 5.3. Electron energy spectrum 15 to 35 keV.

References

[1] J Stepanek, B Larsson, and R Weinreich, "Auger-electron Spectra of Radionuclides for Therapy and Diagnostics," *Acta Oncologica*, vol. 35, no. 7, pp. 863-868, 1996.

[2] S R Cherry, J A Sorenson, and M E Phelps, *Physics in Nuclear Medicine*, 3rd ed. Philadelphia: Saunders/Elsevier Science, 2003.

[3] A I Kassis, G M Makrigiorgos, and S J Adelstein, "Implications of Radiobiological and Dosimetric studies of DNA-incorporated I-123: The use of the Auger effect as a biological probe at the nanometre level," *Radiation Protection Dosimetry*, vol. 31, no. 1/4, pp. 333 - 338, 1990.

[4] R W Howell, "Radiation spectra for Auger-electron emitting radionuclides: Report No. 2," American Association of Physicists in Medicine, Report No. 2 of AAPM Nuclear Medicine Task Group No. 6. Medical Physics 1992.

[5] R Freudenberg, M Wendisch, and J Kotzerke, "Geant4-Simulations for cellular dosimetry in nuclear medicine," *Z. Med. Phys.*, vol. 21, pp. 281-289, 2011.

[6] S Ftacnikova and R Bohm, "Monte Carlo calculations of energy deposition on cellular, multi-cellular and organ level for Auger emitters," *Radiation Protection Dosimetry*, vol. 2, no. 4, pp. 279-288, 2009.

[7] E Pomplun, "Auger Electron Spectra: The Basic Data for Understanding the Auger Effect," *Acta Oncologica*, vol. 39, no. 6, pp. 673 - 679, 2000.

[8] D Bingham, I Gardin, and K P Hoyes, "The problem of Auger emitters for radiological protection," *Radiation Protection Dosimetry*, vol. 92, no. 1-3, pp. 219-228, 2000.

[9] S Agostinelli et al., "Geant4 - a simulation toolkit," *Nuclear Instruments and Methods in Physics Research Section A.*, vol. 506, no. 3, pp. 250 - 303, 2003.

[10] Geant4. [Online]. www.geant4.org

[11] Geant4 Collaboration, Physics Reference Manual, 2012, Version 9.6.0.

[12] Geant4 Collaborators. (2005, December) Introduction to Geant4. [Online]. http://geant4.web.cern.ch/geant4/G4UsersDocuments/Welcome

[13] J P Slabbert, J H Langenhoven, and B S Smit, "Synthesis of [I-123]-iodoantipyrine to study the high-LET characteristics of Auger electrons in mammalian cells," *Journal of Radioanalytical and Nuclear Chemistry*, vol. 240, no. 2, pp. 505 - 508, 1998.

[14] C Bousis, D Emfietzoglou, and H Nikjoo, "Monte Carlo single-cell dosimetry of I-131, I-125 and I-123 for targeted radioimmunotherapy of B-cell lymphoma," *International Journal of Radiation Biology*, vol. 88, no. 12, pp. 908 - 915, Decmber 2012.

[15] G Raisali, L Mirzakhanian, S F Masoudi, and F Semsarha, "Calculation of DNA strand breaks due

to direct and indirect effects of Auger electrons from incorporated I-123 and I-125 radionuclides using the Geant4 computer code," *International Journal of Biology*, vol. 89, no. 1, pp. 57 - 64, 2013.

[16] H Nikjoo et al., "Modelling of Auger-induced DNA damage by incorporated I-125," *Acta Oncologica*, vol. 35, no. 7, pp. 849 - 856, 1996.

[17] C Villigrasa, Z Francis, and S Incerti, "Physical models implemented in the Geant4-DNA extension of the Geant4 toolkit for calculating initial radiation damage at the molecular level," *Radiation Protection Dosimetry*, vol. 143, no. 2 - 4, pp. 214 - 218, 2011.

[18] International Atomic Energy Agency, *Radiation oncology physics : a handbook for teachers and students*, E B Podgorsak, Ed. Vienna, Austria: International Atomic Energy Agency, 2005.

[19] D H Boal, *Mechanics of the cell*, 2nd ed. New York, United States of America: Cambridge University Press, 2012.

[20] International Atomic Energy Agency, "Cytogenetic Dosimetry: Applications in Preparedness for and Response to Radiation Emergencies ," IAEA, Vienne, Safety Guide 2011.

[21] M A Zerabruk, "Repair of sub-lethal damage following single and split-dose irradiation using Co-60 gamma and p(66)/Be neutrons," Cape Peninsula University of Technology, Cape Town, MTech thesis Unpublished, 2005.

[22] R L Warters and K G Hofer, "Radionuclide Toxicity in Cultured Mammalia Cells: Elucidation of the Primary Site for Radiation-Induced Division Delay," *Radiation Research*, vol. 69, pp. 348-358, 1977.

[23] G F Knoll, *Radiation detection and measurement*, 3rd ed. New York, United States of America: John Wiley & Sons, 1999.

[24] Nucleide.org. (2012, August) Nucleide. [Online]. www.nucleide.org/DDEP_WG/Nuclides

[25] T Theron, J Slabbert, A Serafin, and L Böhm, "The Merits of Cell Kinetic Parameters for the Assessment of Intrinsic Cellular Radiosensitivity to Photon and High Linear Energy Transfer Neutron Irradiation," *International Journal of Radiation Oncology and Biological Physics*, vol. 37, no. 2, pp. 423-428, 1997.

[26] T C Hsu, W C Dewey, and R M Humphrey, "Radiosensitivity of Cells of Chinese Hamster In Vitro in Relation to the Cell Cycle," *Experimental Cell Research*, vol. 27, pp. 441-452, 1962.

[27] J Bergonié and L Tribondeau, "Interpretation of Some Results of Radiotherapy and an Attempt at Determining a Logical Technique of Treatment ," *Radiation Research*, vol. 11, pp. 587-588, 1959.

[28] J P Slabbert et al., "Radiosensitivity variation in human tumor cell lines exposed in vitro to p(66)/Be neutrons or Co-60 y-rays," *Strahlentherapie und Onkologie*, vol. 172, no. 10, pp. 567-572, 1996.

[29] M Fenech, "Cytokinesis-block micronucleus cytome assay," *Nature Protocols*, vol. 2, no. 5, pp. 1084 - 1104, May 2007.

[30] Cayman Chemical. (2013, January) Cayman Chemical. [Online]. www.caymanchem.com/catalog/11328

[31] H Norppa and G C M Falck, "What do human micronuclei contain?," *Mutagenesis*, vol. 18, no. 3, pp. 221 - 233, 2003.

[32] A Vral, F Verhaegen, H Thierens, and L De Ridder, "Micronuclei induced by fast neutrons versus Co-60 gamma-rays in human peripheral blood lymphocytes," *International Journal of Radiobiology*, vol. 65, pp. 321 - 328, 1994.

[33] D Varga et al., "An automated scoring procedure for the micronucleus test by image analysis," *Mutagenesis*, vol. 19, pp. 391 - 397, 2004.

[34] P Willems et al., "Automated micronucleus (MN) scoring for population triage in case of large scale radiation events," *International Journal of Radiation Biology*, pp. 1 - 10, October 2009.

[35] International Commission on Radiological Protection, *Relative Biological Effectiveness (RBE), QualityFactor (Q), and Radiation Weighting Factor (w_R)*, 92nd ed., J VALENTIN, Ed.: PERGAMON, 2003.

[36] International Commission on Radiological Protection, "The 2007 Recommendations of the International Commission on Radiological Protection," ICRP, ICRP Publication 103. Ann. ICRP 37 (2-4)., 2007.

[37] F Paquet et al., "The assessment and management of risks associated with exposures to short-range Auger- and beta-emitting radionuclides. State of the art and proposals for lines of research," *Journal of Radiological Protection*, vol. 33, January 2013.

[38] A L McNamara, S Guatelli, D A Prokopovich, M I Reinhard, and A B Rosenfield, "A comparison of X-ray and proton beam low energy secondary electron track structures using the low energy models of Geant4," *International Journal of Radiation Biology*, vol. 88, no. 1 - 2, pp. 164 - 170, January - February 2012.

[39] Geant4 Collaboration, Geant4 User's Guide for Application Developers, 2012, Version: geant4 9.6.0.

[40] A Ivantchenko, V Ivanchenko, J M Q Molina, and S L Incerti, "Geant4 hadronic physics for space radiation environment," *International Journal of Radiation Biology*, vol. 88, no. 1, pp. 171-175, January 2012.

[41] N Nikjoo, D Emfietzoglou, and D E Charlton, "The Auger effect in physical and biological research," *International Journal of Radiation Biology*, vol. 84, no. 12, pp. 1001-1026, December 2008.

[42] A V Ivanchenko et al., "Combination of electromagnetic physics processes for microdosimetry in liquid water using the Geant4-DNA Monte Carlo simulation toolkit," *Nuclear Instruments and Methods in Physics Research Section B*, vol. 273, pp. 95 - 97, 2012.

[43] Z Francis et al., "Molecular scale track structure simulations in liquid water using the Geant4-DNA Monte Carlo processes," *Applied Radiation and Isotopes*, vol. 69, pp. 220 - 226, 2011.

[44] Geant4-DNA. [Online]. www.geant4-DNA.org

[45] A Valentin, M Raine, J E Sauvestre, M Gaillardin, and P Paillet, "Geant4 physics processes for microdosimetry simulation: Very low energy electromagnetic models for electrons in silicon," *Nuclear Instruments and Methods in Physics Research B*, vol. 288, pp. 66-73, 2012.

[46] Z Francis, S Incerti, M Karamitros, H N Tran, and C Villagrasa, "Stopping power and ranges of electrons, protons and alpha particles in liquid water using the Gean4-DNA package," *Nuclear Instruments and Methods in Physics Research B*, vol. 269, pp. 2307-2311, February 2011.

[47] M Dingfelder, D Hantke, M Inokuti, and H G Paretzke, "Electron inelastic-scattering cross sections in liquid water," *Radiation Physics and Chemistry*, vol. 53, pp. 1-18, 1998.

[48] D Emfietzoglou, "Inelastic cross-sections for electron transport in liquid water: a comparison of dielectric models," *Radiation Physics and Chemistry*, vol. 66, pp. 373-385, 2003.

[49] L S Yasui, "Molecular and cellular effects of Auger emiiters: 2008 - 2011," *International Journal of Radiation Biology*, vol. 88, no. 12, pp. 864 - 870, December 2012.

[50] K S Sastry, "Biological effects of the Auger emitter iodine-123: a review. Report no. 1 of AAPM Nulear Medicine Task Group No. 6," *Medical Physics*, vol. 19, pp. 1361-70, 1992.

[51] International Commission on Radiological Protection, "Radionuclide Transformations," *ICRP*, vol. Publication 38, no. 3, 1983.

[52] D E Charlton and J Booz, "Monte Carlo treatment of the decay of iodine-125," *Radiation Research*, vol. 87, pp. 10-23, 1981.

[53] M J Berger, "Improved dose point kernels for electron and beta-ray dosimetry," National Bereau of Standards, Progress Report NBSIR 73-107, 1973.

[54] J L Humm and D E Charlton, "A new calculational method to assess the therapeutic potential of Auger electron emission," *International Journal of Radiation Oncology and Biological Physics*, vol. 17, no. 2, pp. 351-360, 1989.

[55] E Pomplun, "I-123: Calculation of the Auger electron spectrum and assessment of the strand breakage efficiency.," *Biophysical Aspects of Auger Processes, AAPM Symposium Series No. 8*, pp. 121-136, 1992.

[56] E Pomplun, "Monte Carlo-simulated Auger electron spectra for radionuclides of radiobiological and medical interest - a validation with noble gas ionization data," *International Journal of*

Radiobiology, vol. 88, no. 1-2, pp. 108-114, Jan - Feb 2012.

[57] J L Humm, R W Howell, and D V Rao, "Dosimetry of Auger-electron-emitting radionuclides: Report No. 3 of AAPM Nuclear Medicine Task Group No. 6," *Medical Physics*, vol. 21, no. 12, December 1994.

[58] S M Goddu, R W Howell, and D V Rao, "Cellular dosimetry: Absorbed fractions for monoenergetic electron and alpha particle sources and S-values for radionuclides uniformly distributed in different cell compartments," *Journal of Nuclear Medicine*, vol. 35, pp. 303-316, 1994.

[59] W R Leo, "Techniques for Nuclear and Particle Physics Experiments," in *Techniques for Nuclear and Particle Physics Experiments*.: Springer, ch. 2.2 - 2.4.

[60] C Bousis, D Emfietzoglou, and H Nikjoo, "Calculations of absorbed fractions in small water spheres for low-energy monoenergetic electrons and the Auger-emitting radionuclide I-123 and I-125," *International Journal of Radiation Biology*, vol. 88, no. 12, pp. 916-921, 2012.

[61] A I Kassis et al., "Radiotoxicity of I-125 in Mammalian Cells," *Radiation Research*, vol. 111, pp. 305-318, 1987.

[62] A I Kassis, S J Adelstein, C Haydock, and K S Sastry, "Radiotoxicity of S-75 and S-35: Theory and application to a cellular model," *Radiation Research*, vol. 84, pp. 407-425, 1980.

[63] A I Kassis, "Toxicity and therapeutic effects of low-energy electrons," *Nuclear Instruments and Methocs in Physics Research B*, vol. 87, pp. 279-284, 1994.

[64] G M Makrigiorgos et al., "Radiotoxicity of 5-[123I]Iodo-2-deoxyuridine in V79 Cells: A Comparison with 5-[125I]Iodo-2-deoxyuridine," *Radiation Research*, vol. 118, pp. 532-544, 1989.

[65] A I Kassis, F Fayad, B M Kinsey, K S Sastry, and S J Adelstein, "Radiotoxicity of an I-125 labeled DNA Intercalator in Mammalian Cells," *Radiation Research*, vol. 118, no. 2, pp. 283-294, 1989.

[66] R W Howell, D V Rao, D Hou, V R Narra, and K S Sastry, "The Question of Relative Biological Effectiveness and Quality Factor for Auger Emitters Incorporated into Proliferating Mammalian Cells," *Radiation Research*, vol. 128, pp. 282-292, 1991.

[67] S M Goddu, D V Rao, and R W Howell, "Multicellular dosimetry for micrometastases: Dependance of self-dose versus cross-dose to cell nuclei on type of energy of radiation and subcellular distribution of radionuclides," *Journal of Nuclear Medicine*, vol. 35, pp. 521-530, 1994.

[68] R W Howell and A Bishayee, "Bystander effects casued by nonuniform distributions of DNA-incorporated I-125," *Micron*, vol. 33, pp. 127-132, 2002.

[69] R W Howell, V R Narra, K S Sastry, and D V Rao, "On the Equivalent Dose for Auger Electron Emitters," *Radiation Research*, vol. 134, no. 1, pp. 71-78, 1993.

[70] D V Rao, V R Narra, R W Howell, and K S Sastry, "Biological consequences of nuclear versus cytoplasmic decays of I-125: Cysteamine as a radioprotector against Auger cascades in vivo,"

Radiation Research, vol. 124, pp. 188-193, 1990.

[71] N Miyazaki and Y Fujiwara, "Mutagenic and Lethal Effects of 5-[I-125]-iodo-2-deoxyuridine incorporated into DNA of Mammalian Cells and their RBEs," *Radiation Research*, vol. 88, pp. 456-465, 1981.

[72] V R Narra, R W Howell, R S Harapanhalli, K S Sastry, and D V Rao, "Radiotoxicity of some Iodine-123, Iodine-125 and Iodine-131 labeled compounds in Mouse Testes: Implications for Radiopharmaceutical Design," *The Journal of Nuclear Medicine*, vol. 33, no. 12, pp. 2196-2201, 1992.

[73] D V Rao, V R Narra, R W Howell, G F Govelitz, and K S Sastry, "In-vivo radiotoxicity of DNA-incorporated I-125 compared with that of densely ionising alpha-particles," *The Lancet*, vol. 334, no. 8664, pp. 650-653, September 1989.

[74] L S Yasui, A Hughes, and E R DeSombre, "Relative Biological Effectiveness of Accumulated [I-125]dU and [I-125]-Estrogen decays in Estrogen Receptor-expressing MCF-7 Human Breast Cancer Cells," *Radiation Research*, vol. 155, no. 2, pp. 328-334, 2001.

[75] K F Baverstock and D E Charlton, Eds., *DNA Damage by Auger emitters*. London, U.K.: Taylor & Francis, 1998.

[76] G Makrigiorgios, S J Adelstein, and A I Kassis, "Auger electron emitters: Insights gained from in vitro experiments," *Radiation and Environmental Biophysics*, vol. 29, pp. 75-91, 1990.

[77] S M Goddu, R W Howell, and D V Rao, "Calculation of equivalent dose for Auger electron emitting radionuclides in human organs," *Acta Oncologica*, vol. 35, no. 7, pp. 909 - 916, 1996.

[78] G Chabot. (2011, August) Health Physics Society. [Online]. http://hps.org/publicinformation/ate/faqs/gammaandexposure.html [Accessed: 29 May 2013]

[79] R McGinnis. Rad Pro Calculator Online. [Online]. www.radprocalculator.com

[80] Princeton University. (2007, August) Radiation safety guide: Units of Measurement. [Online]. http://web.princeton.edu/sites/ehs/radsafeguide/rsg_app_e.htm [Accessed: 29 May 2013]

[81] International Atomic Energy Agency, "Absorbed Dose Determination in External Beam Radiotherapy," International Atomic Energy Agency, Vienna, Technical Report Series STI/DOC/010/398, 2000.

[82] V Vandersickel et al., "The radiosensitizing effect of Ku70/80 knockdown in MCF10A cells irradiated with X-rays and p(66)+Be(40) neutrons," *Radiation Oncology*, vol. 5, p. 30, 2010.

[83] J Sjoblom, Ed., *Encyclopedic Handbook of Emulsion Technology*.: CRC Press, 2001.

[84] A Irimajiri, Y Doida, T Hanai, and A Inouye, "Passive electrical properties of cultured murine lymphoblast (L5178Y) with reference to its cytoplasmic membrane, nuclear envelope, and intracellular phases," *Journal of Membrane Biology*, vol. 38, no. 3, pp. 209-232, 1978.

[85] K Asami, Y Takahashi , and S Takashima , "Dielectric properties of mouse lymphocytes and erythrocytes," *Biochimica et Biophysica Acta*, vol. 1010, pp. 49-55, 1989.

[86] CERN. (2014) ROOT. [Online]. root.cern.ch

[87] J P Slabbert, L August, A Vral, and J Symons, "The relative biological effectiveness of a high energy neutron beam for micronuclei induction in T-lymphocytes of different individuals," *Radiation Measurements*, vol. 2010, 2010.